Space Research Centre

Polish Academy of Sciences

Discipline: Natural Sciences
Field: Earth and Related Environmental Sciences

Ph.D. Thesis

Analysis of Markov Processes in Space Environment

Dariusz Andrzej Wójcik, M.Sc.

Supervisor:

Prof. dr hab. Wiesław Marian Macek

Warsaw 2025

Acknowledgements.

I am deeply grateful to my supervisor, Prof. dr hab. Wiesław Marian Macek, for his guidance, patience, and belief in my abilities, which have been instrumental in shaping this research. Thank you for your support throughout this time, for your constructive feedback, expertise, and invaluable insights, which have contributed to the development of this work. Thank you for being a source of immense motivation.

I would like to express my sincere gratitude to Dr. Marek Strumik for his insightful suggestions and comments, which have helped refine my work. Furthermore, I extend my heartfelt thanks to the scientific staff of the CBK, CAMK, and IGF PAN institutes for generously sharing their expertise. Their valuable knowledge and intellectual support have significantly enriched my research.

To my parents and family, who have been my foundation through it all, thank you for your unconditional love and support. Your encouragement, patience, and understanding during difficult moments have been invaluable. Thank you for believing in me, for cheering on me, and for your understanding. Your unwavering faith in me has been my greatest source of motivation, and I could not have done this without you.

Finally, I would like to express my deepest gratitude to my partner for her love, support, encouragement, and invaluable time she has dedicated to me. Your presence has been a constant source of strength and happiness. Thank you for being an integral part of my life.

Analysis of Markov Processes in Space Environment

Dariusz Andrzej Wójcik

Abstract.
This doctoral thesis consists of a series of monothematic papers devoted to modern mathematical theory applied to stochastic processes in space plasmas. In a Markov process, given an initial probability density function, the transition to the next stage can be fully determined. Hence, this approach can be considered a bridge between the statistical and dynamical analysis of complex systems. As is already known, solar wind turbulence on large magnetohydrodynamic scales exhibits Markovian features. Therefore, in our studies we have shown that stochastic fluctuations of the magnetic fields measured onboard the NASA *Magnetospheric Multiscale* (*MMS*) mission on much smaller kinetic scales can also be described by Markov processes [1]. Next, we have analyzed the magnetic *MMS* data behind the Earth's bow shock, inside the magnetosheath, and near the magnetopause [2]. Furthermore, we have compared magnetic and velocity fluctuations in all these different regions of circumterrestrial plasma [3]. We have proved that the Chapman-Kolmogorov necessary condition for Markov processes is well satisfied in magnetosheath plasma. In particular, we have shown that for stochastic magnetic fluctuations the Kramers-Moyal expansion stops after the first and second terms, describing drift and diffusion, respectively. These lowest-order Kramers-Moyal coefficients are linear and quadratic functions of magnetic increments, consistent with generalized Ornstein-Uhlenbeck processes. In the case of magnetic fluctuations these coefficients are well fitted to power-law dependence on scales. The numerical solutions of the reduced second order Fokker-Planck equation agree with the experimental probability density functions. For the smallest available scales, we have obtained very peaked density functions (well approximated by the Dirac delta function), while for some moderate scales we have recovered the Kappa distributions resulting from stationary solutions of the Fokker-Planck equation. These distributions are described by various peaked leptokurtic shapes with heavy tails, which, for large values of the kappa parameter, reduce to the normal Gaussian distribution. The kappa parameter and the nonextensivity parameter in Tsallis entropy provide robust measures of the system's departure from equilibrium. It is worth noting that the rescaled distributions exhibit a universal global *scale-invariance*. On the other hand, for velocity fluctuations, higher-order Kramers-Moyal coefficients should be taken into account, with a more complicated functional dependence on the increments of velocity. Admittedly, in this case, we observe more complicated probability density functions. However, we hope that our research results on stochastic fluctuations in space plasma, especially those obtained from the analysis of magnetic fluctuations, will be important for a better understanding of the processes governing turbulent systems in nature.

Acknowledgments. This work has been supported by the National Science Centre (NCN), Poland, through grant No. 2021/41/B/ST10/00823.

[1] W. M. Macek, D. Wójcik, and J. L. Burch, 2023, Magnetospheric Multiscale Observations of Markov Turbulence on Kinetic Scales, *Astrophysical Journal*, 943:152, https://doi.org/10.3847/1538-4357/aca0a0.

[2] W. M. Macek and D. Wójcik, 2023, Statistical analysis of stochastic magnetic fluctuations in space plasma based on the MMS mission, *Monthly Notices of the Royal Astronomical Society*, stad2584, **526**, 5779-5790, 2023, https://doi.org/10.1093/mnras/stad2584.

[3] D. Wójcik and W. M. Macek, 2024, Testing for Markovian character of transfer of fluctuations of solar wind turbulence on kinetic scales, *Physical Review E* **110**, 025203, doi: 10.1103/PhysRevE.110.0252023, https://link.aps.org/doi/10.1103/PhysRevE.110.025203.

Analiza procesów Markowa w środowisku kosmicznym

Dariusz Andrzej Wójcik

Streszczenie.
Niniejsza rozprawa doktorska składa się z serii monotematycznych publikacji poświęconych współczesnej teorii matematycznej stosowanej do procesów stochastycznych w plazmie kosmicznej. W procesie Markowa, przy danej początkowej funkcji gęstości prawdopodobieństwa, przejście do kolejnego stanu jest w pełni deterministyczne. Zatem podejście to można uznać za pomost między analizą statystyczną a dynamiką złożonych układów. Jak już wiadomo, turbulencja wiatru słonecznego na dużych skalach magnetohydrodynamicznych wykazuje właściwości markowskie. W naszych badaniach wykazaliśmy, że fluktuacje stochastyczne pól magnetycznych, mierzonych przez przyrządy na pokładzie misji kosmicznych NASA *Magnetospheric Multiscale* (*MMS*) na znacznie mniejszych skalach kinetycznych, również można opisać za pomocą procesów Markowa [1]. Następnie przeanalizowaliśmy dane magnetyczne z misji *MMS* w obszarze za czołem fali uderzeniowej Ziemi, wewnątrz osłony magnetosfery i w pobliżu magnetopauzy [2]. Ponadto porównaliśmy fluktuacje pól magnetycznych i prędkości w tych różnych obszarach plazmy okołoziemskiej [3]. Udowodniliśmy, że w plazmie osłony magnetosfery warunek Chapmana-Kołmogorowa konieczny dla procesów Markowa jest dobrze spełniony. W szczególności, wykazaliśmy, że dla stochastycznych fluktuacji pola magnetycznego rozwinięcie Kramersa-Moyala kończy się na pierwszym i drugim wyrażeniu, które opisują odpowiednio dryf i dyfuzję. Współczynniki Kramersa-Moyala najniższego rzędu są liniowymi i kwadratowymi funkcjami zmian pola magnetycznego, co jest zgodne z uogólnionymi procesami Ornsteina-Uhlenbecka. W przypadku fluktuacji magnetycznych współczynniki te dobrze dopasowują się do zależności prawa potęgowego względem skali. Numeryczne rozwiązania zredukowanego równania Fokkera-Plancka drugiego rzędu są zgodne z eksperymentalnymi funkcjami gęstości prawdopodobieństwa. Na najmniejszych dostępnych skalach uzyskaliśmy bardzo ostro „wypikowane" funkcje gęstości (dobrze przybliżone przez funkcją delta Diraca), natomiast dla pewnych umiarkowanych skal otrzymaliśmy rozkłady kappa wynikające ze stacjonarnych rozwiązań równania Fokkera-Plancka. Rozkłady te są opisane różnymi kształtami leptokurtycznymi z powiększonymi ogonami, które dla dużych wartości parametru kappa przechodzą w standardowy rozkład Gaussa. Parametr kappa oraz parametr nieekstensywności w entropii Tsallisa stanowią wiarygodne miary odchylenia układu od równowagi. Warto zauważyć, że przeskalowane rozkłady wykazują uniwersalną globalną niezmienniczość na skalach kinetycznych. Z drugiej strony, dla fluktuacji prędkości konieczne jest uwzględnienie wyższych rzędów współczynników Kramersa-Moyala, które wykazują bardziej skomplikowaną zależność funkcyjną od przyrostów prędkości. W tym przypadku obserwujemy bardziej złożone funkcje gęstości prawdopodobieństwa. Niemniej jednak mamy nadzieję, że nasze wyniki badań nad fluktuacjami stochastycznymi w plazmie kosmicznej, zwłaszcza te dotyczące analizy fluktuacji magnetycznych, będą istotne dla lepszego zrozumienia procesów rządzących turbulentnymi układami w przyrodzie.

Podziękowania. Niniejsza praca została zrealizowana przy wsparciu finansowym Narodowego Centrum Nauki (NCN) w ramach grantu nr 2021/41/B/ST10/00823.

[1] W. M. Macek, D. Wójcik, and J. L. Burch, 2023, Magnetospheric Multiscale Observations of Markov Turbulence on Kinetic Scales, Astrophysical Journal, 943:152, https://doi.org/10.3847/1538-4357/aca0a0.

[2] W. M. Macek and D. Wójcik, 2023, Statistical analysis of stochastic magnetic fluctuations in space plasma based on the MMS mission, Monthly Notices of the Royal Astronomical Society, stad2584, 526, 5779-5790, 2023, https://doi.org/10.1093/mnras/stad2584.

[3] D. Wójcik and W. M. Macek, 2024, Testing for Markovian character of transfer of fluctuations of solar wind turbulence on kinetic scales, Physical Review E 110, 025203, doi: 10.1103/PhysRevE.110.0252023, https://link.aps.org/doi/10.1103/PhysRevE.110.025203.

Analysis of Markov Processes in Space Environment

Introduction and Synthetic Summary of the Results

Main doctoral thesis: Turbulence in the Earth's magnetosheath exhibits Markovian character on kinetic scales [1,2,3].

Turbulence in space plasmas remains a fundamental and unresolved issue in physical research, particularly in the context of the solar wind and magnetospheric environments. The interplay of magnetic and velocity fluctuations in collisionless plasmas governs energy transfer across scales, from large magnetohydrodynamic (MHD) structures to small kinetic regimes. Classical turbulence theories and analysis methods, such as structural analysis with Kolmogorov's -5/3 power-law for hydrodynamic turbulence and Kraichnan's -3/2 exponent for magnetized fluids, have been extensively used to describe large-scale dynamics. However, at kinetic scales turbulence transitions into a regime where fluid models become inadequate, and statistical approaches are necessary to characterize stochastic processes governing transition to smaller and smaller scales. The recent high-resolution spacecraft measurements allow for the direct exploration of these kinetic-scale processes, providing unprecedented insight into turbulence in the Earth's magnetosphere and enabling modern statistical analyses.

This doctoral dissertation consists of a series of publications that analyze turbulence in the near-Earth environment using high-resolution magnetic field and plasma measurements from the *Magnetospheric Multiscale* (*MMS*) mission [1,2,3]. The goal is to determine whether turbulence at kinetic scales exhibits Markovian properties, evaluate the applicability of the Fokker-Planck equation, and investigate the role of Kappa distributions in characterizing the Probability Density Functions (PDFs) of fluctuations. These findings on very small scales are compared to previous studies on larger MHD scales [4], including classical turbulence theories [5], and observations from other space missions such as *Voyager*, *Advanced Composition Explorer* (ACE), *Ulysses* [4], and the recent *Parker Solar Probe* [6]. Therefore, the comparison of statistical properties between different plasma regions, i.e., just behind the bow shock, deep inside the magnetosheath, and near the magnetopause, provides a test for turbulence theories and the universality of stochastic processes across varying space environments.

The analysis is based on statistical methods that quantify the stochastic properties of turbulence. The brief spectral analysis indicates that at kinetic scales, turbulence exhibits steeper spectral slopes of around -16/3, compared to the inertial range, reinforcing the idea that different physical mechanisms operate at sub-ion scales [7]. One of the key findings is that turbulence at kinetic scales retains a Markovian character, as confirmed through the Chapman-Kolmogorov equation. This result supports the notion that energy transfer in turbulence can be described by a *local* interaction process rather than requiring long-range correlations. The validation of this property at

such small scales is significant because it suggests that energy redistribution mechanisms are primarily local. Furthermore, the Kramers-Moyal expansion is employed, with the first and second terms that follow linear and quadratic dependencies as drift and diffusion terms. This suggests that turbulence follows generalized Ornstein-Uhlenbeck processes, enabling the formulation of the Fokker-Planck equation that governs the evolution of turbulent fluctuations. The solutions of this equation align well with experimentally derived PDFs, demonstrating that turbulence at these scales can be described by Kappa distributions with varying degrees of non-Gaussianity. The presence of scale invariance further supports the universality of these statistical properties across different near-Earth regions. The dependence of the Kappa parameter on scale size further supports the idea that turbulence cascades in a self-similar but intermittent manner, confirming results from past solar wind studies [5].

Another important part of this study is the distinction between the statistical properties of magnetic and velocity fluctuations from the *MMS* mission. While magnetic field fluctuations exhibit strong Markov properties, velocity fluctuations show somewhat larger deviations, and the higher-order Kramers-Moyal terms should be employed. This result aligns with other studies suggesting that kinetic turbulence is not solely governed by linear wave interactions but is also influenced by localized, nonlinear structures [6]. These findings are in agreement with previous analyses of turbulence in the inertial range [4], but extend the understanding to much smaller scales, where kinetic effects become significant. The comparison with *Parker Solar Probe* mission data [6] indicates that similar statistical properties exist in the near-Sun turbulence, reinforcing the idea that turbulence in space plasmas follows a self-consistent stochastic framework.

This contribution is also significant by looking at the comparison of Markovian properties. By analyzing turbulence in various near-Earth environments, the results demonstrate that while the underlying stochastic processes exhibit universal features, the strength of intermittency and non-Gaussianity varies with plasma conditions. This observation suggests that turbulence evolution is influenced by external factors, such as large-scale solar wind structures, rather than being purely intrinsic to the kinetic cascade [4]. This reinforces the argument that while turbulence is a universal process, its local characteristics depend strongly on boundary conditions and plasma environment.

Further analysis of the PDFs of turbulent fluctuations reveals that the probability distributions deviate significantly from Gaussianity at the smallest resolved scales, highlighting the role of intermittency and coherent structures in kinetic turbulence. The presence of heavy-tailed distributions, particularly at sub-ion scales, suggests a nonuniform energy cascade dominated by localized dissipation events, potentially linked to strong current sheets [6].

The implications of these findings are broad, providing new insights into the nature of turbulence-driven energy dissipation in space plasmas. The confirmation of Markovian properties at kinetic scales offers a strong foundation for stochastic modeling approaches, bridging the gap between large-scale MHD turbulence and small-scale kinetic effects. The emergence of Kappa distributions as natural solutions to the Fokker-Planck equation underscores their importance in describing

turbulent fluctuations in space and astrophysical plasmas. These results contribute to a deeper understanding of the universal features of plasma turbulence, offering valuable constraints for theoretical models and numerical simulations.

Keywords: Kinetic scales, Markov processes, MMS probes, Plasmas, Solar wind, Magnetosphere, Turbulence.

Acknowledgments. This doctoral thesis has been supported by the National Science Centre, Poland (NCN), through grant No. 2021/41/B/ST10/00823.

References:

The papers of this doctoral dissertation (Open Access):
[1] W. M. Macek, D. Wójcik, J. L. Burch, 2023, Magnetospheric Multiscale Observations of Markov Turbulence on Kinetic Scales. *Astrophys. J.* 943:152, https://doi.org/10.3847/1538-4357/aca0a0.
[2] W. M. Macek, D. Wójcik, 2023, Statistical analysis of stochastic magnetic fluctuations in space plasma based on the MMS mission. *Mon. Not. R. Astronom. Soc.* 526, 5779–5790, https://doi.org/10.1093/mnras/stad2584.
[3] D. Wójcik, W. M. Macek, 2024, Testing for Markovian character of transfer of fluctuations in solar wind turbulence on kinetic scales. *Phys. Rev. E* 110, 025203, https://doi.org/10.1103/PhysRevE.110.025203.

Other papers:
[4] M. Strumik, W. M. Macek, 2008, Testing for Markovian character and modeling of intermittency in solar wind turbulence. *Phys. Rev. E* 78, 026414, https://doi.org/10.1103/PhysRevE.78.026414.
[5] R. Bruno, V. Carbone, 2016, Turbulence in the Solar Wind. *Springer International*, Berlin, Vol. 928, https://doi.org/10.1007/978-3-319-43440-7.
[6] S. Benella, M. Stumpo, G. Consolini, T. Alberti, V. Carbone, M. Laurenza, 2022, Markovian Features of the Solar Wind at Subproton Scales, *Astrophys. J. Lett.*, 928, L21, https://doi.org/10.3847/2041-8213/ac6107.
[7] W. M. Macek, A. Krasińska, M. V. D. Silveira, D. G. Sibeck, A. Wawrzaszek, J. L. Burch, C. T. Russell, 2018, Magnetospheric Multiscale observations of turbulence in the magnetosheath on kinetic scales, *Astrophys. J. Lett.*, 864, L29, https://doi.org/10.3847/2041-8213/aad9a8.

The Astrophysical Journal, 943:152 (11pp), 2023 February 1 https://doi.org/10.3847/1538-4357/aca0a0

Magnetospheric Multiscale Observations of Markov Turbulence on Kinetic Scales

Wiesław M. Macek[1,2,4], Dariusz Wójcik[1,2], and James L. Burch[3]
[1] Institute of Physical Sciences, Faculty of Mathematics and Natural Sciences, Cardinal Stefan Wyszyński University, Wóycickiego 1/3, 01-938 Warsaw, Poland
macek@uksw.edu.pl, d.wojcik@uksw.edu.pl
[2] Space Research Centre, Polish Academy of Sciences, Bartycka 18 A, 00-716 Warsaw, Poland; macek@cbk.waw.pl, dwojcik@cbk.waw.pl
[3] Southwest Research Institute, San Antonio, TX, USA; jburch@swri.edu
Received 2022 July 11; revised 2022 October 23; accepted 2022 November 1; published 2023 February 3

Abstract

In our previous studies we have examined solar wind and magnetospheric plasma turbulence, including Markovian character on large inertial magnetohydrodynamic scales. Here we present the results of the statistical analysis of magnetic field fluctuations in the Earth's magnetosheath, based on the Magnetospheric Multiscale mission at much smaller kinetic scales. Following our results on spectral analysis with very large slopes of about $-16/3$, we apply a Markov-process approach to turbulence in this kinetic regime. It is shown that the Chapman–Kolmogorov equation is satisfied and that the lowest-order Kramers–Moyal coefficients describing drift and diffusion with a power-law dependence are consistent with a generalized Ornstein–Uhlenbeck process. The solutions of the Fokker–Planck equation agree with experimental probability density functions, which exhibit a universal global scale invariance through the kinetic domain. In particular, for moderate scales we have the kappa distribution described by various peaked shapes with heavy tails, which, with large values of the kappa parameter, are reduced to the Gaussian distribution for large inertial scales. This shows that the turbulence cascade can be described by the Markov processes also on very small scales. The obtained results on kinetic scales may be useful for a better understanding of the physical mechanisms governing turbulence.

Unified Astronomy Thesaurus concepts: Solar wind (1534); Interplanetary turbulence (830); Heliosphere (711); Interplanetary physics (827); Space plasmas (1544); Magnetohydrodynamics (1964)

1. Introduction

Turbulence appears in many real systems in nature, including various fluids with embedded magnetic fields (Frisch 1995; Biskamp 2003). In particular, space and astrophysical plasmas are natural laboratories for investigating the dynamics of turbulence (Chang 2015; Bruno & Carbone 2016; Echim et al. 2021). This is a complex phenomenon that contains deterministic and random components. Therefore, besides the effort to describe this problem in terms of difference equations, a statistical approach is also useful. The important question for any dynamical system is whether given a probability distribution of the characteristic property of a system in a given moment, one can determine statistical properties of this dynamical system in the future. Therefore, the concept of a Markov process in which the future statistics is independent of the past is an important issue also for turbulence (Pedrizzetti & Novikov 1994). It is possible to prove the existence of a Markov process experimentally and furthermore to extract the differential equation for this Markov process directly from the measured data without using any assumptions or models for the underlying stochastic process (Renner et al. 2001). Strumik & Macek (2008a, 2008b) have applied this statistical method to solar wind magnetic fluctuations in the inertial range. A similar approach has recently been applied to the Parker Solar Probe (PSP) mission in the solar wind at subproton scales (Benella et al. 2022).

Our previous studies have also dealt with turbulence in solar wind and magnetospheric plasmas on large (inertial) magnetohydrodynamic scales, using observations by the Ulysses mission in the solar wind beyond the ecliptic plane (Wawrzaszek & Macek 2010) and by the Voyager mission in the heliosphere and heliosheath (Macek et al. 2011, 2012) and even at the boundaries of the solar system (Macek et al. 2014). Based on the THEMIS mission in the Earth's magnetosheath, we have also verified that turbulence at shocks is well described by inward- and outward-propagating Alfvén waves (Macek et al. 2015, 2017).

Here we consider again turbulence in the Earth's magnetosheath, where timescales are much shorter than those in the heliosheath, based on observations from the Magnetospheric Multiscale (MMS) mission on kinetic scales (Macek et al. 2018). In this case it is hotly debated whether the turbulence energy cascade results from the dissipation of the kinetic Alfvén waves (KAWs; e.g., Schekochihin et al. 2009). Papini et al. (2021) have recently argued that the turbulence energy at kinetic scales could not be related to KAW activity but is mainly driven by localized nonlinear structures. Certainly, it is possible that the observed stochastic nature of fluctuations in the sub-ion scale could be due to the interaction between coherent structures (e.g., Chang 2015; Echim et al. 2021), including local reconnection processes at kinetic scales (Macek et al. 2019a, 2019b). Admittedly, the nature of wave modes in operation cannot be determined by statistical analysis, but we hope that the Markov approach will provide a contact point with a dynamical system approach to turbulence and hence that the results of this study will be useful in future investigations.

The data under study are briefly described in Section 2, with statistical methods outlined in Section 3. In Section 4 we present the results of our analysis, showing that the solutions of

[4] Corresponding author.

the Fokker–Planck equation agree well with experimental probability density functions (PDFs). The importance of Markov processes for turbulence in space plasmas with a universal global scale invariance through the kinetic domain is underlined in Section 5.

2. Data

The MMS mission was launched in 2015 to investigate plasma processes in the magnetospheric and the solar wind plasma, especially on small scales (Burch et al. 2016). We analyze the statistics of the fluctuations of all components of the magnetic field $\boldsymbol{B} = (B_x, B_y, B_z)$ with the total magnitude $B_T = |\boldsymbol{B}|$ in the Geocentric Solar Ecliptic (GSE) coordinates obtained from the FluxGate Magnetometer (FGM; see Russell et al. 2016). We investigate BURST-type observations with the highest available resolution of $\Delta t_B = 7.8$ ms, which corresponds to approximately 128 samples per second. Macek et al. (2018) have selected an interval on 2015 December 28 from 01:48:04 to 01:52:59 with 37,856 measurement points for the magnetic field, which are available just behind the bow shock (BS). The position of the MMS during this event within the Earth's magnetosheath has been depicted in Figure 1, case (a) of Macek et al. (2018). Admittedly, the highest-resolution BURST-type magnetic data $\boldsymbol{B}$ are limited in time. This analysis has allowed us to go well beyond the kinetic regime, i.e., above the electron Taylor-shifted inertial frequency $f_{\lambda e} = (V/c)f_{\rm pe}$, where $f_{\rm pe}$ is the plasma frequency, V is the solar wind velocity, and c denotes the speed of light, at above $f_{\lambda e} \sim 20$ Hz, characterized by a steep spectrum with a slope of about $-11/2$, as seen in their Figure 2 (for details, see Macek et al. 2018). Even though with lower resolution for the ion velocity V the spectrum could only be resolved to the onset of kinetic scales at $\sim$2 Hz, it is worth investigating this case further in view of the Markov property of turbulence.

3. Methods

As usual we use the increments of any characteristic parameter x describing a turbulent system

$$\delta x(t, \tau) = x(t + \tau) - x(t) \tag{1}$$

at each time t and a given scale τ. Following the well-known scenario, the fluctuations $\delta x(t, \tau)$ in a larger scale are transferred to smaller and smaller scales τ. In this way turbulence may be regarded as a stochastic process with the N-point joint transition probability distribution $P(x_1, \tau_1|x_2, \tau_2;\ldots;x_N, \tau_N)$, where $P(x_i, \tau_i|x_j, \tau_j) = P(x_i, \tau_i; x_j, \tau_j)/P(x_j, \tau_j)$ is the conditional PDF. The process is Markovian if the N-point joint transition probability distribution is completely determined by the initial values. Hence in this case one should have

$$P(x_1, \tau_1|x_2, \tau_2;\ldots;x_N, \tau_N) = P(x_1, \tau_1|x_2, \tau_2), \tag{2}$$

or more generally, the necessary Chapman–Kolmogorov condition is satisfied:

$$P(x_1, \tau_1|x_2, \tau_2) = \int_{-\infty}^{+\infty} P(x_1, \tau_1|x', \tau')P(x', \tau'|x_2, \tau_2)dx', \tag{3}$$

where $\tau_1 < \tau' < \tau_2$. Further, using the Kramers–Moyal expansion, one obtains this condition in a differential form

$$-\frac{\partial P(x, \tau|x', \tau')}{\partial \tau} = \sum_{k=1}^{\infty}\left(-\frac{\partial}{\partial x}\right)^k D^{(k)}(x, \tau)P(x, \tau|x', \tau'), \tag{4}$$

where the coefficients $D^{(k)}(x, \tau)$ are determined by the moments of the conditional PDFS (see Risken 1996; Benella et al. 2022):

$$M^{(k)}(x, \tau, \tau') = \int_{-\infty}^{+\infty} (x' - x)^k P(x', \tau'|x, \tau)dx' \tag{5}$$

in the limit $\tau \to \tau'$

$$D^{(k)}(x, \tau) = \frac{1}{k!}\lim_{\tau \to \tau'}\frac{1}{\tau - \tau'}M^{(k)}(x, \tau, \tau'). \tag{6}$$

Moreover, if the fourth-order coefficient is equal to zero, then according to Pawula's theorem, $D^{(k)}(x, \tau) = 0$ for $k \geqslant 3$, and the series is limited to the second order. In this case one arrives at the Fokker–Planck equation in the following reduced differential form (Risken 1996):

$$-\frac{\partial P(x, \tau)}{\partial \tau} = \left[-\frac{\partial}{\partial x}D^{(1)}(x, \tau) + \frac{\partial^2}{\partial x^2}D^{(2)}(x, \tau)\right]P(x, \tau), \tag{7}$$

where the first and second terms describe, respectively, the drift and diffusion functions of the deterministic evolution of the transition probability of a stochastic process described by the Langevin equation

$$-\frac{\partial x}{\partial \tau} = D^{(1)}(x, \tau) + \sqrt{D^{(2)}(x, \tau)}\,\Gamma(\tau), \tag{8}$$

i.e., the process generated (with Itô definition) by the delta-correlated Gaussian white noise, $\Gamma(\tau)\Gamma(\tau') = 2\delta(\tau - \tau')$ (Rinn et al. 2016). The minus signs on the left-hand sides of Equations (7) and (8) indicate that the corresponding transitions proceed backward toward smaller scales. More explicitly, Equation (7) reads

$$\begin{aligned}-\frac{\partial P(x, \tau)}{\partial \tau} &= D^{(2)}(x, \tau)\frac{\partial^2 P(x, \tau)}{\partial x^2} \\ &+ \left[-D^{(1)}(x, \tau) + 2\frac{\partial D^{(2)}(x, \tau)}{\partial x}\right]\frac{\partial P(x, \tau)}{\partial x} + \\ &+ \left[-\frac{\partial D^{(1)}(x, \tau)}{\partial x} + \frac{\partial^2 D^{(2)}(x, \tau)}{\partial x^2}\right]P(x, \tau).\end{aligned} \tag{9}$$

Note that here we have taken the standard definitions used by Risken (1996), while Strumik & Macek (2008a, 2008b) and Renner et al. (2001) have multiplied the Kramers–Moyal coefficients by τ, corresponding to a logarithmic length scale. A simple solution $p_s(x)$ can be obtained from the following stationary Fokker–Planck equation:

$$\frac{\partial}{\partial x}[D^{(2)}(x, \tau)p_s(x)] = D^{(1)}(x, \tau)p_s(x), \tag{10}$$

resulting from the left-hand side of Equation (7) being equal to zero.

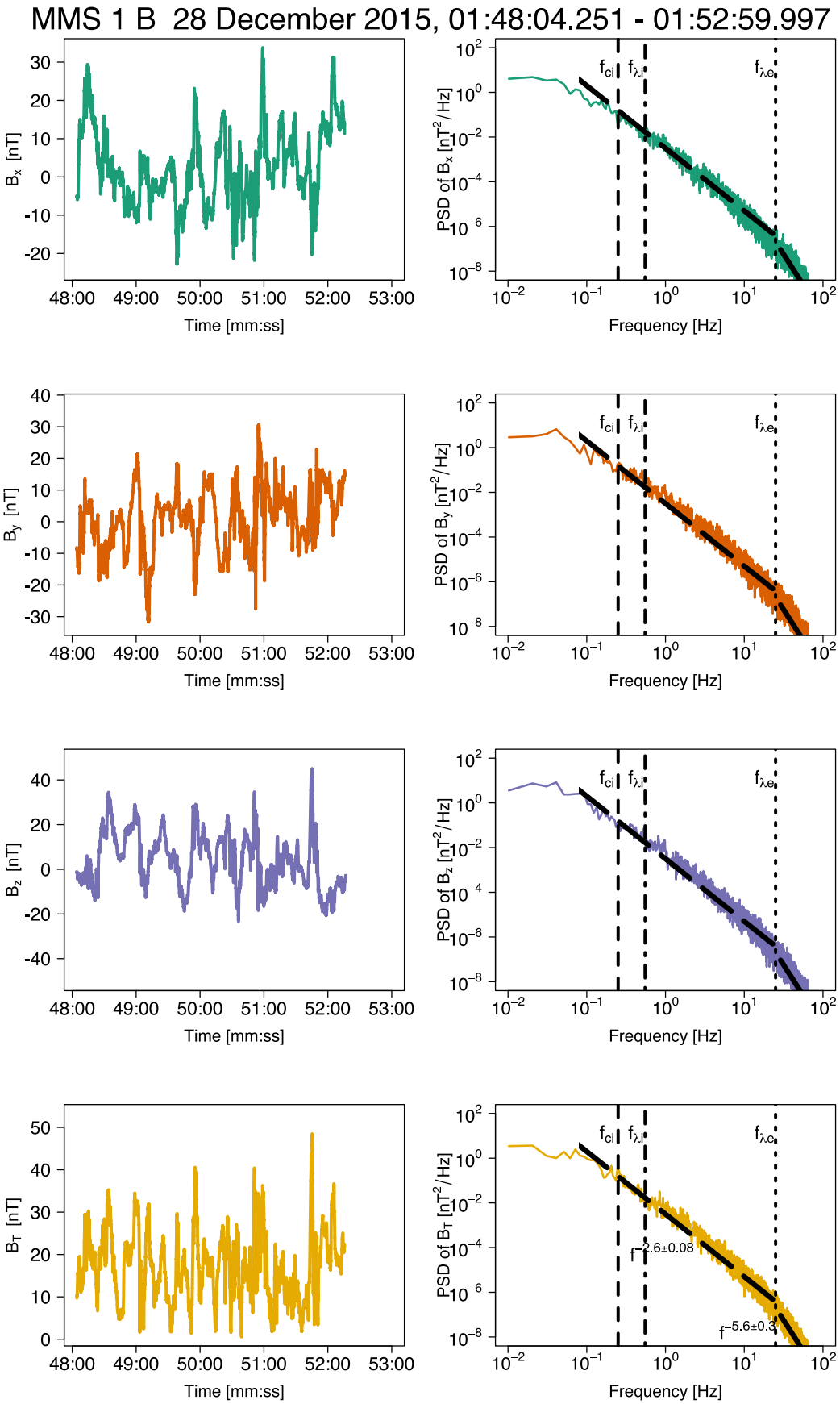

Figure 1. Time series of the magnetic field components $\boldsymbol{B} = (B_x, B_y, B_z)$ in the GSE coordinates and the total magnitude $B_T = |\boldsymbol{B}|$ of the MMS data with the corresponding spectrum of the high-resolution turbulence in the magnetosheath near the BS for frequencies above the ion gyrofrequency f_{ci}, marked by a dashed vertical line, and between the ion $f_{\lambda i}$ and above the electron $f_{\lambda e}$ Taylor-shifted inertial frequencies shown by the dashed–dotted and dotted lines, respectively (case (a) in Table 1 of Macek et al. 2018).

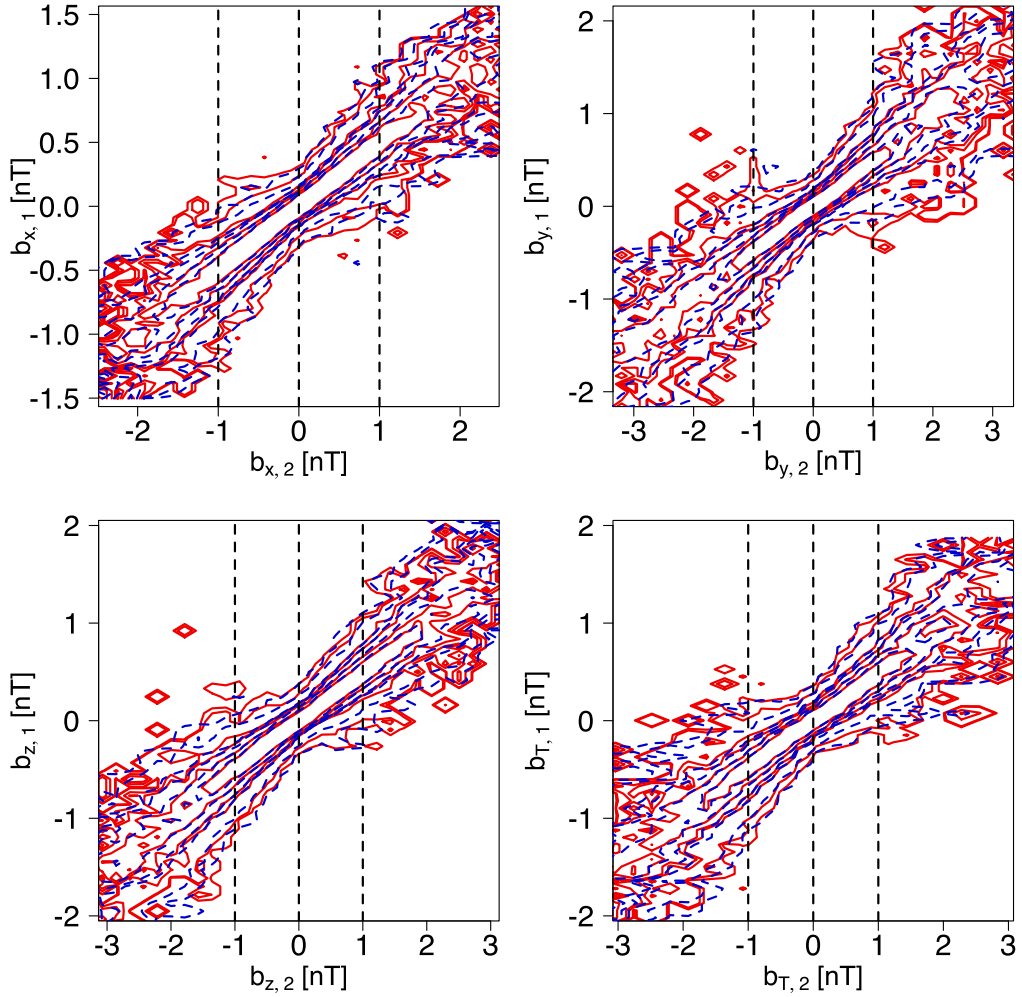

Figure 2. Comparison of the observed contour plots (red curves) of conditional probabilities at various scales τ reconstructed from the MMS magnetic field components in the magnetosheath, corresponding to the spectra in Figure 1, with those contour plots that are reconstructed (dashed blue curves) according to the Chapman–Kolmogorov condition, Equation (3).

4. Results

This method has been successfully applied in the inertial range for magnetic field fluctuations based on the Ulysses data with a time resolution of 1 s (Strumik & Macek 2008a). The Markovian character of solar wind turbulence has also been confirmed by using the ACE data for both magnetic field (16 s) and velocity (48 s) samples (Strumik & Macek 2008b). In this paper we would like to test the Markov property of turbulence on much smaller millisecond scales, which allows us to go beyond the inertial range at least for the case of magnetic field fluctuations.

Figure 1 shows the time series of all components of the magnetic field $\boldsymbol{B} = (B_x, B_y, B_z)$ with magnitude $B_T = |\boldsymbol{B}|$ in the GSE coordinates acquired by the MMS on 2015 December 28 during the 5 minute time BURST interval (from 01:48:04 to 01:52:59), specified as case (a) in Table 1 of Macek et al. (2018), with the corresponding power spectral densities (PSDs) of all the components of the magnetic field $\boldsymbol{B}$ obtained with Welch's (1967) windows. It is worth noting that for the magnetic spectrum above $f_{\lambda e}$ we enter the kinetic regime with the much steeper slope of -5.6 ± 0.3 that is consistent with the value of $-16/3$ predicted by the kinetic theory of Alfvén waves (e.g., Schekochihin et al. 2009).

First, according to Equation (1), we analyze increments of fluctuations $\boldsymbol{b}_\tau := \boldsymbol{B}(t+\tau) - \boldsymbol{B}(t)$ across a timescale τ for each GSE component x, y, and z and the total intensity of the magnetic field $\boldsymbol{B}$. Using the conditional probability introduced in Section 3, we can compute $P(\boldsymbol{b}_1, \tau_1 | \boldsymbol{b}_2, \tau_2)$ on the right-hand side of Equation (2) directly from the MMS data. Then, to verify a local transfer mechanism in the turbulence cascade, we can test whether the Chapman–Kolmogorov condition of Equation (3) is satisfied for the range of scales from τ_1 to τ_2, where $\tau_1 < \tau' < \tau_2$.

In Figure 2 we compare the observed contour plots (red curves) of conditional probabilities at various scales τ with solutions (dashed blue curves) of Equation (3). The subsequent isolines correspond to the following decreasing levels of the conditional PDF (from the middle of the plots) for $\boldsymbol{b}$: 2, 1.1, 0.5, 0.3, 0.05, and 0.02. In the corresponding Figure 3 we verify the Chapman–Kolmogorov Equation (3) by comparison of cuts through the conditional probability distributions for some chosen values of parameter $\boldsymbol{b}_\tau$ in the time series specified by Equation (1), which have been differentiated, and the variance stationarity has been confirmed by using the statistical augmented Dickey–Fuller test (Dickey & Fuller 1979). We have chosen here for the magnetic field $\boldsymbol{b}_\tau$: $\tau_1 = 0.02$ s, $\tau' = \tau_1 + \Delta t_B = 0.0278$ s, and $\tau_2 = \tau_1 + 2\Delta t_B = 0.0356$ s. We see that Equation (3) is approximately satisfied up to the scales of

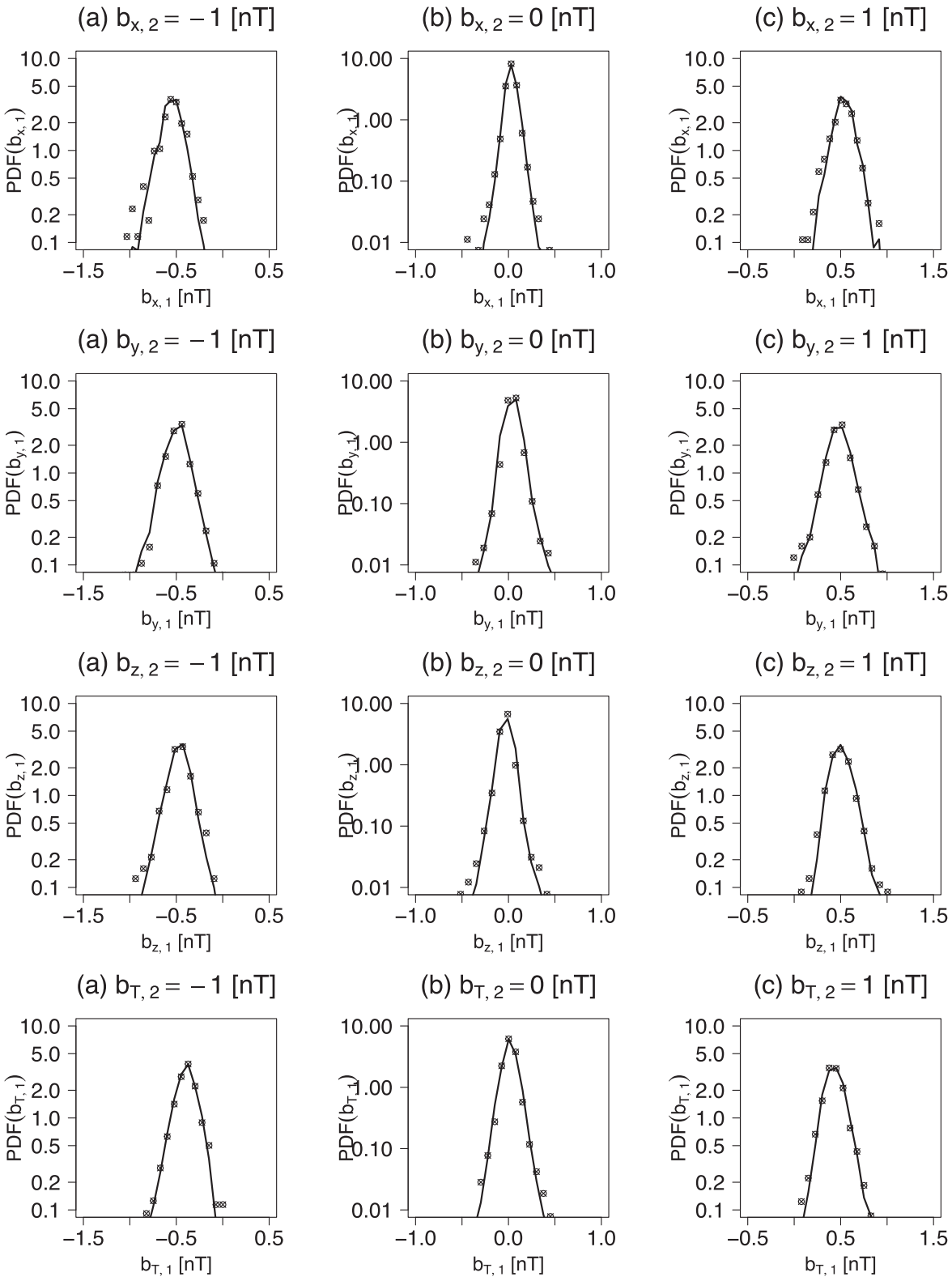

Figure 3. Comparison of cuts through $P(\boldsymbol{b}_1, \tau_1|\boldsymbol{b}_2, \tau_2)$ for the fixed value of all components of the magnetic field increments $\boldsymbol{b}_2$ with $\tau_1 = 0.02$ s, $\tau' = 0.0278$ s, and $\tau_2 = 0.0356$ s.

about 100 $\Delta t_B = 0.78$ s for $\boldsymbol{b}_\tau$, which indicates that the turbulence cascade exhibits Markov properties.

Second, we need to compute the Kramers–Moyal coefficients $D^{(k)}(x, \tau)$ in the Fokker–Planck expansion given by Equation (4). The values of the moments $M^{(k)}(x, \tau, \tau')$ defined in Equation (5) can be obtained from the experimental data by counting the number $N(x', x)$ of occurrences of fluctuations x' and x. Since the errors of $N(x', x)$ are given by $1/\sqrt{N(x', x)}$, the errors for the conditional moments $M^{(k)}(x, \tau, \tau')$ can also be provided (see Renner et al. 2001).

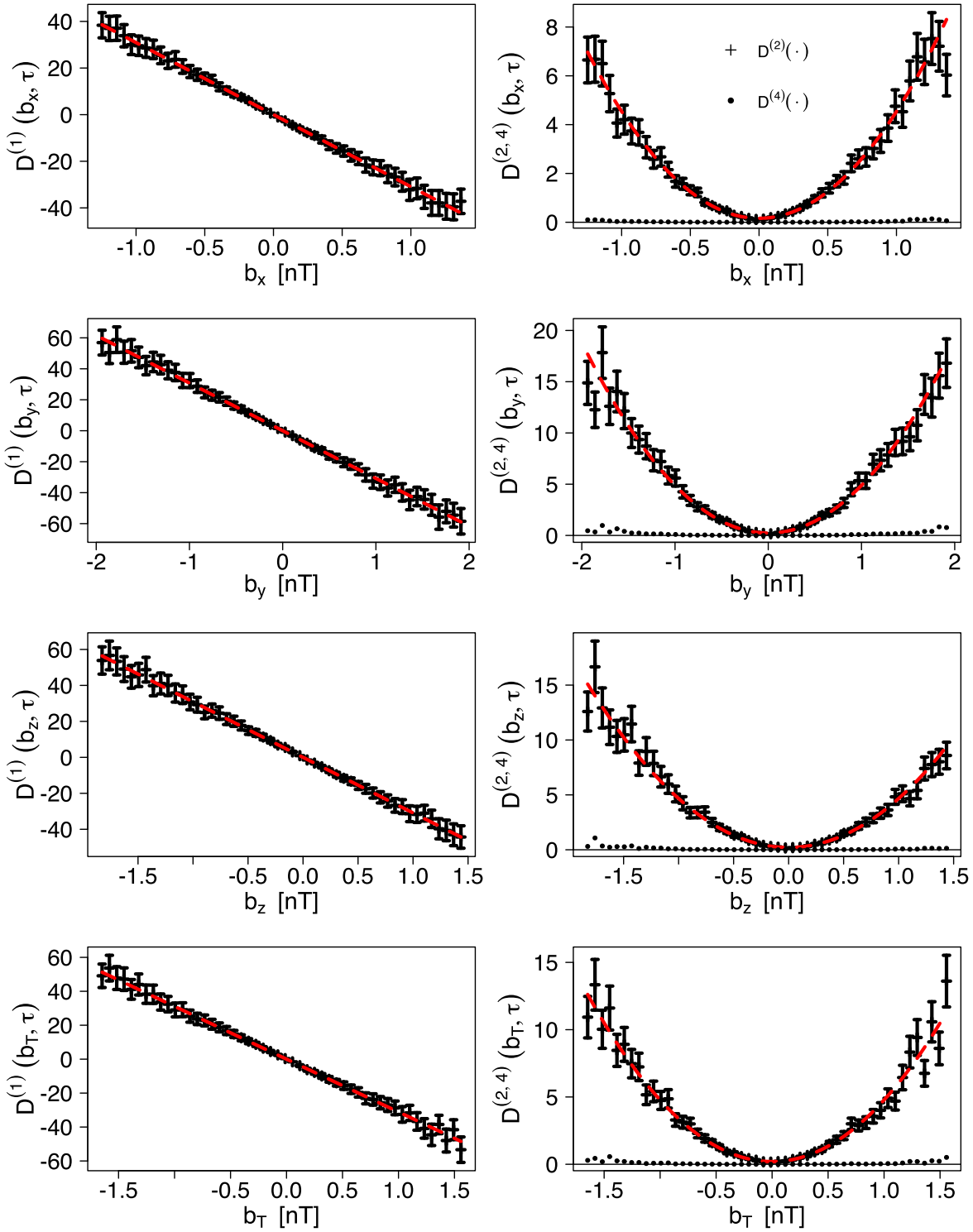

Figure 4. First and second finite-size Kramers–Moyal coefficients depending on the magnetic field increments $\boldsymbol{b}_\tau$ for all components of the magnetic field $\boldsymbol{B} = (B_x, B_y, B_z)$ and the total magnitude $B_T = |\boldsymbol{B}|$. The dashed red lines show the best fits to the calculated values of $D^{(1)}(\boldsymbol{b}, \tau)$ and $D^{(2)}(\boldsymbol{b}, \tau)$ with $D^{(4)}(\boldsymbol{b}, \tau) = 0$, according to Pawula's theorem.

Admittedly $D^{(k)}(x, \tau)$ can only be obtained by extrapolation (for instance by using piecewise linear regression) in the limit $\tau \to \tau'$ in Equation (6), but we have checked that very similar values are obtained when we take the lowest time resolution $\tau - \tau' = \Delta t_B = 0.0078$ s. In fact, we have $D^{(k)}(x, \tau) \approx \frac{1}{k!}\frac{1}{\Delta t} M^{(k)}(x, \tau, \tau')$. Therefore, basically the coefficients $D^{(k)}(x, \tau)$ show the same dependence on x as $M^{(k)}(x, \tau, \tau')$ (see Renner et al. 2001). Figure 4 presents the fits to the first-order drift $D^{(1)}(x, \tau)$ and the second-order finite-size diffusion $D^{(2)}(x, \tau)$ coefficients for $\Delta t_B = 0.0078$ s. We have also verified that the fourth-order coefficient $D^{(4)}(x, \tau)$ is close to zero for the magnetic field data according to Pawula's theorem, which is a necessary and sufficient

Table 1
Parameters for Power-law Dependence of First and Second Kramers–Moyal Coefficients Corresponding to Equations (11) and (12) for All Components of the Magnetic Field $\boldsymbol{B}$ and the Total Magnitude $B_T = |\boldsymbol{B}|$

$\boldsymbol{b}_x$	A	α
a_1	0.6638 ± 0.0355	-1.2376 ± 0.0215
a_2	-0.4925 ± 0.0155	0.9416 ± 0.0094
b_2	0.5918 ± 0.0296	-1.6919 ± 0.0179
$\boldsymbol{b}_y$	A	α
a_1	0.6534 ± 0.0278	-1.2026 ± 0.0169
a_2	-0.4216 ± 0.0203	0.9699 ± 0.0123
b_2	0.5612 ± 0.0316	-1.5263 ± 0.0192
$\boldsymbol{b}_z$	A	α
a_1	0.5646 ± 0.0286	-1.2253 ± 0.0173
a_2	-0.4024 ± 0.0172	1.0934 ± 0.0104
b_2	0.5941 ± 0.0241	-1.6623 ± 0.0146
$\boldsymbol{b}_T$	A	α
a_1	0.6989 ± 0.0225	-1.1191 ± 0.0089
a_2	-0.4946 ± 0.1259	1.1631 ± 0.0498
b_2	0.5854 ± 0.0706	-1.7325 ± 0.0279

condition that the Kramers–Moyal expansion of Equation (4) stops after the second term.

In this case, we see that the best-obtained fits to these lowest-order coefficients are linear

$$D^{(1)}(x, \tau) = -a_1(\tau)x \tag{11}$$

and quadratic functions of x

$$D^{(2)}(x, \tau) = a_2(\tau) + b_2(\tau)x^2, \tag{12}$$

respectively, where the appropriate fitted parameters a_k for $k = 1$ and 2 and b_2 depend on the timescale τ. This corresponds to the generalized Ornstein–Uhlenbeck process. It is interesting to note that, similarly to those obtained for the PSP data by Benella et al. (2022), who have looked at larger τ, the best fit for any x representing each component of $\boldsymbol{b}_\tau$ satisfies a power-law dependence $A\tau^\alpha$ with sufficient accuracy and the values for all the parameters that are listed in Table 1.

In fact, as seen in Figure 5 on the logarithmic scale (see Strumik & Macek 2008a, Figure 5), we have verified here that for the MMS magnetic field data, these lowest-order fits with power-law dependence apply for $\tau \leqslant 100\Delta t_B = 0.78$ s when the PDF is closer to Gaussian, $\tau \sim \tau_G$. However, for higher scales, more complex functional dependence is necessary, especially in the inertial regime (Renner et al. 2001; Strumik & Macek 2008a, 2008b).

We see again that by using the simple linear and parabolic fits of Equations (11) and (12), the stationary solutions of Equation (10) become the well-known continuous kappa distributions (also known as Pearson type VII distribution), which the PDF defined as

$$p_s(x) = \frac{N_o}{\left[1 + \frac{1}{\kappa}\left(\frac{x}{x_o}\right)^2\right]^\kappa} = \frac{N_o'}{[a_2(\tau) + b_2(\tau)x^2]^{1+\frac{a_1(\tau)}{2b_2(\tau)}}}, \tag{13}$$

with $\kappa = 1 + a_1(\tau)/[2b_2(\tau)]$ and $x_o^2 = a_2(\tau)/b_2(\tau)/\kappa = a_2(\tau)/[b_2(\tau) + a_1(\tau)/2]$ (for $a_2(\tau) \neq 0$, $x_o(\tau) \neq 0$) and $N_o = p_s(0)$ satisfying the normalization $\int_{-\infty}^{+\infty} p_s(x')dx' = 1$, i.e., $N_o = \frac{\Gamma(\kappa)}{x_o\sqrt{\pi\kappa}\,\Gamma(\kappa - 1/2)}$. As requested, the boundary condition $p_S(x \to \pm\infty) \to 0$ is also verified here, and with $\kappa \to \infty$, the distribution degenerates into the Maxwellian distribution $N_o e^{-\left(\frac{x}{x_o}\right)^2}$ with $N_o = \frac{1}{x_o\sqrt{\pi}}$. The values of the relevant parameters of Equation (13) obtained by fitting the MMS data to the given distributions are $\kappa = 11.85673$, $x_0 = 1.756009$, and $N_0' = 0.4121234$ for B_x; $\kappa = 10.09043$, $x_0 = 3.05319$, and $N_0' = 0.2684886$ for B_y; $\kappa = 11.04104$, $x_0 = 2.779299$, and $N_0' = 0.2802258$ for B_z; and $\kappa = 12.88198$, $x_0 = 1.75533$, and $N_0' = 0.4133008$ for B_T. These values of κ would correspond to the nonextensivity parameter of the generalized (Tsallis) entropy $q = 1 - 1/\kappa \approx 0.9$, which is somewhat larger than $q \sim 0.5$ for $\kappa \sim 2$ reported for the PSP data by Benella et al. (2022).

In addition, substituting Equations (11) and (12) into Equation (7) we obtain

$$[a_2(\tau) + b_2(\tau)x^2]\frac{\partial^2 P(x, \tau)}{\partial x^2} + [a_1(\tau) + 4b_2(\tau)] \times x\frac{\partial P(x, \tau)}{\partial x} + \frac{\partial P(x, \tau)}{\partial \tau} + [a_1(\tau) + 2b_2(\tau)]P(x, \tau) = 0. \tag{14}$$

This means that in the Fokker–Planck, Equations (9) and (14) become formally the second-order parabolic partial differential equation.

This, in turn, allows us to solve numerically the nonstationary Fokker–Planck equation (Figure 6, dashed lines) using the numerical Euler integration scheme (verified for stationary solution $\frac{\partial P(x,\tau)}{\partial \tau} = 0$, open points), which agrees with those obtained with the modeling package by Rinn et al. (2016). We compare all these theoretical solutions with the PDFs obtained directly from experimental data denoted by the different-colored continuous lines. This comparison is depicted in Figure 6 for various scales τ not greater than τ_G, namely (from bottom to top) for $\tau = 1$, 5, 10, 15, 25, 50, and 100 Δt_B shifted in the vertical direction for clarity of presentation. For moderate values up to $\tau \sim 50\Delta t_B = 0.39$ s in the case of linear and parabolic fits to Equations (11) and (12), we have the kappa distributions. However if we move to the larger scales τ_G from 100 $\Delta t_B = 0.78$ s, the Kramers–Moyal coefficients $D^{(1)}$ and $D^{(2)}$ in Equation (4) are possibly described by more complex polynomial functions, but the PDF is approximately Gaussian, as expected for large values of κ. On the other hand, for the smallest available scales we see a very peaked density function (with large kurtosis) well described by the approximate shape of the Dirac delta function (formally in the limit of $\tau \to 0$).

In Figure 7, we have finally reproduced the PDFs of all components $\boldsymbol{b}_\tau$ rescaled by the respective standard deviations $\sigma_{\boldsymbol{b},\tau}$, which are consistent with the stationary solutions (open circles) in Figure 6. Owing to a power-law dependence of the the first and second Kramers–Moyal parameterization, as for the PSP analysis by Benella et al. (2022), near the Sun with $\kappa \sim 2$ for scales up to $\tau \sim 0.05$ s, the MMS data exhibit a universal global scale invariance mainly at 1 au up to $\tau \sim 50\Delta t_B \sim 0.4$ s, where we have clear kappa distributions but with some larger values of $\kappa \sim 10$. Since for somewhat larger scales from $\tau_G \sim 100\Delta t_B \sim 0.8$ s (not shown here) the respective kappa distributions are very close to a limiting

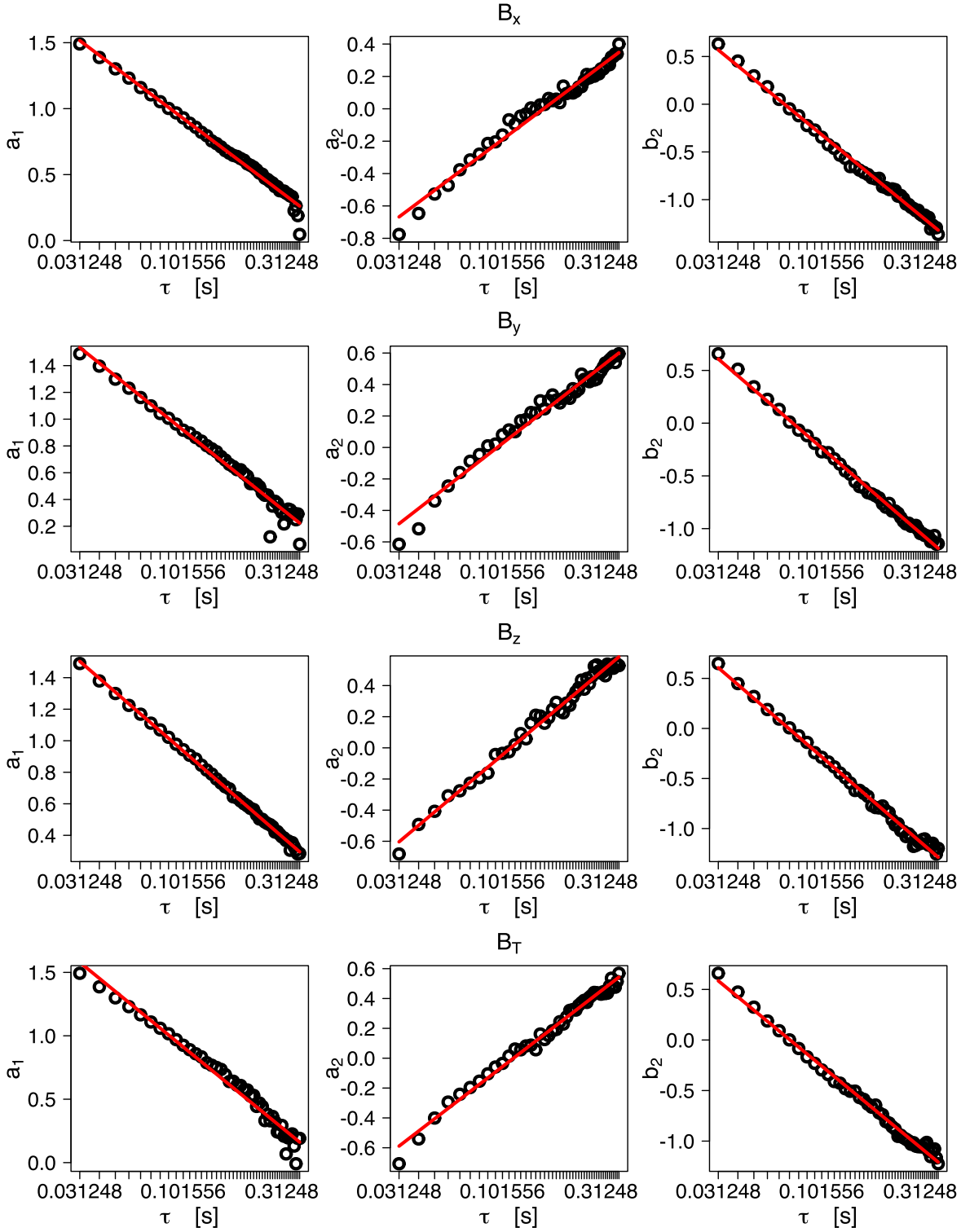

Figure 5. Linear dependence of the parameters a_1, a_2, and b_2 on the logarithmic scale τ. See Equations (11) and (12) for all components of the magnetic field $\boldsymbol{B} = (B_x, B_y, B_z)$ and the total magnitude $B_T = |\boldsymbol{B}|$.

Gaussian shape, this would result in some more deviations from the global scale invariance (not only on tails).

Our results demonstrate that the energy transfer among the different scales is essentially a stochastic process that can be modeled by the Fokker–Planck advection-diffusion equation also in the kinetic regime. As we already suggested in our earlier analysis for inertial range of scales (Strumik & Macek 2008a, 2008b), because the transfer among the different scales is a stochastic "memoryless" process, we should expect a universal structure in the turbulent dynamics. This is actually shown by our statistical analysis of the PDFs up to kinetic scales.

5. Conclusions

MMS and PSP missions with unprecedented high millisecond time resolution of magnetometer data allow us to

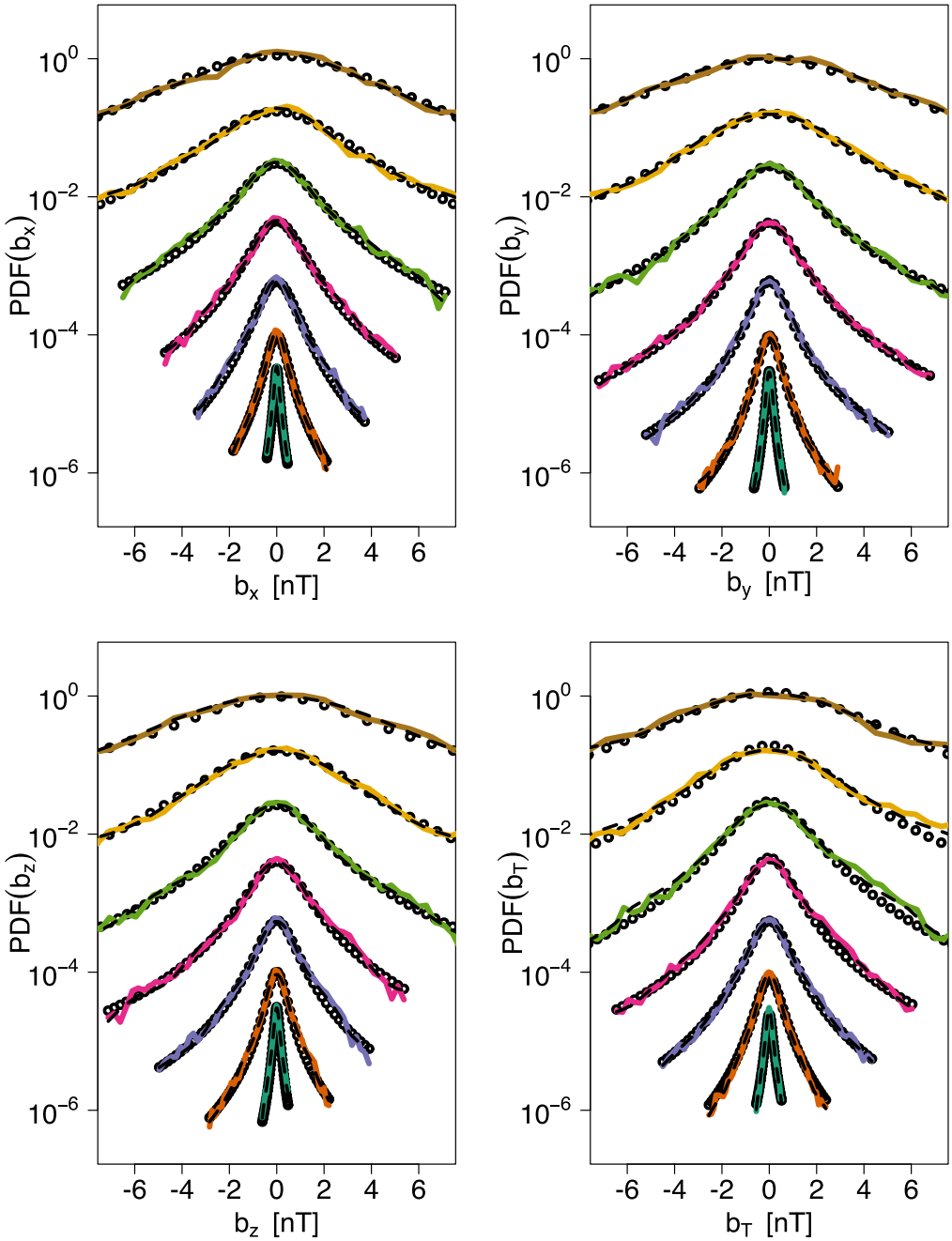

Figure 6. Comparison of the nonstationary (dashed lines) and stationary (open circles) solutions of the Fokker–Planck equation with the experimental PDFs of the magnetic field components $P(\boldsymbol{b}, \tau)$ fluctuations (continuous colored lines) for all components of the magnetic field $\boldsymbol{B} = (B_x, B_y, B_z)$ and the total magnitude $B_T = |\boldsymbol{B}|$ in the magnetosheath behind the BS using the MMS data, corresponding to spectra in Figure 1, for various scales (shifted from bottom to top) $\tau = 0.0078$, 0.04, 0.078, 0.12, 0.2, 0.39, and 0.78 s.

investigate turbulence on very small kinetic scales. In this paper we have looked at the MMS observations above 20 Hz, where the magnetic spectrum becomes very steep with the slope, close to $-16/3$, resulting possibly from interaction between coherent structures.

Following our previous studies in the inertial region (Strumik & Macek 2008a, 2008b) we have shown for the first time that the Chapman–Kolmogorov equation, which is a necessary condition for the Markovian character of turbulence, is satisfied, exhibiting a local transfer mechanism of turbulence cascade also on much smaller kinetic scales. Moreover, we have verified that in this case the Fokker–Planck equation is reduced to drift and diffusion terms at least for scales smaller than 0.8 s.

In particular, similarly as for PSP data analyzed by Benella et al. (2022), these lowest-order coefficients are linear and quadratic functions of magnetic field, which correspond to the generalized Ornstein–Uhlenbeck processes. We have also recovered a similar universal scale invariance of the PDFs up to kinetic scales of about 0.4 s.

It is interesting to note that for moderate scales we have also non-Gaussian (kappa) distribution, which for the smallest values of the available scale of 7.8 ms, is approximately described by a very peaked shape close to the Dirac delta

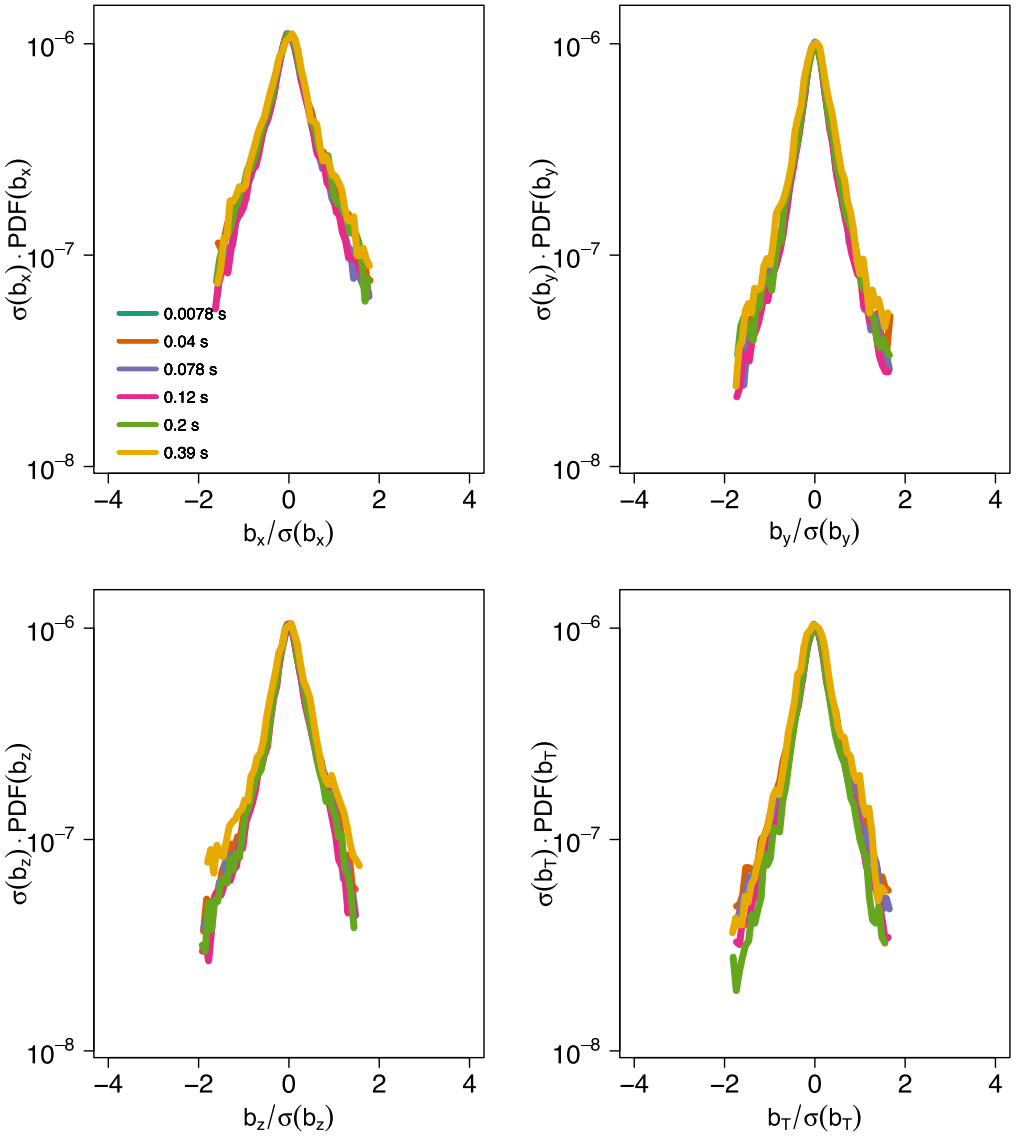

Figure 7. A universal scale invariance of the collapsing PDFs of $\boldsymbol{b}_\tau$ rescaled by the respective standard deviations $\sigma_{\boldsymbol{b},\tau}$, corresponding to the kappa distributions in Figure 6 on the kinetic scales up to $\tau \sim 0.4$ s.

function. We also show that the normal Gaussian distribution is recovered for timescales two orders larger (with a large value of the kappa parameter).

We hope that our observation of Markovian futures in solar wind turbulence will be important for understanding the relationship between deterministic and stochastic properties of turbulence cascade at kinetic scales in complex astrophysical systems.

We thank Marek Strumik for discussion on the theory of Markov processes. We are grateful for the dedicated efforts of the entire MMS mission team, including development, science operations, and the Science Data Center at the University of Colorado. We especially benefited from the efforts of T. E. Moore as Project Scientist, C. T. Russell, and the magnetometer team for providing the magnetic field data from http://cdaweb.gsfc.nasa.gov. We acknowledge B. L. Giles, Project Scientist for information about the magnetic field instrument, and also D. G. Sibeck and M. V. D. Silveira for discussions during previous visits by W.M.M. to the NASA Goddard Space Flight Center. We would like to thank the referee for inspiring comments, especially on the universal scale invariance through the kinetic domain. This work has been supported by the National Science Centre, Poland (NCN), through grant No. 2021/41/B/ST10/00823.

ORCID iDs

Wiesław M. Macek https://orcid.org/0000-0002-8190-4620
Dariusz Wójcik https://orcid.org/0000-0002-2658-6068
James L. Burch https://orcid.org/0000-0003-0452-8403

References

Benella, S., Stumpo, M., Consolini, G., et al. 2022, ApJL, 928, L21
Biskamp, D. 2003, Magnetohydrodynamic Turbulence (Cambridge: Cambridge Univ. Press)
Bruno, R., & Carbone, V. 2016, Turbulence in the Solar Wind, Lecture Notes in Physics, Vol. 928 (Berlin: Springer)
Burch, J. L., Moore, T. E., Torbert, R. B., & Giles, B. L. 2016, SSRv, 199, 5
Chang, T. T. S. 2015, An Introduction to Space Plasma Complexity (Cambridge: Cambridge Univ. Press)
Dickey, D. A., & Fuller, W. A. 1979, JASA, 74, 427

Echim, M., Chang, T., Kovacs, P., et al. 2021, Magnetospheres in the Solar System (Washington, DC: American Geophysical Union), 67
Frisch, U. 1995, Turbulence. The Legacy of A.N. Kolmogorov (Cambridge: Cambridge Univ. Press)
Macek, W. M., Krasińska, A., Silveira, M. V. D., et al. 2018, ApJL, 864, L29
Macek, W. M., Silveira, M. V. D., Sibeck, D. G., Giles, B. L., & Burch, J. L. 2019a, GeoRL, 46, 10295
Macek, W. M., Silveira, M. V. D., Sibeck, D. G., Giles, B. L., & Burch, J. L. 2019b, ApJL, 885, L26
Macek, W. M., Wawrzaszek, A., & Burlaga, L. F. 2014, ApJL, 793, L30
Macek, W. M., Wawrzaszek, A., & Carbone, V. 2011, GeoRL, 38, L19103
Macek, W. M., Wawrzaszek, A., & Carbone, V. 2012, JGRA, 117, 12101
Macek, W. M., Wawrzaszek, A., Kucharuk, B., & Sibeck, D. G. 2017, ApJL, 851, L42
Macek, W. M., Wawrzaszek, A., & Sibeck, D. G. 2015, JGRA, 120, 7466
Papini, E., Cicone, A., Franci, L., et al. 2021, ApJL, 917, L12
Pedrizzetti, G., & Novikov, E. A. 1994, JFM, 280, 69
Renner, C., Peinke, J., & Friedrich, R. 2001, JFM, 433, 383
Rinn, P., Lind, P., Wächter, M., & Peinke, J. 2016, JORS, 4, e34
Risken, H. 1996, The Fokker–Planck Equation: Methods of Solution and Applications, Springer Series in Synergetics (Berlin: Springer)
Russell, C. T., Anderson, B. J., Baumjohann, W., et al. 2016, SSRv, 199, 189
Schekochihin, A. A., Cowley, S. C., Dorland, W., et al. 2009, ApJS, 182, 310
Strumik, M., & Macek, W. M. 2008a, PhRvE, 78, 026414
Strumik, M., & Macek, W. M. 2008b, NPGeo, 15, 607
Wawrzaszek, A., & Macek, W. M. 2010, JGRA, 115, A07104
Welch, P. D. 1967, IEEE Trans. Audio Electroacoust., 15, 70

Monthly Notices of the ROYAL ASTRONOMICAL SOCIETY

MNRAS **526,** 5779–5790 (2023) https://doi.org/10.1093/mnras/stad2584
Advance Access publication 2023 September 4

Statistical analysis of stochastic magnetic fluctuations in space plasma based on the *MMS* mission

Wiesław M. Macek [1,2]★ and Dariusz Wójcik [1,2]★

[1] *Institute of Physical Sciences, Faculty of Mathematics and Natural Sciences, Cardinal Stefan Wyszyński University, Wóycickiego 1/3, PL-01-938 Warsaw, Poland*
[2] *Space Research Centre, Polish Academy of Sciences, Bartycka 18A, PL-00-716 Warsaw, Poland*

Accepted 2023 August 20. Received 2023 August 12; in original form 2023 May 17

ABSTRACT

Based on the *Magnetospheric Multiscale* (*MMS*) mission we look at magnetic field fluctuations in the Earth's magnetosheath. We apply the statistical analysis using a Fokker–Planck equation to investigate processes responsible for stochastic fluctuations in space plasmas. As already known, turbulence in the inertial range of hydromagnetic scales exhibits Markovian features. We have extended the statistical approach to much smaller scales in space, where kinetic theory should be applied. Here we study in detail and compare the characteristics of magnetic fluctuations behind the bow shock, inside the magnetosheath, and near the magnetopause. It appears that the first Kramers–Moyal coefficient is linear and the second term is a quadratic function of magnetic increments, which describe drift and diffusion, correspondingly, in the entire magnetosheath. This should correspond to a generalization of Ornstein–Uhlenbeck process. We demonstrate that the second-order approximation of the Fokker–Planck equation leads to non-Gaussian kappa distributions of the probability density functions. In all cases in the magnetosheath, the approximate power-law distributions are recovered. For some moderate scales, we have the kappa distributions described by various peaked shapes with heavy tails. In particular, for large values of the kappa parameter this shape is reduced to the normal Gaussian distribution. It is worth noting that for smaller kinetic scales the rescaled distributions exhibit a universal global *scale invariance*, consistently with the stationary solution of the Fokker–Planck equation. These results, especially on kinetic scales, could be important for a better understanding of the physical mechanism governing turbulent systems in space and astrophysical plasmas.

Key words: magnetic fields – turbulence – methods: data analysis – methods: statistical – Sun: heliosphere – solar wind.

1 INTRODUCTION

Turbulence is a complex phenomenon that notwithstanding progress in (magneto)hydrodynamic simulations is still a challenge for natural sciences (Frisch 1995), and physical mechanisms responsible for turbulence cascade are not clear (Biskamp 2003). Fortunately, collisionless solar wind plasmas can be considered natural laboratories for investigating this complex dynamical system (Bruno & Carbone 2016). Fluctuations of magnetic fields play an important role in space plasmas, leading also to a phenomenon known as magnetic reconnection (e.g. Burlaga 1995; Treumann 2009).

Turbulent magnetic reconnection is a process in which energy can proficiently be shifted from a magnetic field to the motion of charged particles. Therefore, this process responsible for the redistribution of kinetic and magnetic energy in space plasmas is pivotal to the Sun, Earth, and to other planets and generally across the whole Universe. Reconnection also impedes the effectiveness of fusion reactors and regulates geospace weather that can affect contemporary technology such as the Global Positioning System (GPS) navigation, modern mobile phone networks, including electrical power grids. Electric fields responsible for reconnection in the Earth's magnetosphere have been observed on kinetic scales by the *Magnetospheric Multiscale* (*MMS*) mission (Macek et al. 2019a,b). Certainly, reconnection in the magnetosphere is related to turbulence at small scales (Karimabadi et al. 2014).

Basically, in a Markov process, given an initial probability distribution function (PDF), the transition to the next stage can fully be determined. It is also interesting here that we can prove and demonstrate the existence of such a Markov process experimentally. Namely, without relying on any assumptions or models for the underlying stochastic process, we are able to extract the differential equation of this Markov process directly from the collected experimental data. Hence this Markov approach appears to be a bridge between the statistical and dynamical analysis of complex physical systems. There is substantial evidence based on statistical analysis that stochastic fluctuations exhibit Markov properties (Pedrizzetti & Novikov 1994; Renner, Peinke & Friedrich 2001). We have already proved that turbulence has Markovian features in the inertial range of hydromagnetic scales (Strumik & Macek 2008a,b). Admittedly, for turbulence inside the inertial region of magnetized plasma, the characteristic spectra should be close to standard Kolmogorov (1941) power-law type with exponent $-5/3 \approx -1.67$ (Kolmogorov 1941)

★ E-mail: macek@uksw.edu.pl, macek@cbk.waw.pl (WMM); dwojcik@cbk.waw.pl (DW)

and Kraichnan (1965) power-law spectrum with exponent −3/2, but surprisingly, the absence of these classical spectra, especially on smaller scales, seems to be the rule.

Moreover, we have also confirmed clear breakpoints in the magnetic energy spectra in the Earth's magnetosheath (SH), which occur near the ion gyrofrequencies just behind the bow shock (BS), inside the SH, and before leaving the SH. Namely, we have observed that the spectrum steepens at these points to power exponents in the kinetic range from −5/2 to −11/2 for the magnetic field data of the highest resolution available within the *MMS* mission (Macek et al. 2018). Therefore, we would like to investigate the Markov property of stochastic fluctuations outside this inertial region of magnetized plasma on small scales, when the slopes are consistent with kinetic theory.

It should also be noted that based on the measurements of magnetic field fluctuations in the Earth's SH gathered onboard the *MMS* mission, we have recently extended these statistical results to much smaller scales, where kinetic theory should be applied (Macek, Wójcik & Burch 2023). Here we compare the characteristics of stochastic fluctuations behind the BS, inside the SH, and near the magnetopause (MP). In this paper, we therefore present the results of our comparative analysis, where we check whether the solutions of the Fokker–Planck (FP) equation are consistent with experimental PDFs in various regions of the SH.

In Section 2, a concise description of the *MMS* mission and the analysed data is provided, while the Section 3 outlines used stochastic mathematical and statistical methods. The vital results of our analysis are presented in Section 4, which demonstrates that the solutions of the FP equation are in good agreement with empirical PDFs. Finally, Section 5 emphasizes the significance of stochastic Markov processes in relation to turbulence in space plasmas, which exhibit a universal global *scale invariance* across the kinetic domain.

2 DATA

The *MMS* mission, which began in 2015 March 12 and is still in operation, delves into the connection and disconnection of the Sun's and Earth's magnetic fields. Four spacecraft (namely *MMS 1–MMS 4*), which carry identical instrument suites, are orbiting near the equator to observe magnetic turbulence in progress. They are formed into a pyramid-like formation. Each satellite has an octagonal form that is around 3.5 m in breadth and 1.2 m in height. The satellites rotate at 3 revolutions min^{-1} during scientific operations. Position data are supplied by ultraprecise GPS apparatus, while attitude is sustained by four stellar trackers, two accelerometers, and two solar sensors. All of the spacecraft have identical instruments to measure plasmas, magnetic and electric fields, and other particles with remarkably high (milliseconds) time resolution and accuracy. This allows us to figure out if reconnection takes place in an individual area, everywhere within a broader area simultaneously, or traversing through space. The *MMS* studies the reconnection of the solar and terrestrial magnetic fields in both the day and night sides of Earth's magnetosphere, which is the only place where it can be directly observed by spacecraft. In our previous studies, we have observed reconnection in the Earth's magnetosphere involving small kinetic scales (Macek et al. 2019a,b).

We have further examined fluctuations of all components of the magnetic fields $\boldsymbol{B} = (B_x, B_y, B_z)$ in the Geocentric Solar Ecliptic (GSE) coordinates, with the magnitude strength $B = |\boldsymbol{B}|$ (square root of the sum of the squares of the field components), which have been taken from the *MMS* Satellite No. 1 (*MMS 1*), located just beyond the Earth's BS. In this way, we have shown that magnetic fluctuations exhibit Markov character also on very small kinetic scales (Macek et al. 2023). Moreover, we have noticed that in all components the Markovian features are quite similar. Here, we would like to further investigate statistical properties of magnetic fluctuations in various regions of the SH. The spacecraft trajectories in the SH, in three different regions, namely

(a) just behind the BS
(b) deep inside the SH, and
(c) near the MP,

which have been shown in fig. 1 of Macek et al. (2018).

Therefore, we would like to look at the measurements of the magnetic field strength $B = |\boldsymbol{B}|$, but now at various regions of the SH. To investigate SH stochastic fluctuations, now we have chosen the same three different time intervals samples, which correspond to table 1 of Macek et al. (2018). In cases (a) and (c) of approximately 5 and 1.8 min respective intervals, we use burst-type observations from the fluxgate magnetometer (FGM) sensor with the highest resolution (Δt_B) of 7.8 ms (128 samples s^{-1}) with 37 856 and 13 959 data points, correspondingly. However, in the other case (b), between the BS and the MP, where only substantially lower resolution 62.5–125 ms in survey mode (8–16 samples s^{-1}) data are available, we have a much longer interval lasting 3.5 h with 198 717 data points with $\Delta t_B = 62.5$ s. All of the data are publicly available on the website: http://cdaweb.gsfc.nasa.gov, which is hosted by the National Aeronautics and Space Administration (NASA) (Burch et al. 2016).

Admittedly, the gaps in time series, which commonly appear in the data gathered from space missions, can have a considerable impact on the conclusions that can be derived from statistical analysis based on experimental data. One of the powerful but simple tools used to cope with this problem is a linear interpolation method between points, which we have used, if necessary, to fill these gaps in the analysed data sets. Therefore, in Fig. 1 on the upper side of each case (a)–(c) from left to right, we have depicted time series of the magnetic field strength $B = |\boldsymbol{B}|$. Whereas on the bottom side of each case, we have shown the respective power spectral density (PSD) obtained using the method proposed by Welch (1967).

The calculated average ion and electron gyrofrequencies are as follows: in case (a) $f_{ci} = 0.25$ Hz, and $f_{ce} = 528$ Hz; case (b) $f_{ci} = 0.24$ Hz and $f_{ce} = 510$ Hz; and case (c) $f_{ci} = 0.29$ Hz and $f_{ce} = 609$ Hz (Macek et al. 2018). In addition, employing the hypothesis according to Taylor (1938), relating time and space scales in this way: $l = v_{sw}\,\tau$, where l is a spatial scale and v_{sw} is the mean velocity of the solar wind flow in the SH, we estimate characteristic inertial frequencies for ions and electrons: in case (a) $f_{\lambda i} = 0.55$ Hz and $f_{\lambda e} = 24.5$ Hz; case (b) $f_{\lambda i} = 0.41$ Hz and $f_{\lambda e} = 18.1$ Hz; and case (c) $f_{\lambda i} = 0.45$ Hz and $f_{\lambda e} = 20.1$ Hz. We have marked these values on each graph of PSD. In case (a) the obtained spectral exponent is about -2.60 ± 0.06 somewhat steeper, before the $f_{\lambda e} = 24.5$ Hz threshold and undoubtedly more steepen than the Kolmogorov (1941) (−5/3) or Kraichnan (1965) (−3/2) slopes.

On the other hand, outside the inertial range of scales large spectral exponents has been reported from the *Cluster* multispacecraft mission (Sahraoui et al. 2009), the *WIND* data (Bruno, Trenchi & Telloni 2014), including the proposed explanation of nature of solar wind magnetic fluctuations on kinetic scales based on the missions (e.g. Lion, Alexandrova & Zaslavsky 2016; Roberts et al. 2016). Owing to unprecedented high 7.8 ms time resolution of magnetometer data in the *MMS* mission available in burst mode, we also see that in case (a) the slope is of -2.60 ± 0.06 (close to −5/2) above $f_{\lambda e} = 24.5$ Hz. This is further followed by an even steeper spectrum with the slope of -5.59 ± 0.32 (close to −11/2 or −16/3). Because

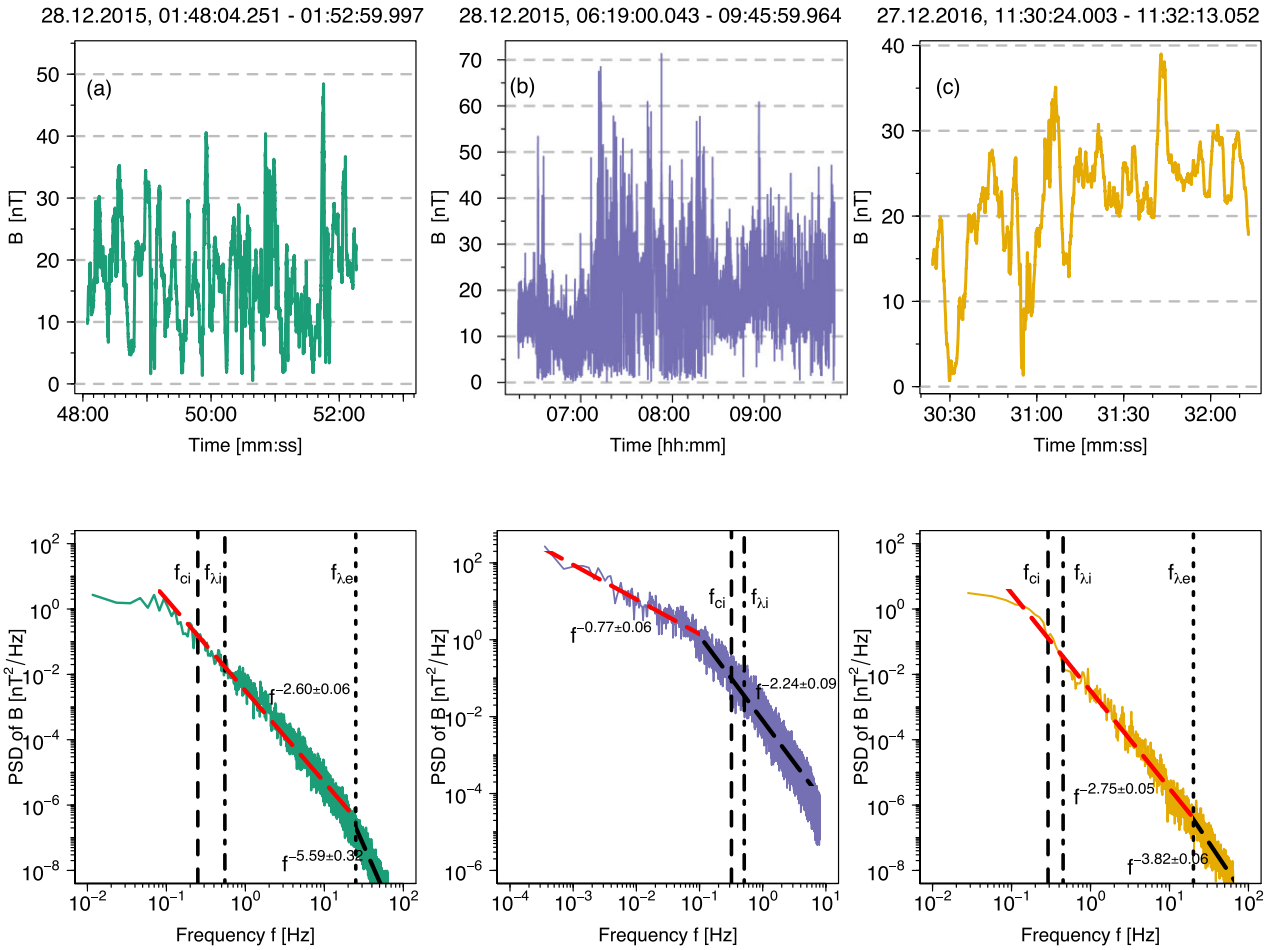

Figure 1. Time series of the magnetic field strength $B = |\boldsymbol{B}|$ of the *MMS* data with the corresponding spectra in the SH (a) near the BS, (b) inside the SH, and (c) near the MP plotted with three different colours. Average ion gyrofrequency ($f_{\rm ci}$), and a characteristic Taylor's shifted frequencies for ions ($f_{\lambda \rm i}$) and electrons ($f_{\lambda \rm e}$) are shown by the dashed, dashed–dotted, and dotted lines, respectively; see table 1 of Macek et al. (2018).

of a substantially lower survey data resolution of 62.5 ms in case (b) the spectrum with -2.24 ± 0.09 ($\approx -7/3$) is steeper than the Kolmogorov (1941) ($-5/3$) spectrum only after the visible breakpoint in the slope, which lies at $f = 0.12$ Hz, i.e. near the ion gyrofrequency $f_{\rm ci} = 0.24$ Hz, while more gentle slope of -0.77 ± 0.06 is observed before this breakpoint. Finally, in case (c), similarly as in case (a) using BURST data, the spectral exponent of -2.75 ± 0.05 is again steeper before, and even more with the exponent -3.82 ± 0.06 (close to $-7/2$) after the observed breakpoint that lies at around the electron Taylor's (1938) shifted frequency $f_{\lambda \rm e} = 20$ Hz, as discussed by Macek et al. (2018). This shows that the observed stochastic nature of fluctuations in the subion scale could be due to the interaction between coherent structures (Perrone et al. 2016, 2017), and a very high slope of $-16/3$ is possibly related to the dissipation of the kinetic Alfvén waves (e.g. Schekochihin et al. 2009).

3 METHODS OF DATA ANALYSIS

As usual, we use the fluctuations of the magnetic fields $B = |\boldsymbol{B}|$, which describe this turbulent system at each time $t > 0$. Therefore, with a given time-scale $\tau_i > 0\ \forall_i$, one can typically define the increments of this quantity as follows:

$$b_i(t) := B(t + \tau_i) - B(t), \tag{1}$$

and, assuming an arbitrary $\tau_i > 0$, it can be labelled as b_τ or b for simplicity in the following sections.

We assume that the fluctuations of increment b_τ in a larger time-scale τ are transferred to smaller and smaller scales. Therefore, stochastic fluctuations may be regarded as a stochastic process in scale with the N-point joint (transition) conditional probability density function denoted by $P(b_1, \tau_1 | b_2, \tau_2, \ldots, b_N, \tau_N)$. In this case, the conditional probability density function is defined by default as

$$P(b_i, \tau_i | b_j, \tau_j) = \frac{P(b_i, \tau_i; b_j, \tau_j)}{P(b_j, \tau_j)}, \tag{2}$$

with the marginal (unconditional) probability density function, $P(b_j, \tau_j)$, and the joint probability function, $P(b_i, \tau_i; b_j, \tau_j)$, of finding the fluctuations b_i at a scale τ_i and b_j at a scale τ_j, for $0 < \tau_i < \tau_j$. In the same way, we may construct the conditional probability densities for any longer sequences of increments b.

The stochastic process is Markovian if the conditional probability function depends only on the initial values b_1 and b_2 at the time-scales τ_1 and τ_2, but not on b_3 at the next larger scale τ_3, and so on, i.e. for any $i = 1, \ldots, N$ we have

$$P(b_1, \tau_1 | b_2, \tau_2) = P(b_1, \tau_1 | b_2, \tau_2, ..., b_N, \tau_N) \tag{3}$$

for $0 < \tau_1 < \tau_2 < \cdots < \tau_N$. Basically, the Markov process can be determined by the initial conditional probability function $P(b_1, \tau_1 | b_2, \tau_2)$. Strictly speaking, the future states of the process

are conditionally independent of past states. Because of this relation, the conditional probabilities are also called transition probabilities, while the property of equation (3) is known as a *memorylessness*.

One of the generalizations of equation (3) is called the Chapman–Kolmogorov (CK) condition, which is given by the equation (Risken 1996)

$$P(b_1, \tau_1|b_2, \tau_2) = \int_{-\infty}^{+\infty} P(b_1, \tau_1|b', \tau')P(b', \tau'|b_2, \tau_2)\,\mathrm{d}b' \tag{4}$$

for $\tau_1 < \tau' < \tau_2$. This equation can be interpreted in the following way: the transition probability from b_2 at a time-scale τ_2 to b_1 at a time-scale τ_1 is the same as a product of the transition probability from b_2 at a time-scale τ_2 to b' at a time-scale τ', and the transition probability from b' at a time-scale τ' to b_1 at a time-scale τ_1, for all possible b's. Let us emphasize here that such a generalization is a necessary condition for a stochastic process to be the Markov process.

Next, from the CK condition of equation (4), by using a standard series expansion, one can derive a corresponding Kramers–Moyal (KM) backward expansion with an infinite number of terms. Backward expansions are equations of evolution of probability $P(b, \tau|b', \tau')$, where we differentiate with respect to b. This equation has the following differential form (see section 4.2 of Risken 1996):

$$-\frac{\partial}{\partial\tau}P(b, \tau|b', \tau') = \sum_{k=1}^{\infty}\left(-\frac{\partial}{\partial b}\right)^k D^{(k)}(b, \tau)P(b, \tau|b', \tau'), \tag{5}$$

where it is important to note that the differential symbol acts on both $D^{(k)}(b, \tau)$ and $P(b, \tau|b', \tau')$ coefficients. Since the solutions of the forward and backward KM equations are equivalent, then without loss of generality, we can label it as KM expansion. Formally, $D^{(k)}(b, \tau)$ are called KM coefficients, which in this way are defined as the limit at $\tau \to \tau'$ of kth power of conditional moments (see Risken 1996):

$$D^{(k)}(b, \tau) = \frac{1}{k!}\lim_{\tau\to\tau'}\frac{1}{\tau - \tau'}M^{(k)}(b, \tau, \tau'), \tag{6}$$

$$M^{(k)}(b, \tau, \tau') = \int_{-\infty}^{+\infty}(b' - b)^k P(b', \tau'|b, \tau)\,\mathrm{d}b'. \tag{7}$$

Ideally, using the conditional moments $M^{(k)}(b, \tau, \tau')$, the KM coefficients can be evaluated, though they cannot be obtained directly from the analysed data. While these conditional moments can be calculated from the empirical observations, the $D^{(k)}(b, \tau)$ coefficients can only be obtained by extrapolation in the limit $\tau \to \tau'$ according to equations (6) and (7), but these formulae cannot be applied explicitly.

One of the popular extrapolation methods for this problem is a use of piecewise linear regression model with breakpoints. This is a type of regression model, which allows multiple linear models to fit to the analysed data. The crucial objective of this method is an accurate estimation of a number of breakpoints. First, in order to estimate the best breakpoint position, we have evaluated every value within a specified interval and looked at the value of logarithmic transformation of the likelihood function (also known as *log-likelihood* function) of each adjusted model. Naturally, the highest value of this function provides the optimal breakpoint. Further, to select (and estimate) the best possible number of breakpoints of the segmented relationship, we have used the standard Akaike (1973) information criterion (AIC) and Bayesian information criterion (BIC; Schwarz 1978). None the less, the truly similar results are obtained when the lowest time resolution is taken. Thus, in our case, we have a simple approximation of the KM coefficients, which is given by

$$D^{(k)}(b, \tau) = \frac{1}{k!}\frac{1}{\Delta t}M^{(k)}(b, \tau, \tau'), \tag{8}$$

where Δt is a given lowest time resolution of the time series. It is also interesting to note that $D^{(k)}(b, \tau)$ coefficients show the same dependence on b as $M^{(k)}(b, \tau, \tau')$. This simplification substantially decreases the time required to obtain the results numerically.

Now, in order to find the solution of equation (5), it is necessary to determine the number of terms of the right-hand side (RHS) of this equation that needs to be considered. According to Pawula's theorem, the KM expansion of a positive transition probability $P(b, \tau|b', \tau')$ may end after the first or second term (e.g. Risken 1996, section 4.3). If it does not end after the second term, then the expansion must contain an infinite number of terms. On the other hand, if the second term is the last one, namely $D^{(k)}(b, \tau) = 0$ for $k \geq 3$, then the KM expansion of equation (5) leads to the following particular formula:

$$-\frac{\partial}{\partial\tau}P(b, \tau|b', \tau') = \left[-\frac{\partial}{\partial b}D^{(1)}(b, \tau) + \frac{\partial^2}{\partial b^2}D^{(2)}(b, \tau)\right] \times P(b, \tau|b', \tau'), \tag{9}$$

with the well-known FP operator $\mathcal{L}_{\mathrm{FP}}(b, \tau)$ in the squared parenthesis (e.g. Risken 1996, equations 5.1 and 5.2) governing the evolution of the probability density function $P(b, \tau|b', \tau')$ and is called the FP equation (also known as a forward Kolmogorov equation). It has been primarily used for the Brownian motion of particles, but now equation (9) defines a generalized Ornstein–Uhlenbeck process. Strictly speaking, this is a linear second-order partial differential equation of a parabolic type. By solving the FP equation, it is possible to find distribution functions from which any averages (expected values) of macroscopic variables can be determined by integration. If the relevant time-dependent solution is provided, this equation can be used to not only describe stationary features, but also the dynamics of systems.

The first term, $D^{(1)}(b, \tau)$, and the second term, $D^{(2)}(b, \tau) > 0$, determining the FP equation (9) are responsible for the drift and diffusion processes, respectively. The former process accounts for the deterministic evolution of the stochastic process (as a function of b and τ). The latter process modulates the amplitude of the δ-correlated Gaussian noise $\Gamma(\tau)$ (which is known as the Langevin force – the fluctuating force $F_{\mathrm{f}}(\tau)$ per unit mass m), that fulfils the normalization conditions: $\langle\Gamma(\tau)\Gamma(\tau')\rangle = 2\delta(\tau - \tau')$, where δ is a Dirac delta function and $\langle\Gamma(\tau)\rangle = 0$ (see Risken 1996). Thus, in the equivalent approach another complementary equation arises:

$$-\frac{\partial b}{\partial\tau} = D^{(1)}(b, \tau) + \sqrt{D^{(2)}(b, \tau)}\,\Gamma(\tau), \tag{10}$$

which is formally called the Langevin equation. Here we have used the Itô (1944) definition that is missing a spurious drift (e.g. Risken 1996, section 3.3.3), hence the drift coefficient $D^{(1)}$ occurs directly, unlike in the Stratonovich (1968) definition. Admittedly, the Itô (1944) definition is more difficult to interpret and analyse, because of the new rules for integration and differentiation that must be used. Although, owing to a powerful apparatus, which is the Itô Lemma, it allows us to deal with stochastic processes analytically. Anyway, here again, all higher KM coefficients $D^{(k)}$ for $k \geq 3$ are equal to zero. Note that the negative signs on the left-hand side (LHS) of equations (9) and (10) show that the corresponding transitions proceed backward to smaller and smaller scales.

Next, because the differentiating in the FP operator in equation (9) should act on both the KM coefficients and the conditional

probability density $P(b,\,\tau|b^{'},\,\tau^{'})$ by performing relatively simple transformations, it can be rewritten in the following expanded form (equation 45.3a of Risken 1996):

$$-\frac{\partial}{\partial\tau}P(b,\tau|b',\tau') = D^{(2)}(b,\tau|b',\tau')\frac{\partial^2}{\partial b^2}P(b,\tau|b',\tau') + \left[2\frac{\partial}{\partial b}D^{(2)}(b,\tau|b',\tau') - D^{(1)}(b,\tau|b',\tau')\right]\frac{\partial}{\partial b}P(b,\tau|b',\tau') + \left[\frac{\partial^2}{\partial b^2}D^{(2)}(b,\tau|b',\tau') - \frac{\partial}{\partial b}D^{(1)}(b,\tau)\right]P(b,\tau|b',\tau'). \quad (11)$$

Formally, equation (11) resulting from the FP equation (9) is the second-order parabolic partial differential equation.

It is also worth mentioning that this equation is the generalization of the case of thermal conductivity diffusion equation, which can be solved with the initial and boundary conditions $P(b,\,\tau=0|b^{'},\,\tau^{'}=0)=p(b,\,b^{'})$ and $P(b=0,\,\tau|b^{'}=0,\,\tau^{'})=0$, respectively, using the method of separation of variables. The solution of non-stationary FP equation (11) can well be approximated numerically, i.e. by the difference method. The master curve for the probability density function $P(b,\,\tau)$ of equation (11) can readily be evaluated by the stationary solution $p_{\rm s}(b,\,\tau)$ of equation (9), which is given by

$$\frac{\partial}{\partial b}\left[D^{(2)}(b,\tau)p_{\rm s}(b,\tau)\right] = D^{(1)}(b,\tau)p_{\rm s}(b,\tau) \quad (12)$$

that results from comparing the LHS of equation (9) with zero.

4 RESULTS

In order to inspect processes responsible for stochastic fluctuations in space plasma, we have applied the methods described in Section 3 to small scale in cases (a) and (c) and medium scale in case (b) fluctuations of the magnetic field $B=|\boldsymbol{B}|$ in the Earth's SH. In general, the approach presented in this paper could be applied under a few important conditions that should be tested as preliminary procedures (see Rinn et al. 2016). The first condition is that time series data must be stationary. If they were non-stationary, then the conditional moments given by equation (7) are not essentially meaningful. The second condition is that the process should be Markovian, i.e. the present state should only depend on the preceding state. The third condition is that the Pawula's theorem must hold, as discussed in Section 3.

Having this in mind, we have started with the brief analysis and description of the relevant time series and the corresponding graphs of power spectral densities. Next, we have checked stationarity of all analysed time series (see e.g. Macek 1998). To show that a Markov processes approach is suitable in our situation, we have moved forward to the verification of the necessary CK condition, through estimation of the KM coefficients, and then have checked the validity of the Pawula's theorem. This lets us to apply the reduced formula of the FP equation (9), which describes evolution of the probability density function $P(b,\,\tau)$.

Following our initial discussion, we must now verify whether the data time series under study is stationary. Generally, if a time series exhibits no trend, has a constant variance over time, and a consistent autocorrelation function over time, then it is classified as stationary. Such time series are also much easier to model. There are a variety of ways to evaluate this feature of any time series. One of such method is the augmented Dickey & Fuller (1979) test. This test uses the following null and alternative hypotheses: $\rm H_0$: the time series is non-stationary, versus $\rm H_1$: the time series is stationary. When the p-value is less than 0.05, then the null hypothesis can be rejected and it can be concluded that the time series is stationary. In fact, after performing such a statistical test, we have determined that in cases (a) and (b), the respective p-values are <0.01, indicating that the null hypothesis can be rejected. Thus, these magnetic field strength $B=|\boldsymbol{B}|$ time series are stationary. However, in case (c), where a much smaller data sample is available, the p-value is equal to 0.154, hence we have failed to reject the null hypothesis. The result suggests that the time series is non-stationary and has some time-dependent structure with varying variance over time.

Once again, there are various methods of eliminating trends and seasonality, which define non-stationary time series. Trends can cause the mean to fluctuate over time, while seasonality can lead to changes in the variance over time. The most straightforward approach to address this issue is the differencing technique, a common and frequently used data transformation that is applied for making time series data stationary. Differencing is achieved by subtracting the previous observation from the current one. Following notation in equation (1), this can simply be written as $b(t)=B(t)-B(t-1)$. To reverse this process, the prior time-step's observation must be added to the difference value. The practice of computing the difference between successive observations is referred to as a `lag-1` difference. The number of times that differencing is carried out is referred to as the order of differentiation. Fortunately, in our case (c), applying the `lag-1` (order 1) difference operation has been sufficient to get rid of non-stationarity. The augmented Dickey & Fuller (1979) test has yielded a p-value of less than 0.01, thus the null hypothesis could be rejected, indicating that the analysed $B=|\boldsymbol{B}|$ time series is stationary.

We have used one of the exploratory data analysis approaches called unsupervised binning method (compare with normalized histogram method) to make bins (histogram's boxes) and to obtain the empirical conditional probability density functions $P(b_1,\,\tau_1|b_2,\,\tau_2)$ for $0<\tau_1<\tau_2$ directly from the analysed data. First, we have estimated the empirical joint PDF $P(b_1,\,\tau_1;\,b_2,\,\tau_2)$ by counting the number of different pairs $(b_1,\,b_2)$ on a two-dimensional grid of equal width data bins (small intervals). This *bins* integer should be neither too large, such that each bin no longer contains a significant quantity of points, nor too small, such that any dependency of the drift and diffusion coefficients on the state variable cannot be detected. Next, we have performed the normalization such that the integral over all bins is equal to 1 (note that the sum will not be equal to 1 unless bins of unity width are chosen). Similarly, the empirical one-dimensional PDF $P(b_2,\,\tau_2)$ can be estimated with the use of a one-dimensional grid of bins (and carrying out the normalization), and the empirical conditional PDFs are obtained using equation (2) directly (in a numerical sense).

In such a way, we have found the empirical conditional probability density functions from the analysed data, which are shown by red continuous contours in Fig. 2. They are compared here with the theoretical conditional PDFs that are solutions of the CK condition of equation (4) displayed by blue dashed contours, which are two-dimensional representation of three-dimensional data. Such a comparison is seen in Fig. 2 for the magnetic field increments b, at the various scales: in cases (a) and (c) $\tau_1=0.02$ s, $\tau^{'}=\tau_1+\Delta t_B=0.0278$ s, $\tau_2=\tau_1+2\Delta t_B=0.0356$ s, where $\Delta t_B=0.0078$ s, and in case (b) $\tau_1=0.2$ s, $\tau^{'}=\tau_1+\Delta t_B=0.2625$ s, $\tau_2=\tau_1+2\Delta t_B=0.325$ s, where $\Delta t_B=0.0625$ s. The depicted subsequent isolines correspond to the following decreasing levels of the conditional PDFs, from the middle of the plots, for following magnetic field increments b: case (a) 2, 1.1, 0.5, 0.3, 0.05, 0.01; case (b) 5, 1, 0.7, 0.45, 0.3, 0.22, 0.15, 0.1, 0.05; and case (c) 7, 3.3, 1.3, 0.3, 0.08, 0.06. This is rather evident that the contour lines corresponding to these two empirical and theoretical probability distributions are

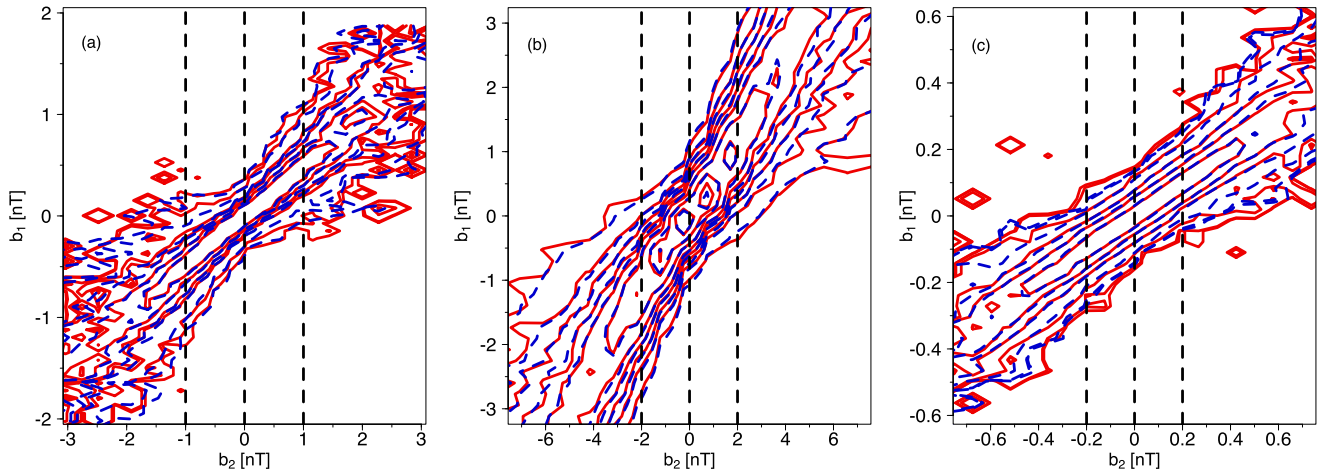

Figure 2. Comparison of observed contours (red solid curves) of conditional probabilities at various time-scales τ, with reconstructed contours (blue dashed curves) according to the Chapman–Kolmogorov (CK) condition, recovered by the use of *MMS* magnetic field total magnitude $B = |\boldsymbol{B}|$ in the SH: (a) just behind the BS, (b) inside the SH, and (c) near the MP, corresponding to the spectra in Fig. 1.

nearly matching for all three cases. Thus, it appears that the CK condition of equation (4) is sufficiently well satisfied.

Next, in the corresponding Fig. 3, we have verified again the CK condition of equation (4). Intuitively speaking (and somehow informally), what we see in Fig. 2 is just a view 'from the top' of the three-dimensional shape, while in Fig. 3 the orthogonal cuts are depicted. Again, we have compared these cuts through the conditional probability density functions for particular chosen values of parameter b_2, which can be seen at the top of each plot. As is evident, the cuts through the empirical probability density functions coincide rather well with the cuts through the theoretical probability density functions, providing good fits in all of the analysed cases. Admittedly, only in case (b) for $b_2 = 0$ [nT] the cuts points deviate from the lines in tails, but it seems to be caused by the data outliers, which can eventually be further eliminated. It is necessary to mention that after such a comparison for different values of (τ_1, τ', τ_2), we have found that the CK condition of equation (4) is satisfied for b up to a scale of approximately $100\Delta t_B = 0.78$ s in case (a), to about $150\Delta t_B = 9.375$ s in case (b), and around $40\Delta t_B = 0.312$ s in case (c), thus indicating that the stochastic fluctuations have Markov properties.

To verify Pawula's theorem, which states that if the fourth-order coefficient is equal to zero, then $D^{(k)}(b, \tau) = 0, k \geq 3$, it is necessary to estimate the $D^{(1)}(b, \tau)$, $D^{(2)}(b, \tau)$, and $D^{(4)}(b, \tau)$ coefficients using our experimental data. The standard procedure for calculating these values is to use an extrapolation method such as a piecewise linear regression to estimate the respective limits in equation (6). However, as already mentioned in Section 3, the similar results are obtained by simplifying the problem of finding these coefficients, by using equation (8), which enables us to estimate these values using the adequately scaled $M^{(k)}(b, \tau, \tau')$ coefficients. In our situation, the time resolution Δt_B is equal to 7.8 ms in cases (a) and (c), while in case (b) it is 62.5 ms. Thus, given the conditional probabilities $P(b_1, \tau_1|b_2, \tau_2)$ for $0 < \tau_1 < \tau_2$, we have calculated these central moments directly from equation (7), using the obtained empirical data by counting the numbers $N(b', b)$ of occurrences of two fluctuations b' and b. Given that the errors of $N(b', b)$ might be simply determined by $\sqrt{N(b', b)}$, then, in a similar way, it is possible to calculate the errors for the conditional moments $M^{(k)}(b, \tau, \tau')$. Consequently, scaling these values according to equation (8), we have obtained the empirical KM coefficients. By examination of the $M^{(k)}(b, \tau, \tau')$ and $D^{(k)}(b, \tau)$ coefficients, we can observe that they both exhibit the same dependence on b.

The results of this analysis are shown in Fig. 4, where on the upper part we have depicted the first-order coefficient depending on b, while at the bottom we have shown the second- and fourth-order coefficients depending on b, for all three cases (a), (b), and (c). Moreover, for each case, we have provided the calculated confidence intervals (error bars). It is demonstrated that the fit for $D^{(1)}(b, \tau)$ coefficient is a linear function of b and for $D^{(2)}(b, \tau)$ is a quadratic function of b, for $\Delta t_B = 0.0078$ s in cases (a) and (c), and $\Delta t_B = 0.0625$ s in case (b). In fact, we have checked that the same fits are reasonable up to even $150\Delta t_B$ for all three analysed cases. This means that in this instance, there should be no difficulties with fitting the polynomials for different Δt_B.

As seen at the bottom part of Fig. 4 of cases (a) and (c), it is evident that the Pawula's theorem is clearly satisfied. On the other hand, in case (b) it might be not so obvious. For instance, for $b \approx -6.2$ nT, we can see that the value of $D^{(4)}(b, \tau)$ is somewhat greater than zero. In this case, we can use the somewhat weaker version of this theorem, which states that it is sufficient to check if $D^{(4)}(b, \tau) \ll [D^{(2)}(b, \tau)]^2$, for all b (see Risken 1996; Rinn et al. 2016). Thus, in this situation, we have $[D^{(2)}(b, \tau)]^2 \approx 1225$, which is significantly larger than $D^{(4)}(b, \tau) \approx 1$, for $b \approx -6.2$ nT. Therefore, it is reasonable to conclude that the Pawula's theorem is sufficiently well fulfiled in all of the analysed cases. Hence we can assume that the Markov process is described by the FP equation (9).

In order to find the analytical solution of the FP equation (9), we have proposed certain approximations of the lowest order KM coefficients. As previously discussed (see Fig. 4), it is straightforward that $D^{(1)}(b, \tau)$ exhibits a linear dependence, whereas $D^{(2)}(b, \tau)$ displays a quadratic dependence on b. Consequently, it is reasonable to assume the following parametrization:

$$\begin{cases} D^{(1)}(b, \tau) = -a_1(\tau)b, \\ D^{(2)}(b, \tau) = a_2(\tau) + b_2(\tau)b^2, \end{cases} \tag{13}$$

where the relevant parameters $a_1 > 0$, $a_2 > 0$, and $b_2 > 0$ depend on temporal scale $\tau > 0$. Moreover, it appears that all of these parameters

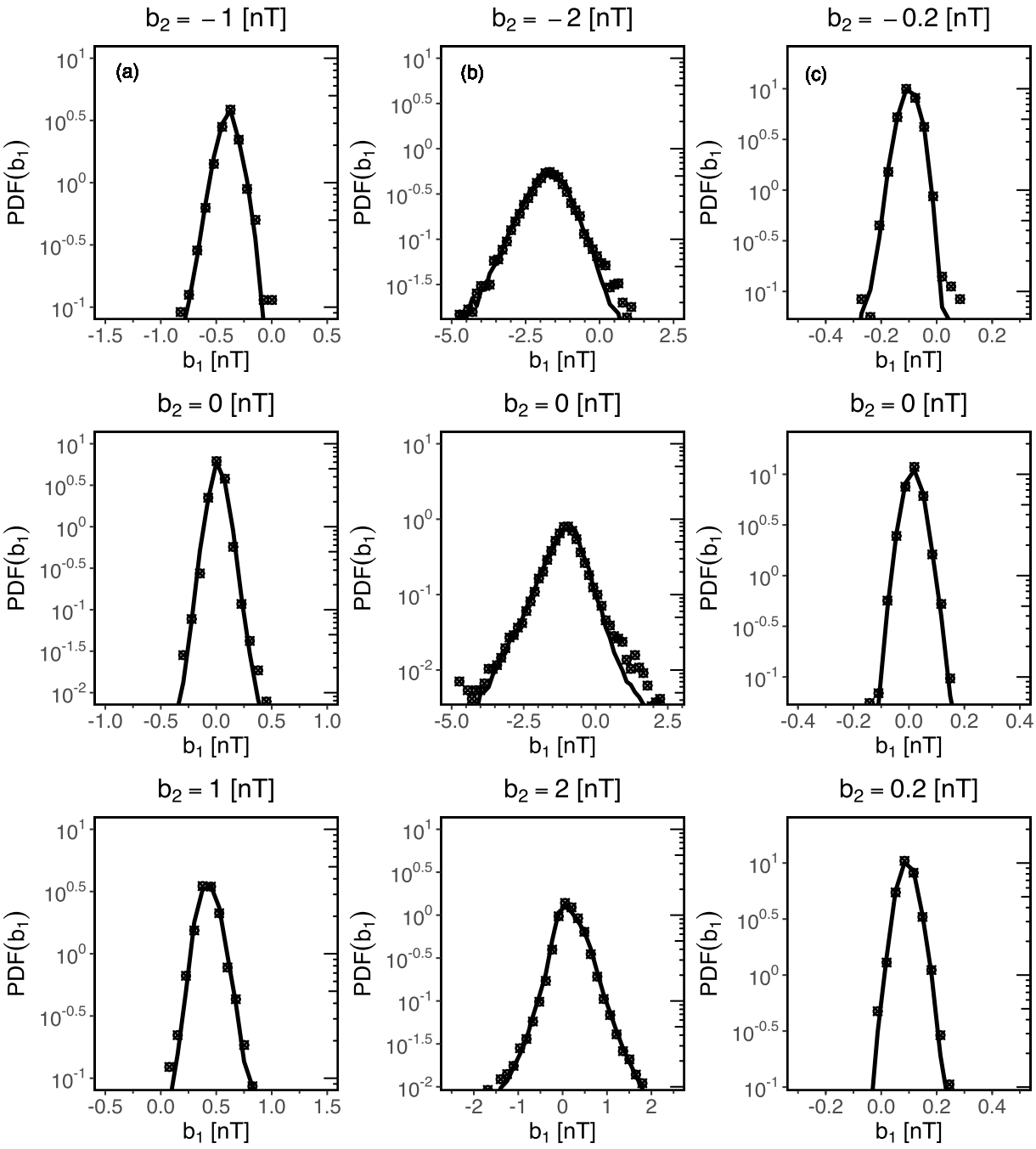

Figure 3. Comparison of cuts through $P(b_1, \tau_1|b_2, \tau_2)$ for the fixed value of the strength of the magnetic field total magnitude $B = |\boldsymbol{B}|$ in the SH: (a) just behind the BS, (b) inside the SH, and (c) near the MP, with increments b_2 with $\tau_1 = 0.02$ s, $\tau^{'} = 0.0278$ s, and $\tau_2 = 0.0356$ s in cases (a) and (c), and with $\tau_1 = 0.2$ s, $\tau^{'} = 0.2625$ s, and $\tau_2 = 0.325$ s in case (b).

exhibit a power-law dependence on temporal scale τ:

$$\begin{cases} a_1(\tau) = A\tau^{\alpha}, \\ a_2(\tau) = B\tau^{\beta}, \\ b_2(\tau) = C\tau^{\gamma}, \end{cases} \tag{14}$$

where the values for all of the logarithmized parameters $A, B, C \in \mathbb{R}$ and the $\alpha, \beta, \gamma \in \mathbb{R}$ are given in Table 1.

It is important to emphasize that the functional dependencies of the coefficients $a_1(\tau)$, $a_2(\tau)$, and $b_2(\tau)$ on τ given by equation (14) are merely parametrizations of the empirical results. In fact, here power laws have been selected, because they have adequately described the observed values with sufficient accuracy. Nevertheless, some alternative theoretical analyses may lead to slightly different functional dependence (see Renner et al. 2001). Admittedly, it turned out that the values of the fitted parameters can slightly be different

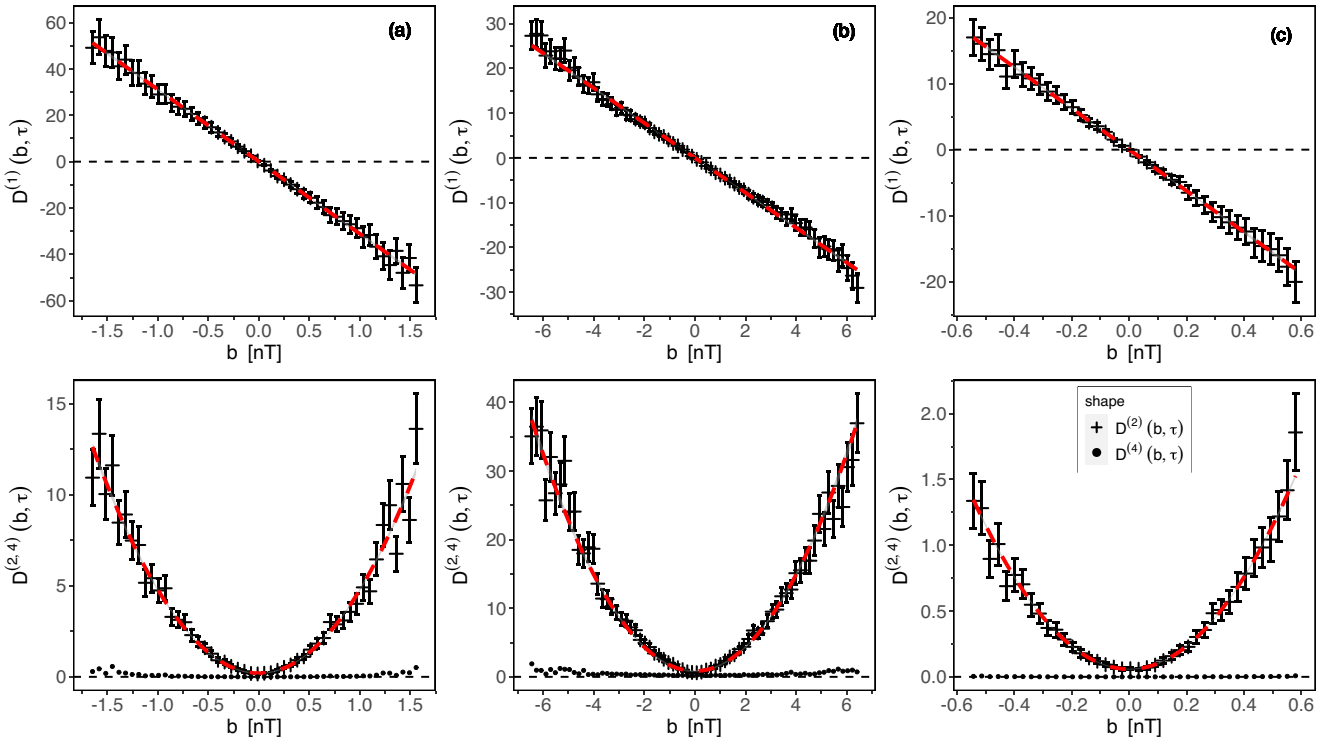

Figure 4. The first and second limited-size Kramers–Moyal (KM) coefficients determined by the magnetic field increments b for a total strength of magnetic field $B = |\boldsymbol{B}|$ in the SH: (a) just behind the BS, (b) inside the SH, and (c) near the MP. The dashed red lines show the best choice fits to the calculated values of $D^{(1)}(b, \tau)$ and $D^{(2)}(b, \tau)$ with $D^{(4)}(b, \tau) = 0$, according to the Pawula's theorem.

Table 1. The fitted parameters for power-law dependence of first- and second-order Kramers–Moyal (KM) coefficients of equations (13) and (14) as functions of scale τ.

Case	$\log_{10}(A)$	α	$\log_{10}(B)$	β	$\log_{10}(C)$	γ
(a)	0.6989 ± 0.0225	-1.1191 ± 0.0089	-0.4946 ± 0.1259	1.1631 ± 0.0498	0.5854 ± 0.0706	-1.7325 ± 0.0279
(b)	0.1837 ± 0.0139	-1.0417 ± 0.0100	-0.4666 ± 0.0160	0.5425 ± 0.0116	0.4183 ± 0.0163	-1.2233 ± 0.0118
(c)	0.7791 ± 0.0079	-1.1055 ± 0.0057	-0.5893 ± 0.0126	1.0002 ± 0.0091	0.5011 ± 0.0274	-1.7646 ± 0.0199

from those that fit exactly the solution of the FP equation (9). Renner et al. (2001) have also highlighted the asymmetry of the fit $D^{(2)}(b, \tau)$ on b, which is also present in our analysis [especially in case (c), and to a lesser degree in case (a)].

The obtained fits to the *MMS* observations in the SH are depicted in Fig. 5, for each case (a), (b), and (c), showing the dependence of KM coefficients parameters on scale $\tau > 0$. Since our data contain a multitude of relatively low values and a few exceedingly large values, which would render a linear graph rather unreadable, instead of using a standard linear graph, we have decided to employ logarithmic scales for both the vertical and horizontal axes (so-called log–log plot). Such a procedure is rather straightforward. For example, for the first row of equation (14), taking the logarithm of both sides one obtains $\log(a_1(\tau)) = \alpha \log(\tau) + \log(A)$, which is a special case of a linear function, with the exponent α corresponding to the slope of the line. The value of $\log(A)$ corresponds to the intercept of a $\log(a_1(\tau))$ axis, while the $\log(\tau)$ axis is intercepted at $\log A/(-\alpha)$. We have opted for this approach to enhance the clarity of the presentation. Therefore, since we have used both the logarithmic scales the respective power laws appear as straight lines in Fig. 5. Similarly, the graphical representations for all the parameters a_1, b_1, and b_2 of equations (13) and (14), which we have provided, are helpful for identifying correlations and determining respective constants A, B, C and $\alpha < 0$, $\beta > 0$, $\gamma < 0$ in Table 1 (cf. Macek et al. 2023).

After performing a careful analysis of the *MMS* magnetic field magnitude B data, our findings indicate that the power-law dependence is applicable for the values of: $\tau \lesssim 100\Delta t_B = 0.78$ s in case (a); $\tau \lesssim 150\Delta t_B = 9.375$ s in case (b); $\tau \lesssim 50\Delta t_B = 0.39$ s in case (c), and for some larger scales, say $\tau \gtrsim \tau_G$, the shapes of the probability density functions appear to be closer to Gaussian. However, despite the satisfactory results obtained at these small kinetic scales, a more intricate functional dependence (possibly polynomial fits) is characteristic for much higher scales, in particular, in the inertial domain (Strumik & Macek 2008a,b).

As a result of our investigations, we are able to obtain analytical stationary solutions $p_s(x)$ given by equation (12) following from the FP equation (9), which can be expressed by a continuous kappa distribution (also known as Pearson's type VII distribution), which exhibits a deviation from the normal Gaussian distribution. The probability density function of this distribution is of a given

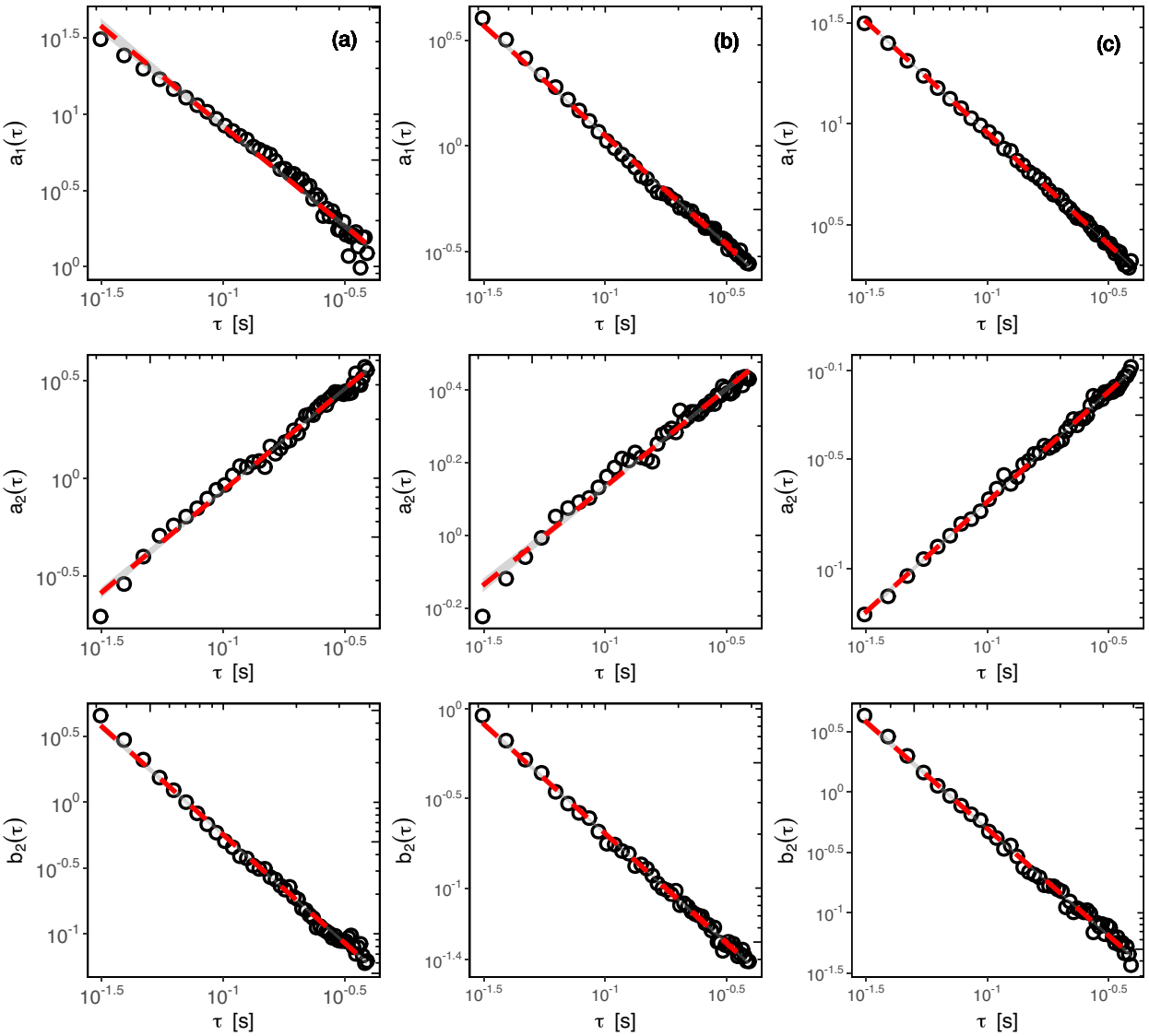

Figure 5. Linear dependence of the parameters a_1, a_2, b_2 (see equation 14) on the double logarithmic scale τ (log–log plot), for the magnetic field overall intensity $B = |\boldsymbol{B}|$ in the SH: (a) just behind the BS, (b) inside the SH, and (c) near the MP. The dashed red lines, with the standard error of the estimate illustrated by grey shade, show the best choice fits to the calculated values.

form

$$p_{\rm s}(b) = \frac{N_0}{\left[1 + \frac{1}{\kappa}\left(\frac{b}{b_0}\right)^2\right]^{\kappa}}, \tag{15}$$

where, for $a_2(\tau) \neq 0, b_0(\tau) \neq 0$, we have a shape parameter $\kappa = 1 + a_1(\tau)/[2b_2(\tau)]$ and $b_0^2 = a_2(\tau)/[b_2(\tau) + a_1(\tau)/2]$, while $N_0 = p_{\rm s}(0)$ satisfies the normalization $\int_{-\infty}^{\infty} p_{\rm s}(b)\,{\rm d}b = 1$. By substituting $p_{\rm s}(b)$ to this integral we find that

$$N_0 = \frac{\Gamma(\kappa)}{\Gamma\left(\kappa - \frac{1}{2}\right) b_0\sqrt{\pi\kappa}}, \tag{16}$$

where, this time, $\Gamma(\kappa) = \int_0^{\infty} b^{\kappa-1}\,{\rm e}^{-b}\,{\rm d}b$, ${\rm Re}(\kappa) > 0$ is a mathematical gamma function (Euler integral of the second kind), as defined for all complex numbers with a positive real part.

It is worth noting that kappa distribution, as represented by equation (15), approaches the normal Gaussian (Maxwellian) distribution for large values of scaling parameter κ. To be precise, as $\kappa \to \infty$, the following well-known formula can approximately be satisfied:

$$\lim_{\kappa\to\infty} p_{\rm s}(b) = N_0 \exp\left(-\frac{b^2}{2\sigma^2}\right), \tag{17}$$

with the scaling parameter b_0 related to the standard deviation $\sigma = b_0/\sqrt{2}$. This time the parameter $N_0 = p_{\rm s}(0)$ satisfies the elementary normalization $N_0 = \frac{1}{\sigma\sqrt{2\pi}}$.

The numerical results of fitting the empirical *MMS* data to the given distributions and determining the relevant parameters of equation (15) are as follows: $\kappa = 1.5179$, $b_0 = 1.9745$, and $N_0 = 0.68438$ for B in case (a); $\kappa = 1.3758$, $b_0 = 2.6955$, and $N_0 = 0.34375$ in case (b); and $\kappa = 3.5215$, $b_0 = 1.7313$, and $N_0 = 1.1866$ in case (c). These values of κ would correspond to the non-extensivity parameter of the generalized (Tsallis) entropy $q = 1 - 1/\kappa$ (e.g. Burlaga & Viñas 2005). In our case this is given by $q = \frac{a_1(\tau)}{a_1(\tau)+2b_2(\tau)}$ and is equal to 0.341 in case (a), 0.273 in case (b), and 0.716 in case (c). The extracted values of the κ and q parameters provide robust measures of the departure of the system from equilibrium. We see that these

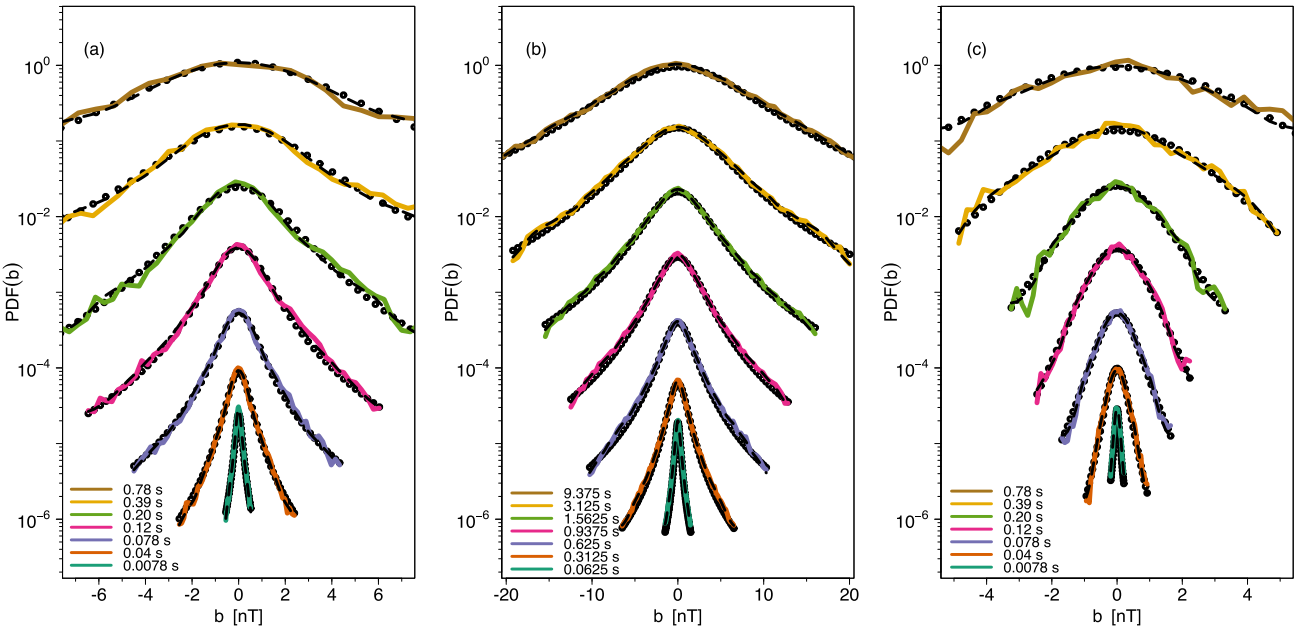

Figure 6. The empirical probability density functions (various continuous coloured lines) for a total strength of magnetic field $B = |\boldsymbol{B}|$, which correspond to spectra in Fig. 1, compared with the non-stationary (dashed lines) and the stationary (open circles) solutions of the FP equation, for various time-scales (shifted from bottom to top) $\tau = 0.0078$, 0.04, 0.078, 0.12, 0.2, 0.39, and 0.78 s in cases (a) and (c), and $\tau = 0.0625$, 0.3125, 0.625, 0.9375, 1.5625, 3.125, and 9.375 s in case (b).

values are similar to $q \sim 0.5$ for $\kappa \sim 2$ reported for the *Parker Solar Probe* (*PSP*) data by Benella et al. (2022).

Now, by using the system of equation (13) with equation (9), we have arrived at the following formula (Macek et al. 2023):

$$\big(a_2(\tau) + b_2(\tau)b^2\big)\frac{\partial^2 P(b,\tau)}{\partial b^2} + \big(a_1(\tau) + 4b_2(\tau)\big)b\frac{\partial P(b,\tau)}{\partial b} + \frac{\partial P(b,\tau)}{\partial \tau} + \big(a_1(\tau) + 2b_2(\tau)\big)P(b,\tau) = 0. \tag{18}$$

This implies that the FP equations (11) and (18) are expressed in terms of a second-order parabolic partial differential equation. Thus, through the implementation of the numerical Euler integration scheme, which has been verified for stationary solution $\frac{\partial P(b,\tau)}{\partial \tau} = 0$, we are able to successfully solve the non-stationary FP equation numerically. Our results are in line with those obtained by Rinn et al. (2016) using the statistical modelling package in programming language R.

Fig. 6 shows the findings resulting from our analysis based on the *MMS* data. Here we compare the solutions of the FP equation (9) with the empirical probability density functions of $P(b, \tau)$: (a) near the BS; (b) inside the SH; and (c) near the MP for various scales τ (not greater than τ_G). The displayed plotted curves, in each case, are as follows: the stationary solution (denoted by open circles); the non-stationary solutions (marked with dashed lines); and the empirical PDFs (indicated with various coloured continuous lines).

Further, in cases (a) and (c) the corresponding time scales are $\tau =$ 0.0078, 0.04, 0.078, 0.12, 0.2, 0.39, and 0.78 s, whereas in case (b) these scales are $\tau = 0.0625$, 0.3125, 0.625, 0.9375, 1.5625, 3.125, and 9.375 s. The corresponding curves are shifted in the vertical direction from bottom to top for even better clarity of presentation. It is also worth noting that we have used the semi-logarithmic scale τ, what is useful when dealing with data that covers a broad range of values. On this scale, the vertical scale is logarithmic (base 10) axis, which means that the separation between the ticks on the graph is proportional to the logarithm of PDF, while the horizontal b-axis is a standard linear scale, and the ticks are evenly spaced.

What is important to note from this picture are the peaked leptokurtic shapes of PDFs and corresponding stationary solutions. Namely, in case (a) the peak (with large kurtosis) is present for scales up to ~0.5 s; in case (b) up to about ~3 s; and in case (c) up to ~0.25 s. For these levels selected for each case the PDF becomes closer to Gaussian (i.e. approximately parabolic shape on the graph with the semi-logarithmic scales), as expected for large values of κ. In case (c) we can see more jumps in fluctuations, i.e. the curves are not so smooth. Fluctuations are quite evident in both the empirical curves and the theoretical solutions, so it seems that some numerical noise is present in the tails of the PDFs. Admittedly, reducing noise is a tricky issue, although the easiest way is to artificially smooth using the simple moving average. Therefore, we have tried this procedure for $n = 1$, 2, 3 steps and it has appeared that the $n = 3$ choice is sufficient.

Fig. 7 depicts finally the probability density functions of fluctuations of the strength of the magnetic field b_τ rescaled by the standard deviations $\sigma(b_\tau)$ in the following way:

$$b_\tau \longrightarrow \frac{b_\tau}{\sigma(b_\tau)}, \tag{19}$$

$$\mathrm{PDF}(b_\tau) \longrightarrow \sigma(b_\tau)\,\mathrm{PDF}(b_\tau). \tag{20}$$

In this way, we can define a master curve for the shape of the PDFs. Again, we have used the logarithmic scale on the vertical axis. We also see that the rescaled curves are consistent with the stationary solutions of equation (15), as marked with open circles in Fig. 6. It should be noted that all the curves in Fig. 7 are very close to each other for small scales. However, for larger $\tau = 50$ or $100\Delta t_B$ these shapes deviate from the master curve and naturally tend to the well-known Gaussian shape. We see that the shape of the

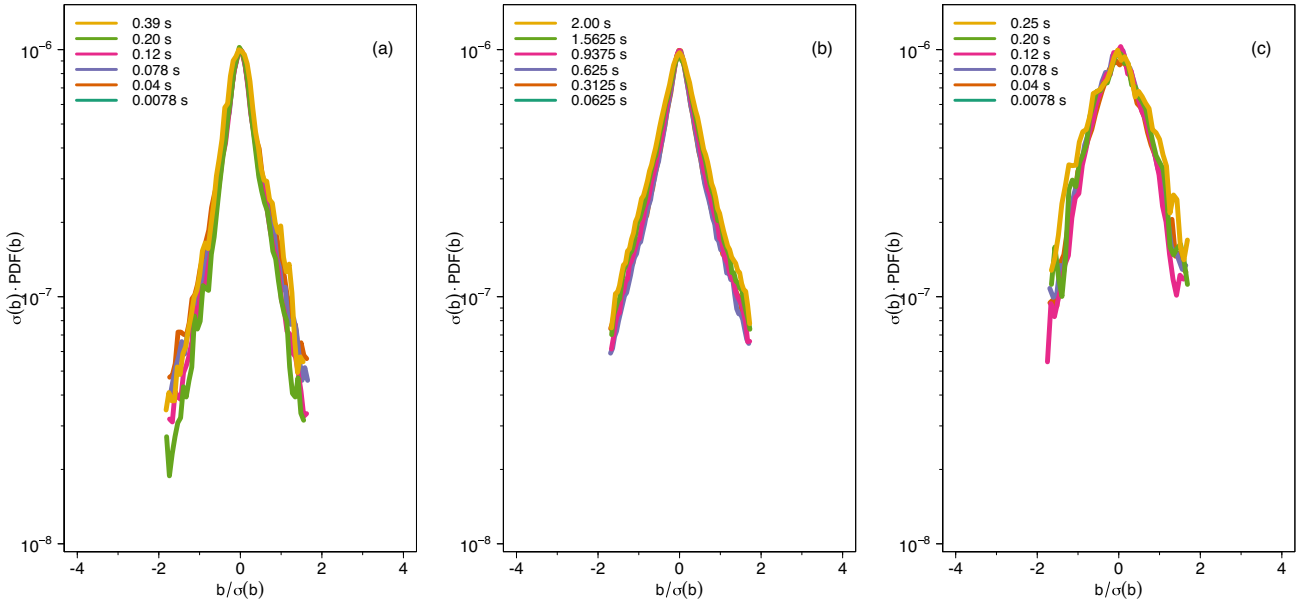

Figure 7. A collapse of probability density functions of b_τ (compare Fig. 6), which are scaled by the corresponding standard deviations (see equations 19 and 20), for the small time-scales τ stopping at approximately: $\tau \sim 0.4$ s in case (a); $\tau \sim 2.0$ s in case (b); and $\tau \sim 0.25$ s in case (c).

PDFs obtained from the *MMS* data exhibits a global *scale invariance* in the SH up to scales of ∼2 s. A similar collapse has also been reported with the *PSP* data at subproton scales (Benella et al. 2022). Fig. 7 shows that fluctuations in the SH are described by a stochastic process. Admittedly, the mechanism of generation of these magnetic fluctuation at small kinetic scale is not known, but the results suggest some universal characteristics of the processes. An alternative point of view has recently been proposed by Carbone et al. (2022).

5 CONCLUSIONS

Following our studies in the space plasmas at large inertial scales (Strumik & Macek 2008a,b), we have examined time series of the strength of magnetic fields in different regions of the Earth's SH, where the spectrum steepens at subproton scales (Macek et al. 2018). With the highest resolution available on the *MMS*, the data samples just after the BS and near the MP are stationary and for somewhat lower resolution deep inside the SH the deviations from stationarity are small and could well be eliminated. Basically, in all these cases the stochastic fluctuations exhibit Markovian features. We have verified that the necessary CK condition is well satisfied, and the probability density functions are consistent with the solutions of this condition.

In addition, the Pawula's theorem is also well satisfied resulting in the FP equation reduced to drift and diffusion terms. Hence, this corresponds to the generalization of Ornstein–Uhlenbeck process. Further, the lowest KM coefficients have linear and quadratic dependence as functions of the magnetic field increments. In this way, the power-law distributions are well recovered throughout the entire SH. For some moderate scales we have the kappa distributions described by various peaked shapes with heavy tails. In particular, for large values of the kappa parameter these distributions are reduced to the normal Gaussian distribution.

Similarly as for the *PSP* data, the probability density functions of the magnetic fields measured onboard the *MMS* rescaled by the respective standard deviations exhibit a universal global *scale invariance* on kinetic scales, which is consistent with the stationary solution of the FP equation. We hope that all these results, especially those reported at small scales, are important for a better understanding of the physical mechanism governing turbulent systems in space and laboratory.

ACKNOWLEDGEMENTS

We thank Marek Strumik for discussion on the theory of Markov processes. We are grateful for the efforts of the entire *MMS* mission, including development, science operations, and the Science Data Center at the University of Colorado. We benefited from the efforts of T. E. Moore as Project Scientist, C. T. Russell, and the magnetometer team. We acknowledge B. L. Giles, Project Scientist, for information about the magnetic field instrument, and also D. G. Sibeck and M. V. D. Silveira for discussions during previous visits by WMM to the NASA Goddard Space Flight Center.

This work has been supported by the National Science Centre, Poland (NCN) through grant no. 2021/41/B/ST10/00823.

DATA AVAILABILITY

The data supporting the results in this paper are available through the *MMS* Science Data Center at the Laboratory for Atmospheric and Space Physics (LASP), University of Colorado, Boulder: https://lasp.colorado.edu/mms/sdc/public/. The magnetic field data from the magnetometer are available online from http://cdaweb.gsfc.nasa.gov. The data have been processed using the statistical programming language R.

REFERENCES

Akaike H., 1973, in Petrov B. N., Csaki F., eds, Proceedings of the 2nd International Symposium on Information Theory. Akademiai Kiado, Budapest, p. 267

Benella S., Stumpo M., Consolini G., Alberti T., Carbone V., Laurenza M., 2022, ApJ, 928, L21

Biskamp D., 2003, Magnetohydrodynamic Turbulence. Cambridge Univ. Press, Cambridge

Bruno R., Carbone V., 2016, Lecture Notes in Physics Vol. 928, Turbulence in the Solar Wind. Springer, Cham, Switzerland
Bruno R., Trenchi L., Telloni D., 2014, ApJ, 793, L15
Burch J. L., Moore T. E., Torbert R. B., Giles B. L., 2016, Space Sci. Rev., 199, 5
Burlaga L. F., 1995, Interplanetary Magnetohydrodynamics. Oxford Univ. Press, New York
Burlaga L. F., Viñas A. F., 2005, Phys. A: Stat. Mech. Applications, 356, 375
Carbone V., Telloni D., Lepreti F., Vecchio A., 2022, ApJ, 924, L26
Dickey D. A., Fuller W. A., 1979, J. Am. Stat. Assoc., 74, 427
Frisch U., 1995, Turbulence. The legacy of A. N. Kolmogorov. Cambridge Univ. Press, Cambridge
Itô K., 1944, Proc. Imperial Acad., 20, 519
Karimabadi H. et al., 2014, Phys. Plasmas, 21, 062308
Kolmogorov A., 1941, Doklady Akad. Nauk SSSR, 30, 301
Kraichnan R. H., 1965, Phys. Fluids, 8, 1385
Lion S., Alexandrova O., Zaslavsky A., 2016, ApJ, 824, 47
Macek W. M., 1998, Phys. D: Nonlinear Phenomena, 122, 254
Macek W. M., Krasińska A., Silveira M. V. D., Sibeck D. G., Wawrzaszek A., Burch J. L., Russell C. T., 2018, ApJ, 864, L29
Macek W. M., Silveira M. V. D., Sibeck D. G., Giles B. L., Burch J. L., 2019a, Geophys. Res. Lett., 46, 10295
Macek W. M., Silveira M. V. D., Sibeck D. G., Giles B. L., Burch J. L., 2019b, ApJ, 885, L26
Macek W. M., Wójcik D., Burch J. L., 2023, ApJ, 943, 152
Pedrizzetti G., Novikov E. A., 1994, J. Fluid Mech., 280, 69
Perrone D., Alexandrova O., Mangeney A., Maksimovic M., Lacombe C., Rakoto V., Kasper J. C., Jovanovic D., 2016, ApJ, 826, 196
Perrone D., Alexandrova O., Roberts O. W., Lion S., Lacombe C., Walsh A., Maksimovic M., Zouganelis I., 2017, ApJ, 849, 49
Renner C., Peinke J., Friedrich R., 2001, J. Fluid Mech., 433, 383
Rinn P., Lind P., Wächter M., Peinke J., 2016, J. Open Res. Softw., 4, e34
Risken H., 1996, The Fokker–Planck Equation: Methods of Solution and Applications. Springer, Berlin
Roberts O. W., Li X., Alexandrova O., Li B., 2016, J. Geophys. Res., 121, 3870
Sahraoui F., Goldstein M. L., Robert P., Khotyaintsev Y. V., 2009, Phys. Rev. Lett., 102, 231102
Schekochihin A. A., Cowley S. C., Dorland W., Hammett G. W., Howes G. G., Quataert E., Tatsuno T., 2009, ApJS, 182, 310
Schwarz G., 1978, Ann. Stat., 6, 461
Stratonovich R. L., 1968, Conditional Markov Processes and Their Application to the Theory of Optimal Control. American Elsevier Publishing Company, Princeton, NJ, available at: https://api.semanticscholar.org/CorpusID:117417954
Strumik M., Macek W. M., 2008a, Phys. Rev. E, 78, 026414
Strumik M., Macek W. M., 2008b, Nonlinear Processes Geophys., 15, 607
Taylor G. I., 1938, Proc. R. Soc. Lond. Ser. A, 164, 476
Treumann R. A., 2009, A&AR, 17, 409
Welch P. D., 1967, IEEE Trans. Audio Electroacoustics Control, 15, 70

This paper has been typeset from a TEX/LATEX file prepared by the author.

Testing for Markovian character of transfer of fluctuations in solar wind turbulence on kinetic scales

Dariusz Wójcik [*] and Wiesław M. Macek [†]
Institute of Physical Sciences, Faculty of Mathematics and Natural Sciences, Cardinal Stefan Wyszyński University, Wóycickiego 1/3, 01-938 Warsaw, Poland and Space Research Centre, Polish Academy of Sciences, Bartycka 18A, 00-716 Warsaw, Poland

(Received 9 March 2024; revised 13 May 2024; accepted 28 June 2024; published 12 August 2024)

We apply statistical analysis to search for processes responsible for turbulence in physical systems. In our previous studies, we have shown that solar wind turbulence in the inertial range of large magnetohydrodynamic scales exhibits Markov properties. We have recently extended this approach on much smaller kinetic scales. Here we are testing for the Markovian character of stochastic processes in a kinetic regime based on magnetic field and velocity fluctuations in the solar wind, measured onboard the Magnetospheric Multiscale (MMS) mission: behind the bow shock, inside the magnetosheath, and near the magnetopause. We have verified that the Chapman-Kolmogorov necessary conditions for Markov processes is satisfied for *local* transfer of energy between the magnetic and velocity fields also on kinetic scales. We have confirmed that for magnetic fluctuations, the first Kramers-Moyal coefficient is linear, while the second term is quadratic, corresponding to drift and diffusion processes in the resulting Fokker-Planck equation. It means that magnetic self-similar turbulence is described by generalized Ornstein-Uhlenbeck processes. We show that for the magnetic case, the Fokker-Planck equation leads to the probability density functions of the kappa distributions, which exhibit global universal *scale invariance* with a linear scaling and lack of intermittency. On the contrary, for velocity fluctuations, higher order Kramers-Moyal coefficients should be taken into account and hence scale invariance is not observed. However, the nonextensity parameter in Tsallis entropy provides a robust measure of the departure of the system from equilibrium. The obtained results are important for a better understanding of the physical mechanism governing turbulent systems in space and laboratory.

DOI: 10.1103/PhysRevE.110.025203

I. INTRODUCTION

Turbulence consists of phenomena that, notwithstanding progress in numerical simulations, remain a challenge for natural sciences, even for simple fluids [1]. This is all the more so for magnetized plasma with magnetohydrodynamic (including Hall) simulations, but physical mechanisms responsible for irregular behavior are still not transparent [2]. Fortunately, collisionless solar wind plasma can be considered a natural laboratory for investigating these complex dynamical systems [3]. In particular, fluctuations of magnetic fields play an important role in space plasmas [e.g., 4,5]. The classical spectrum of Kolmogorov [6] follows a power law with slope exponent $-5/3$ for isotropic incompressible turbulence in ordinary fluids and Kraichnan [7] type spectrum with an even smaller slope of $-3/2$ in magnetized media.

One should underline that in a Markov process, given an initial probability distribution function (PDF), the transition to the next stage can be fully determined. It is also interesting that one can prove and demonstrate the existence of such Markov processes based on experimental data [8]. Namely, without relying on any assumptions or models for the underlying stochastic process, we are able to extract the equation of Markov process directly from the measurements of times series. Hence this Markov approach appears to be a bridge between the statistical and dynamical analysis of complex physical systems. There is a substantial evidence based on statistical analysis that turbulence exhibits Markov properties [8–13]. We have already proved that magnetic and velocity fluctuations have Markovian features in the inertial range of hydromagnetic scales [10,11]. In this case, the characteristic spectrum appears to be roughly close to the standard Kolmogorov [6] power-law type with exponent $-5/3 \approx -1.67$; see Fig. 1 of Ref. [10].

On the other hand, the presence of the classical $-5/3$ or $-3/2$ at small scales seems to be rather exceptional. In fact, based on the highest millisecond time resolution data available in the Magnetospheric Multiscale (MMS) mission, we have noted clear breakpoints in the magnetic energy spectra in various regions of the Earth's magnetosheath: (a) behind the bow shock (BS), (b) inside the magnetosheath (SH), and (c) near the magnetopause (MP) before leaving the magnetosheath. Namely, we have observed that the magnetic spectrum steepens at some critical points in the kinetic regime of scales: from $-5/2$ above the ion gyrofrequency till $-7/2$ or even $-11/2$

[*]Contact author: dwojcik@cbk.waw.pl
[†]Contact author: macek@uksw.edu.pl, macek@cbk.waw.pl; http://www.cbk.waw.pl/~macek

(or $-16/3$) above the Taylor-shifted frequency (related to the electron skin depth of above 20–25 Hz), but for velocity spectrum similar to Kolmogorov [6]; see Ref. [14]. Some higher slopes for the magnetic spectrum have also been observed for an electron gyroscale [15] and for whistler turbulence [e.g., 16,17].

Therefore, it is certainly interesting to investigate the Markov property of turbulence outside the inertial region of magnetized plasma on small scales, when the slopes are consistent with kinetic theory [e.g., 18]. It should also be noted that based on the measurements of magnetic field fluctuations in the Earth's magnetosheath gathered onboard the MMS mission, we have recently extended this statistical analysis to much smaller scales, where kinetic theory should be applied [19,20]. Therefore, here we compare the characteristics of both magnetic field and velocity fluctuations behind the bow shock, inside the magnetosheath, and near the magnetopause. In this paper, we present the results of our comparative analysis for the following cases of transfer of fluctuations: velocity-to-velocity, velocity-to-magnetic, and magnetic-to-velocity, confirming the local character of the transfer of cascading eddies. We also check whether the Fokker-Planck (FP) equation is suitable for the processes responsible for solar wind turbulence and whether their solutions agree with experimental PDFs in selected regions of the magnetosheath.

Section II provides a brief description of the MMS mission and the analyzed data. Section III outlines mathematical stochastic and statistical methods for processes in scale (Sec. III A), including the necessary Chapman-Kolmogorov (CK) condition in Sec. III B. This enables estimating the Kramers-Moyal (KM) coefficients and checking the validity of Pawula's theorem leading to the FP equation in Sec. III C, given the stationarity (Appendix A) of the detrended time series (Appendix B). The results of our analysis are presented in Sec. IV, which demonstrates that at least for magnetic fluctuations, the solutions of the FP equation are in good agreement with empirical PDFs also on small kinetic scales, with a universal global *scale invariance*. Finally, Sec. V emphasizes the significance of stochastic processes in relation to turbulence in space plasmas, which exhibit Markovian features across the kinetic domain.

II. DATA

The MMS mission was launched in 2015 to investigate plasma processes in the magnetosphere and the solar wind plasma especially on small scales [21]. Our recent analysis has encompassed increments in each vector component of the magnetic field, denoted as $\mathbf{B} = (B_x, B_y, B_z)$, within the Geocentric Solar Ecliptic (GSE) coordinate system, as displayed together with the corresponding spectra in Fig. 1 of Ref. [19]. This vector field **B** have been derived from measurements collected by the MMS 1 spacecraft, positioned just beyond the bow shock region of the Earth. We have successfully demonstrated the presence of Markovian characteristics, where the magnetic turbulence occurs, even at significantly reduced kinetic scales. Interestingly, our observations also reveal a remarkable uniformity in these Markovian features across all components. We have also explored analogous characteristics of the magnitude of this vector field, $B = |\boldsymbol{B}|$, in three different regions within the magnetosphere: (a) behind the bow shock, (b) within the magnetosheath, and (c) in proximity to the magnetopause, as depicted in Fig. 1 of Ref. [20].

Consequently, we now aim to analyze the magnetic field strength $B = |\mathbf{B}|$, as well as the ion plasma velocity $V = |\mathbf{V}|$ magnitudes inside the magnetosheath and in its close vicinity. These regions as well as the spacecraft trajectory have been depicted in Fig. 1 of Ref. [14]. To explore the potential global scale invariance of the fluctuations, we have opted for the same three time interval samples as those presented in Table 1 of Ref. [14]. For a magnetic field, in cases (a) near the bow shock and (c) near the magnetopause, with time spans of approximately 5 min and 1.8 min each, we have used BURST-type observations obtained from the FluxGate Magnetometer (FGM) sensor. This sensor has the highest resolution of $\Delta t_B = 7.8$ ms (roughly 128 samples per second), providing data sets with 37 856 and 13 959 data points, respectively. Conversely, in case (b) between the bow shock and the magnetopause, we have the available FAST-survey type data at substantially lower resolution of $\Delta t_B = 62.5$ ms (16 samples per second). This data set consists of a much longer interval, spanning 3.5 h, and contains a total of 198 717 data points.

In addition, in the analysis of ion plasma velocity magnitude $V = |\mathbf{V}|$, we use data obtained through measurements from the Dual Ions Spectrometer (DIS) instrument. These measurements have a lower time resolution; specifically within the BURST-type observations, the time resolution Δt_V for ion measurements is set at 150 ms (about 6.5 samples per second), and 30 ms (33 samples per second) for electrons. In the FAST-survey mode, the instrument provides data snapshots at regular intervals of $\Delta t_V = 4.5$ s. All the data sets considered in this study are available through Ref. [22], while the complete description of the MMS spacecraft instruments is specified in Ref. [21].

III. METHODS OF DATA ANALYSIS

As usual, the examination of statistical properties of a turbulent system is performed across various scales. Kolmogorov [6] has already postulated that the isotropic turbulence within the inertial range should be linked to the flow velocity increment of τ. We also suppose that fluctuations occurring at a larger scale τ shift to smaller and smaller scales, until the dissipation scale is reached [19,20]. Therefore, here we employ the increments (fluctuations) of a given parameter, either the characteristic magnetic field denoted by $X := B = |\mathbf{B}|$ or the ion velocity denoted by $X := V = |\boldsymbol{V}|$. Naturally, such increments are typical scale-dependent complexity measures, which characterize the behavior of a turbulent system at a given time t and at each timescale (lag) τ, as given by

$$x_\tau(t) := \delta x(t, \tau) = X(t + \tau) - X(t), \tag{1}$$

i.e., the difference in magnetic field or flow velocity between points separated by a time interval τ.

In consequence, stochastic fluctuations can be perceived as a stochastic process, governed by the N-point joint (transition) conditional probability density function (denoted as cPDF), $P(x_1, \tau_1|x_2, \tau_2; \ldots; x_N, \tau_N)$, where $P(x_i, \tau_i|x_j, \tau_j) =$

$\frac{P(x_i,\tau_i;x_j,\tau_j)}{P(x_j,\tau_j)}$ is a conditional PDF, with the joint PDF $P(x_i, \tau_i; x_j, \tau_j)$ and a marginal PDF $P(x_j, \tau_j)$. By employing these joint PDFs, the correlations between scales can also be determined, which illustrates how the complexity is linked across different scales. Nevertheless, the reasoning can easily be inverted by applying the *Bayes theorem* by the equation, for $P(x_j, \tau_j) \neq 0$,

$$P(x_i, \tau_i|x_j, \tau_j) = \frac{P(x_j, \tau_j|x_i, \tau_i)P(x_i, \tau_i)}{P(x_j, \tau_j)}. \tag{2}$$

When τ is scaled by a factor $\lambda \in \mathbb{R}^+$, then it is said that the increments are globally scale invariant, if scaling occurs with the unique scaling exponent β, i.e., $x_{\lambda\tau}(t) = \lambda^\beta x_\tau(t)$, with β independent of scale τ.

A. Process in scale

The power spectral densities (PSDs) (as shown in the lower parts of Figs. 2–4 in Ref. [14]) serve as a statistic to scrutinize the scale-dependent behavior of turbulent fluctuations and are analogous to the examination of the autocorrelation function. In this study, we explore a somewhat expanded application of stochastic processes by means of the Markovian approach. Essentially, the stochastic process is said to be *Markovian* if, for $0 < \tau_1 < \tau_2 < \cdots < \tau_N$, it holds that

$$P(x_1, \tau_1|x_2, \tau_2) = P(x_1, \tau_1|x_2, \tau_2; \ldots; x_N, \tau_N). \tag{3}$$

In particular, if the data satisfy the Markov condition from larger to smaller scales, this condition is also satisfied in the reverse direction from smaller to larger scales, as stated previously by the Bayes theorem in Eq. (2); see Ref. [8].

B. Chapman-Kolmogorov condition and locality

The generalization of Eq. (3) is called the *Chapman-Kolmogorov* (CK) *equation* (condition),

$$P(x_1, \tau_1|x_2, \tau_2) = \int_{-\infty}^{+\infty} P(x_1, \tau_1|x', \tau')P(x', \tau'|x_2, \tau_2)dx', \tag{4}$$

where (τ_1, τ', τ_2) is a set of timescale parameters, such as $\tau_1 < \tau' < \tau_2$. We have checked that it is satisfied for the Markov turbulence on inertial scales [10]. Importantly, this serves as the very essential requirement for a stochastic process to exhibit Markovian properties.

If the condition of Eq. (4) is fulfilled, then the transition PDF from the scale τ_2 to τ_1 can be decomposed into two sequential transitions: first from τ_2 to τ', and next from τ' to τ_1. Hence, in the context of a turbulent cascade, fulfillment of this condition for all considered (τ_1, τ', τ_2) implies the existence of a *local* transfer mechanism in the cascade. When considering fluctuations in time, one can imply that the transfer process is local in scale. Nonetheless, if the root mean square (RMS) (in a discrete case, $x_{\mathrm{RMS}} = [\frac{1}{n}\sum_i x_i^2]^{1/2}$) of ion velocity increments is considerably smaller than the mean velocity $\langle v_{\mathrm{sw}}\rangle$ of the solar wind flow, under Taylor's hypothesis [23], then temporal variations at a fixed position are understood as spatial variations. In this scenario, the local transfer in scale can be understood as being directly linked to the local transfer in wave-vector space.

We also aim to examine the interactions between ion velocity and magnetic field modes, which provide input into the transfer of energy between these two quantities. These interactions should be interpreted as a statistical dependence between $b_\tau(t, \tau)$ and $v_\tau(t, \tau)$. To incorporate this transfer of fluctuations between different quantities, we introduce the generalized CK condition as

$$\begin{aligned} P(x_1, \tau_1|y_2, \tau_2) &= \int_{-\infty}^{+\infty} P(x_1, \tau_1|y', \tau')P(y', \tau'|y_2, \tau_2)dy' \\ &\sim \int_{-\infty}^{+\infty} P(x_1, \tau_1|x', \tau')P(x', \tau'|y_2, \tau_2)dx', \end{aligned} \tag{5}$$

where the intermediate-scale quantity varies, but yields very similar results, allowing for the use of only one version of Eq. (5). This also enables us to investigate whether the transfer of fluctuations between two quantities exhibits a local or nonlocal character. Specifically, if the empirical cPDFs align with those calculated from Eq. (5), then the transfer of fluctuations can be broken down into smaller steps (with the intermediate-scale τ'), implying that the transfer in the cascade has a local character.

Consequently, the differential form of the CK equation (4) is called the *Kramers-Moyal* (KM) expansion and is given by

$$\begin{aligned} -\frac{\partial P(x_\tau, \tau|x'_\tau, \tau')}{\partial\tau} &= \sum_{k=1}^{\infty}\left(-\frac{\partial}{\partial x_\tau}\right)^k \\ &\quad\times [D^{(k)}(x_\tau, \tau)P(x_\tau, \tau|x'_\tau, \tau')], \end{aligned} \tag{6}$$

where the coefficients $D^{(k)}(x_\tau, \tau)$, called Kramers-Moyal (KM) coefficients, are given by

$$D^{(k)}(x_\tau, \tau) = \frac{1}{k!}\lim_{\tau\to\tau'}\frac{1}{\tau - \tau'}M^{(k)}(x_\tau, \tau, \tau'), \tag{7}$$

with

$$M^{(k)}(x_\tau, \tau, \tau') = \int_{-\infty}^{+\infty}(x'_\tau - x_\tau)^k P(x'_\tau, \tau'|x_\tau, \tau)dx'_\tau, \tag{8}$$

which can be obtained by extrapolation (piecewise linear regression model). Equations (7) and (8) show that the drift and diffusion coefficients can be expressed in the form of the first and second moments of the cPDFs $P(x'_\tau, \tau'|x_\tau, \tau)$ in the small time interval limit. In this way, one can find the KM coefficients for the increments x_τ.

In general, the KM expansion (6) involves infinitely many evolution terms. Often the first- and second-order KM coefficients are different from zero, and hence statistically significant, while the third-, fourth-, and higher-order coefficients usually exhibit a tendency to gradually approach zero. The important *Pawula's* theorem [24] states that if the fourth-order KM coefficient is equal to zero, then $D^{(k)}(x_\tau, \tau) = 0$ for $k \geqslant 3$, and the series is limited to the second order.

C. Fokker-Planck and Langevin equations

In this case, the differential KM expansion (6) is presented in a reduced form called the *Fokker-Planck* (FP) equation,

determining the evolution of the transition probability [24]:

$$-\frac{\partial P(x_\tau,\tau|x'_\tau,\tau')}{\partial\tau}=\left[-\frac{\partial}{\partial x_\tau}D^{(1)}(x_\tau,\tau)+\frac{\partial^2}{\partial x_\tau^2}D^{(2)}(x_\tau,\tau)\right]\times P(x_\tau,\tau|x'_\tau,\tau'), \tag{9}$$

where the first and second terms are responsible for the *drift* and *diffusion* processes, respectively. One should note the negative sign which arises from the direction of time evolution, moving from larger to smaller scales, as we have previously assumed.

Consequently, a complementary approach with the following *Langevin* equation (using the *Itô's* definition) emerges:

$$-\frac{\partial x_\tau}{\partial\tau}=D^{(1)}(x_\tau,\tau)+\sqrt{D^{(2)}(x_\tau,\tau)}\,\Gamma(\tau), \tag{10}$$

for the δ-correlated Gaussian white noise $\Gamma(\tau)$, which satisfies the following normalization conditions: mean $\langle\Gamma(\tau)\rangle=0$ and a correlation $\langle\Gamma(\tau)\Gamma(\tau')\rangle=2\delta(\tau-\tau')$, where δ is a Dirac delta function [13]. The stochastic nature of the fluctuations across different scales is encapsulated by the diffusion coefficient within the Langevin framework.

Equivalently, Langevin equation (10) can be rewritten in a more natural form of stochastic differential equation (SDE),

$$dx_\tau(\tau)=h(x_\tau,\tau)d\tau+g(x_\tau,\tau)dW(\tau), \tag{11}$$

where, again, $h(x_\tau,\tau)=D^{(1)}(x_\tau,\tau)$ is a drift term and $g(x_\tau,\tau)=\sqrt{D^{(2)}(x_\tau,\tau)}$ modulates a diffusion term. Here, $\{W(\tau)\,|\,\tau\geqslant 0\}$ is a scale-related Wiener process (Brownian motion). Generally, we say that $\{W(\tau)\}$ is a Brownian motion in scale if the following conditions are satisfied: (i) $W(\tau=0)=0$, (ii) mean $<W(\tau)>\;=0$ and variance $\mathrm{Var}[W(\tau)]=\sigma^2\tau$, and (iii) $\{W(\tau)\}$ has stationary and independent increments. Note that the Markov property is implied by the presence of independent increments. There is an equivalence between the FP and Langevin dynamics, in a way that the PDF of a stochastic process whose dynamics is governed by the Langevin equation satisfies the FP given by Eq. (9); see the proof in Ref. [25].

Notably, any process $x_\tau(\tau)$ generated with Eq. (11) is a continuous diffusion process. Such a diffusion process refers to a continuous-time stochastic process with (almost surely) continuous sample paths having the Markov property. Actually, a fundamental example of a continuous diffusion process is a Wiener process. Moreover, the process $x_\tau(\tau)$ generated by Eq. (11) also satisfies the Lipschitz condition, i.e., for any function $f:\mathbb{R}\to\mathbb{R}$, and $x_1,x_2\in\mathbb{R}$, there exists a constant $\epsilon>0$ such that $|f(x_1)-f(x_2)|\leqslant\epsilon\,|x_1-x_2|$.

On the other hand, in terms of the probabilities $\mathbb{P}:\mathcal{F}\to\mathbb{R}^+$, where $\mathcal{F}$ is an event space, we can say that the continuous process $x_\tau(\tau)$, generated by the Langevin equation, fulfills a continuity Lindenberg's (Dynkin's) condition, if, for any $\epsilon>0$,

$$\lim_{\tau\to 0^+}\frac{\mathbb{P}[|x_\tau(\tau)|>\epsilon\,|X(\tau)=x]}{\tau}=0. \tag{12}$$

Deviation from this continuity criterion implies a lack of smoothness of the process, signifying the presence of discontinuous events such as jumps. Consequently, for the process with nonvanishing higher-order KM coefficients, the Lindenberg's continuity condition of Eq. (12) can be rewritten as a continuity condition in terms of conditional moments $M^{(k)}$, for $k\geqslant 0$ and any $\epsilon>0$,

$$\lim_{\tau\to 0^+}\frac{\mathbb{P}[|x_\tau(\tau)|>\epsilon\,|X(\tau)=x]}{\tau}\leqslant\frac{M^{(k)}(x_\tau,\tau)}{\epsilon^k\,\tau}, \tag{13}$$

which can be proven using the Chebyshev inequality; see [26].

The Langevin equation (11) [characterized by vanishing higher-order ($k\geqslant 3$) KM coefficients] generates continuous sample paths. However, complex systems often manifest nonstationary dynamics, leading to discontinuous sample paths in the corresponding time series [25]. This poses a challenge when employing the Langevin approach. Apparently, distinct features such as heavy tails or some abrupt large jumps may imply the existence of discontinuous jump components [27]. Models with jumps have been employed to capture this randomness [28]. Their primary challenge yet involves estimating parameters defining jumps and their distribution sizes, along with addressing path discontinuities in processes sampled at discrete intervals. Remarkably, this nonparametric estimation enables one to examine potential nonlinearities in drift, diffusion, and the intensity of the discontinuous *jump* component. This component can be related to the nonvanishing higher-order KM coefficients. Therefore, a SDE that describes a stochastic *jump-diffusion* process is of the following form [see [27]]:

$$dx_\tau(\tau)=h(x_\tau,\tau)d\tau+g(x_\tau,\tau)dW(\tau)+\xi(x_\tau,\tau)\,dJ(\tau), \tag{14}$$

where $J(\tau)$ represents a timescale-homogeneous Poisson jump process, with a jump rate $\lambda(x_\tau)$, a size $\xi(x_\tau,\tau)\sim\mathcal{N}(0,\sigma_\xi^2)$, and a jump amplitude σ_ξ^2. In this process, the diffusion coefficient and a jump characteristics contribute to the second-order KM coefficient. Notably, all unknown functions and coefficients can be directly derived from the empirical data. This approach is suitable for both stationary and nonstationary time series, where discontinuous jump components are present, which would need further investigation; cf. Ref. [27].

IV. RESULTS

We focus on Markovian characteristics at much finer millisecond scales. Certainly, this allows one to extend our analysis beyond the inertial range [10,11], with a particular emphasis on magnetic field fluctuations, as has already been analyzed in Refs. [19,20].

In our endeavor to better understand the turbulence mechanisms within space plasma, we analyze fluctuations not only of the magnetic field $B=|\mathbf{B}|$, but also of ion velocity $V=|\mathbf{V}|$. Namely, we have now applied this approach to the small-scale, in cases (a) and (c), and the medium-scale, in case (b), fluctuations of B, while for V fluctuations, to medium scales in cases (a) and (c), and a higher scale in case (b).

A. Stationarity

It is necessary to validate the stationarity of the data time series under investigation, as described in Sec. III A. To evaluate this feature, we have used the statistical tests, namely, the *Augmented Dickey-Fuller* (ADF) test [29], as well as the

Kwiatkowski-Phillips-Schmidt-Shin (KPSS) test [30], as described in Appendix A.

Using the ADF test, we have determined that in cases (a) and (b), for both variables $B = |\mathbf{B}|$ and $V = |\mathbf{V}|$, respectively, the corresponding p values are less than 0.01. This signifies the rejection of the null hypothesis. Consequently, the time series of magnetic field strength and ion velocity can be considered stationary. Nevertheless, for case (c), where the dataset is substantially smaller for both variables, the computed p values equal 0.154 and 0.3705, for B and V, respectively, indicating the inability to reject the null hypothesis. These values point towards the presence of some nonstationary component in the time series, implying a time-dependent structure with possibly fluctuating variance over time. Using the differencing method (lag-1 difference), we could get rid of this nonstationarity. Then the ADF test results in a p value of <0.01, which leads again to the rejection of the null hypothesis.

Next, we have also employed the KPSS test on both variables $B = |\mathbf{B}|$ and $V = |\mathbf{V}|$. It turned out that in all of the analyzed cases (a)–(c), the resulting p values are <0.01, which means that we reject the null hypothesis. This implies that our time series does have a unit root [which was already confirmed by the ADF test in case (c)], and it is rather nonstationary. In such a case, when the ADF test concludes stationarity, while the KPSS test suggests nonstationarity (presence of a unit root), this means that the series are difference stationary. Hence, to achieve stationarity, a straightforward lag-1 differentiation is usually sufficient. Indeed, after applying this operation, the resulting p values are greater than 0.1 in all of the cases, demonstrating that we do not have sufficient evidence to reject the null hypothesis. Consequently, this signifies that both time series of magnetic field strength $B = |\mathbf{B}|$ and ion velocity $V = |\mathbf{V}|$ can be considered stationary.

B. Chapman-Kolmogorov condition

The basis of adopting the Markov analysis relies on the assumption that the data follow Markovian characteristics. This can be subjected to direct verification through the definition given by Eq. (4). To establish the applicability of a Markov processes framework in our context, we can check the required CK condition, using a method described in Sec. III B. Although, to validate this necessary condition, we briefly discuss the integration limits of the right-hand side of this equation, which formally extends over the set of real numbers. We see that (τ_1, τ', τ_2) represents a set of fluctuation scales.

Note that τ_1 has been chosen to be approximately three times greater than Δt_B, which determines a lower-bound scale in relation to the Einstein-Markov scale [31]. This lower bound represents a finite step size introducing a coarse-grained structure to the evolution of τ across scales, from the largest to the smallest scale. As a result, the Markov process can be interpreted as a stochastic model that effectively represents this continuous coarse-grained process.

Within Eq. (4), the integration is performed over x' representing fluctuations at scale τ'. In the calculations, it is possible to determine bounds for x' based on various quantiles, such as the 5% and 95%, or more robustly, the 1% and 99% quantiles, or even more rigorously. These values are derived from time series at timescales τ'. Formally, for a sufficiently large sample, the result of the integration should remain consistent, independently of the chosen limits. This implies that the chosen limits should be properly extensive. By using such a parametric case study, a consistent plateau can be identified for the well-defined limits of the integration.

Hence, using a methodology described in Sec. III B, we have obtained the empirical cPDFs from the data, denoted as $P_E(x_1, \tau_1|x_2, \tau_2)$, as presented in Figs. 1–3, plotted as continuous contours with the matching various colors (a) near the bow shock, (b) inside the magnetosheath, and (c) near the magnetopause. They are compared there with the cPDFs, which are solutions of the CK equation (4), labeled as $P_{\rm CK}(x_1, \tau_1|x_2, \tau_2)$, and shown as the black dashed contours. Such a comparison is done under the specific parameter set (τ_1, τ', τ_2), such as $\tau' = \tau_1 + \Delta t_X$, $\tau_2 = \tau_1 + 2\Delta t_X$, for $\tau_1 < \tau' < \tau_2$. Here, Δt_X again denotes a sampling time encompassing each variable B and V, for cases (a)–(c), which are comprehensively described below. Typically, the contour graphs provide a two-dimensional (2D) representation of 3D data.

The results of this comparative analysis for magnetic field increments $x_i = b_i \ \forall_i$ performed at various kinetic scales are displayed in Fig. 2 of Ref. [20], as compared with Fig. 1 of Ref. [11] for the region of large magnetohydrodynamic (MHD) scales. The analogous comparative analysis is now seen in Fig. 1 using ion velocity increments $x_i = v_i$ at various scales, compared with Fig. 2 of Ref. [11]. More precisely, in cases (a) and (c), with lower time separation $\Delta t_V = 0.15$ s, we have taken into account the following scales: $\tau_1 = 0.3$ s, $\tau' = \tau_1 + \Delta t_V = 0.45$ s, and $\tau_2 = \tau_1 + 2\Delta t_V = 0.6$ s. In case (b), with much lower resolution $\Delta t_V = 4.5$ s, we have used $\tau_1 = 9$ s, $\tau' = \tau_1 + \Delta t_V = 13.5$ s, and $\tau_2 = \tau_1 + 2\Delta t_V = 18$ s. Again, the isolines shown in the graphs indicate decreasing levels of cPDFs for velocity increments v_i from the central region of each plot. They are as follows: in case (a), 0.4, 0.16, 0.09, 0.04, 0.02, 0.01, and 0.006; in case (b), 0.2, 0.031, 0.023, 0.015, 0.009, 0.005, 0.003; while in case (c), 0.4, 0.145, 0.09, 0.07, 0.04, 0.03, and 0.015. We observe that in the central parts, the contour lines corresponding to $P_E(\cdot|\cdot)$ and $P_{\rm CK}(\cdot|\cdot)$ overlap quite well in cases (a) and (b), and somewhat less in case (c). We see pronounced irregularities caused by the limited data available for estimating PDFs near the edges of the plots, especially in case (c). Hence, in such regions, the explicit verification of the suitability of the CK equation (4) might not be directly possible. Nevertheless, towards the central parts of the contours, we can observe that the CK equation (4) is sufficiently well fulfilled in the first two cases, and approximately satisfied in the third case.

In addition, to analyze the superposed *locality* of fluctuations, as thoroughly described in Sec. III B, we have derived the empirical cPDFs $P_E(x_1, \tau_1|y_2, \tau_2)$ and $P_E(y_1, \tau_1|x_2, \tau_2)$, as well as the solutions of a generalized CK equation (5), given by cPDFs $P_{\rm CK}(x_1, \tau_1|y_2, \tau_2)$ and $P_{\rm CK}(y_1, \tau_1|x_2, \tau_2)$, respectively. One should note that the time stamps of the resolution for the B and V variables for *in situ* measurements by the MMS should receive greater attention. We have noticed slight shifts in the time stamps, but they are very comparable (up to several milliseconds), and thus we have concluded that these shifts are negligible. To begin with, to achieve an

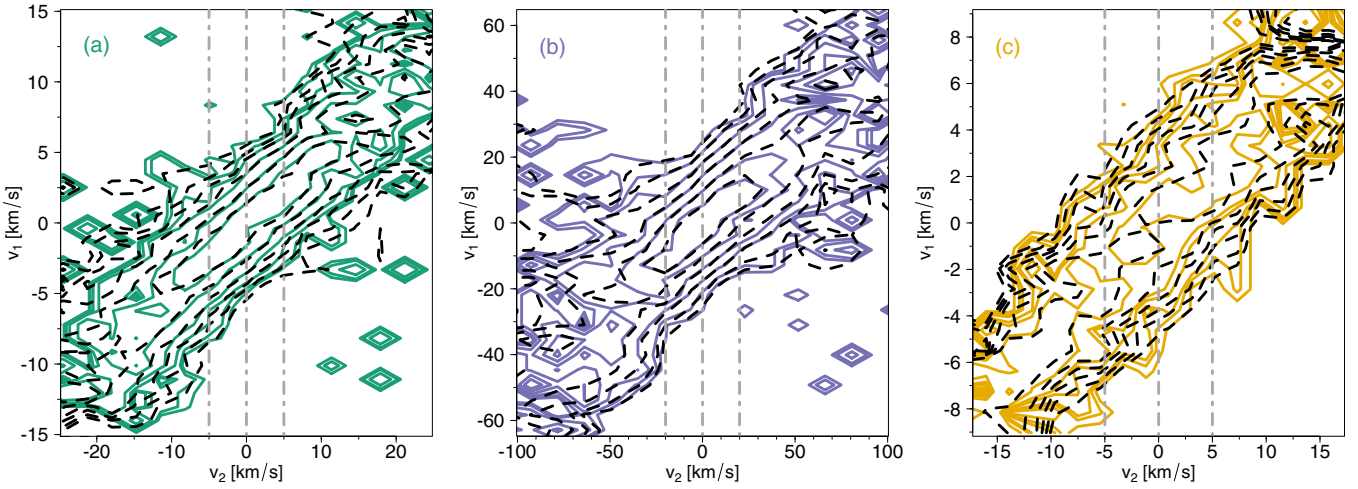

FIG. 1. A comparison between the experimental contours of cPDFs, $P_E(v_1, \tau_1|v_2, \tau_2)$ (depicted as solid various-colored curves), and the reconstructed CK contours of cPDFs, $P_{\rm CK}(v_1, \tau_1|v_2, \tau_2)$ (shown as dashed black curves), for different timescales using the CK condition (4). Data from the MMS mission for ion velocity $V = |\mathbf{V}|$, in three cases: (a) near the bow shock, (b) inside the magnetosheath, and (c) near the magnetopause.

"equilibrium" between the two analyzed variables, we have employed methods of upsampling (linear interpolation) and downsampling (decimation) of data, as elaborated in Appendix B.

Namely, in case (a), with $\Delta t_B = 0.0078\,\text{s}$ and $\Delta t_V = 0.15\,\text{s}$, we have performed a downsampling on the magnetic field variable to obtain a consistent time resolution of $\Delta t_{BV} \sim 0.15\,\text{s}$, resulting in ∼2000 data points. In turn, in case (b), with $\Delta t_B = 0.0625\,\text{s}$ and $\Delta t_V = 4.5\,\text{s}$, because of the risk of substantial loss of information through a straightforward downsampling (loss of too many, e.g., 1 per 72 observations), we have opted for linear interpolation on the variable of ion velocity V joined with downsampling on magnetic field variable B. This has yielded a time resolution of roughly $\Delta t_{BV} \sim 2.25\,\text{s}$, with a dataset consisting of 5500 points. To enhance the clarity of the results in case (c), we have applied the same joint methodology to have a longer (initially severely constrained) variable of velocity V. This results in a satisfactory time resolution of $\Delta t_{BV} \sim 0.075\,\text{s}$, with about 1500 data points, that facilitates a generation of the specific set of scale parameters (τ_1, τ', τ_2). Similar to the previous one-variable cases, $\tau_1 = 0.3\,\text{s}$ in case (a), $\tau_1 = 4.5\,\text{s}$ in case (b), and $\tau_1 = 0.15\,\text{s}$ in case (c), while $\tau' = \tau_1 + \Delta t_{\rm BV}$ and $\tau_2 = \tau_1 + 2\Delta t_{BV}$.

Since the exchange between magnetic and kinetic energy is through magnetic field line stretching, expressed as $\mathbf{b} \cdot \nabla \mathbf{v} \cdot \mathbf{b}$, then physically the intermediate-scale quantities are $x' = b'$ and $y' = b'$ in Eq. (5) in the transfer velocity-to-magnetic field ($x_1 = b_1$ and $y_2 = v_2$) and magnetic-to-velocity field ($x_1 = v_1$ and $y_2 = b_2$), respectively. Although both x' and y' as intermediate-scale quantities are mathematically rigorous, only one selected version of Eq. (5) should be used,

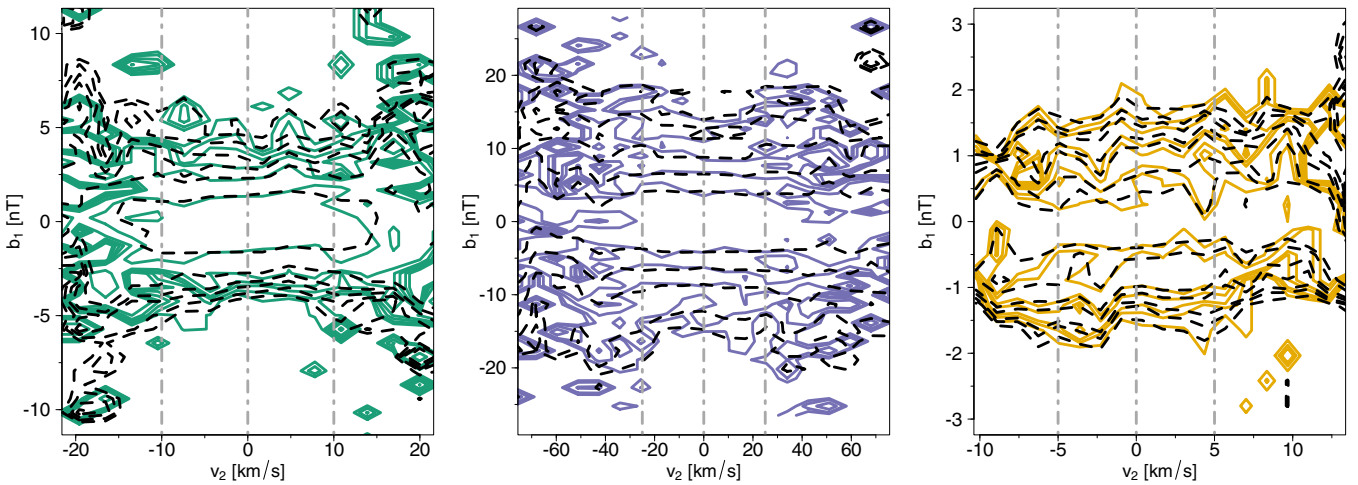

FIG. 2. A comparison between the experimental contours of cPDFs, $P_E(b_1, \tau_1|v_2, \tau_2)$ (depicted as solid various-colored curves), and the reconstructed CK contours of cPDFs, $P_{\rm CK}(b_1, \tau_1|v_2, \tau_2)$ (shown as dashed black curves), for different timescales using the generalized CK condition (5) with $x' = b'$. Data from the MMS mission for a V to B transfer of fluctuations, in the same three analyzed cases.

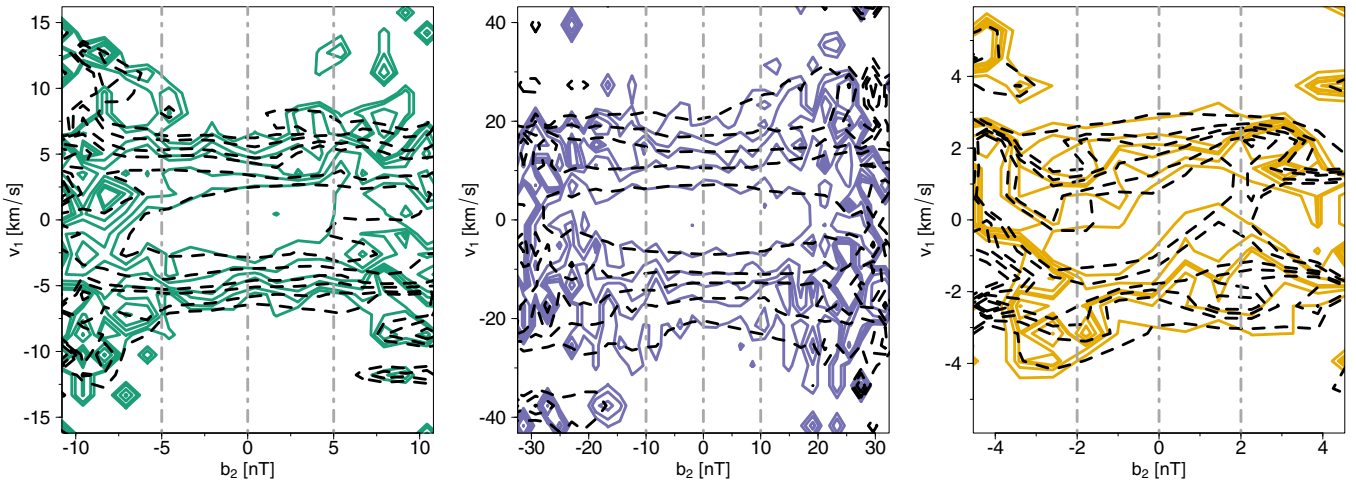

FIG. 3. A comparison between the experimental contours of cPDFs, $P_E(v_1, \tau_1|b_2, \tau_2)$ (depicted as solid various-colored curves), and the reconstructed CK contours of cPDFs, $P_{\rm CK}(v_1, \tau_1|b_2, \tau_2)$ (shown as dashed black curves), for different timescales using the generalized CK condition (5) with $y' = b'$. Data from the MMS mission for a B to V transfer of fluctuations, in the same three analyzed cases.

as mentioned in Sec. III B. The results for both cases of the comparison of the exchange of energy between the velocity and the magnetic fields on kinetic scales are presented as contours in Figs. 2 and 3, correspondingly.

Further, the isolines displayed in the graphs represent decreasing levels of the cPDFs for magnetic field increments b_i, from the center of the plots. For the velocity-to-magnetic case, we show the isolines originating from the middle of the plots set as follows: 0.3, 0.14, 0.07, 0.045, 0.035, 0.025, 0.018 in case (a); 0.2, 0.055, 0.03, 0.017, 0.011, 0.007, 0.004 in case (b); and 0.4, 0.25, 0.16, 0.14, 0.11, 0.09, 0.06 in case (c). Since the energy released from the magnetic field should be equal to the energy obtained by the velocity field, the transfer of velocity-to-magnetic fluctuation should be approximately the same (with opposite signs) as the magnetic-to-velocity exchange, similarly to what has also been computed for MHD scales; see Figs. 5 and 6 in Ref. [11].

Figures 2 and 3 show that both experimental and theoretical contours align quite well in the central parts and to a slightly lesser extent in the outer regions of cases (a) and (b). However, these fits are less pronounced than in the transfer of fluctuations of the same quantity. Additionally, in case (c), one sees a discrepancy even in the center parts, especially in the case of magnetic-to-velocity transfer. We think that these irregularities are primarily related to the limited amount of the data available here. Anyway, these observations suggest that the fulfillment of the generalized CK equation (5) is rather tangible in cases (a) and (b), but admittedly may not be conclusive in case (c). Please note the gray vertical dashed lines in each contour plot (Figs. 1–3) across all investigated cases.

Further, to provide supplementary validation of the proposed CK condition (4) and the generalized CK condition (5), we have also examined the cross sections through the 3D histograms of the cPDF for specific increments $x_i = v_i$ or $x_i = b_i$, for the respective v_i–v_i, b_i–v_i, and v_i–b_i transfers of fluctuations, as illustrated in Figs. 4–6, respectively. The approximated (discretized) fixed values of each parameter are given at the uppermost part of each plot. As can be seen, the slices (cross sections) through the empirical cPDFs, $P_E(\cdot|\cdot)$, plotted as colored filled circles, align quite well with the slices through the theoretical curves, $P_{\rm CK}(\cdot|\cdot)$, shown with black dashed curves, yielding a very good agreement with the CK condition of Eq. (5) in all of the examined cases; cf. [20], Fig. 3 (for the transfer of magnetic-to-magnetic fluctuations, $x_i = b_i$ and $x_i' = b_i$). The slight deviations in tails observed on a few graphs can be attributed to the limited data used for the unsupervised binning method (see Appendix B). For the fixed values of $b_2 < 0$ (nT) and $b_2 > 0$ (nT), we see (on top of each plot) a slight shift and truncation of the PDFs, which is prominent especially in cases (a) and (b), and to a lesser degree, in case (c).

It is important to highlight that our extensive comparisons across various parameter sets (τ_1, τ', τ_2) have yielded convincing results. In particular, we have found that the CK condition (4) holds true for $x_\tau = b_\tau$ as τ increases [20], Fig. 3. When Δt_B attains somewhat higher values, indicating that τ_2 becomes sufficiently large, the CK condition remains satisfied, but sometimes both cPDFs no longer exhibit dependence on b_2. Nevertheless, this broader insight in analyzed space regions suggests that the turbulent cascade usually has Markov properties also on kinetic scales.

Admittedly, in Fig. 4, for the velocity-to-velocity transfer fluctuations, we see that the alignment is slightly less clear than that observed in the case of magnetic-to-magnetic fluctuations in Fig. 3 of Ref. [20]. The most accurate fits are seen in case (a), but minor deviations are encountered in the tails of each PDF. Rather good fits are observed in case (b), though numerical noise is present even in the central peaked part of each PDF. Admittedly, the least precise fitting emerges in case (c). In general, for fixed values of $v_2 < 0$ (km s^{-1}) and $v_2 > 0$ (km s^{-1}) (see top of each plot), the shapes of the PDFs can exhibit some asymmetry, which may be attributed to higher moments of PDF in Eq. (8). In the former case, the obtained PDF shape seems to be somewhat right-skewed, while in the latter situation, a tendency to a left-skewed shape is rather apparent. Additionally, the shapes in cases (a) and (b) exhibit greater peakedness, whereas in case (c), we observe

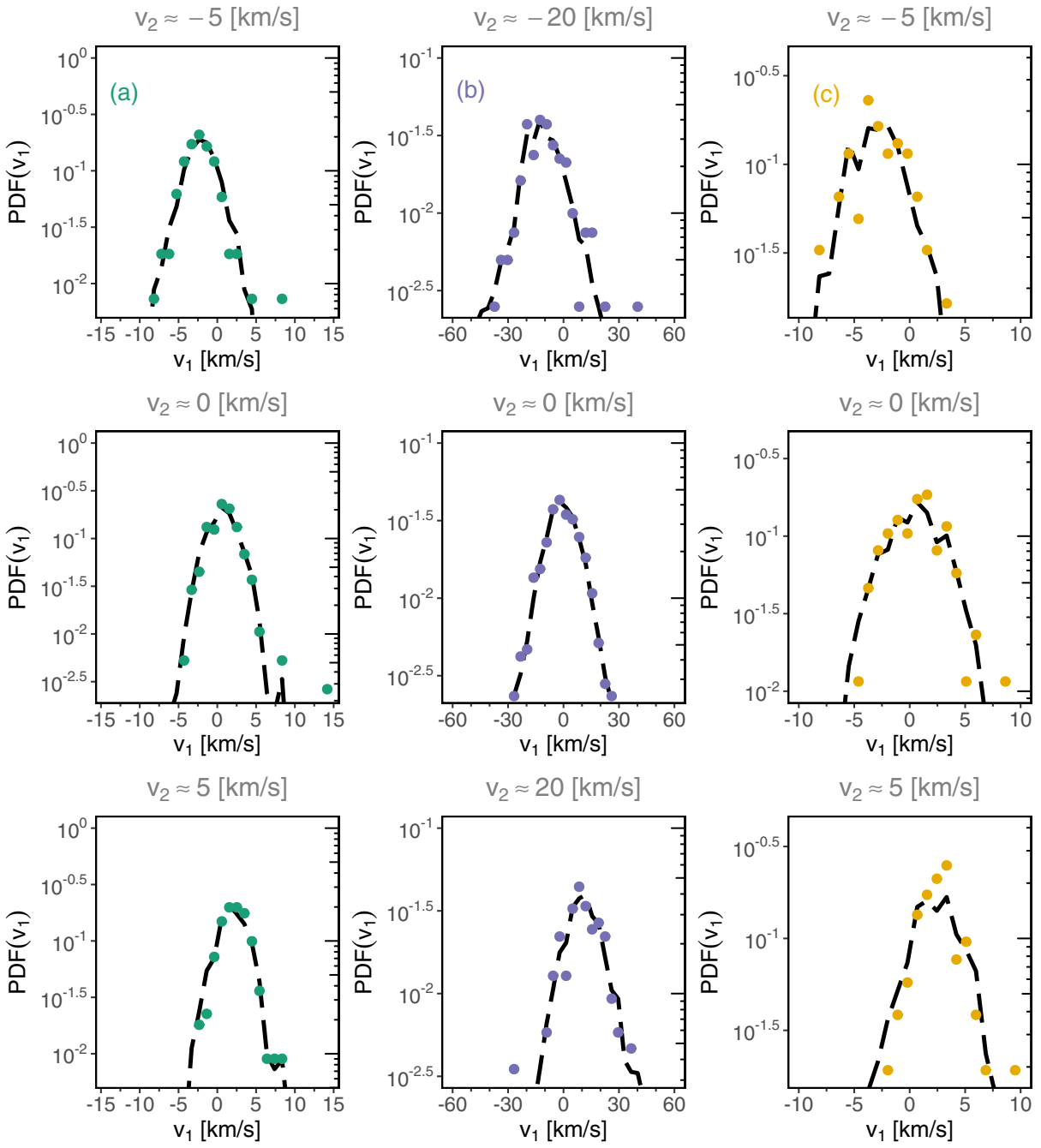

FIG. 4. Comparison of the experimental cross sections through the cPDFs $P_E(v_1, \tau_1|v_2, \tau_2)$ (colored filled circles) and $P_{CK}(v_1, \tau_1|v_2, \tau_2)$ (black dashed lines), under fixed ion velocity fluctuation v_2 (on top of each graph) for cases (a) behind the bow shock, (b) inside the magnetosheath, and (c) near the magnetopause. The parameter set (τ_1, τ', τ_2) is in agreement with that in Fig. 1.

somewhat smoother shapes. Apart from that, both of the first PDFs match quite well; also in case (c), the fits are fairly acceptable.

It is also relevant to discuss the extent to which the CK condition given by Eq. (4) is satisfied for the $x_i = v_i$ variable. After a comprehensive analysis involving numerous parameter sets (τ_1, τ', τ_2) akin to the previous scenario, the following observations emerge. In case (a), this condition is approximately well satisfied up to $50\Delta t_V = 7.5$ s, corresponding to $\tau_2 = \tau_1 + 50\Delta t_V = 7.8$ s. Next, in case (b), it remains valid for scales up to $30\Delta t_V = 135$ s, which gives $\tau_2 = \tau_1 + 30\Delta t_V = 144$ s. In case (c), it is somewhat fulfilled, albeit up to $5\Delta t_V = 0.75$ s, namely, $\tau_2 = \tau_1 + 5\Delta t_V = 1.05$ s. Once again, our observations affirm the presence of Markovian properties within the turbulent cascade as the analysis is able to look at the domain of kinetic scales.

Afterwards, we consider the transfer of fluctuations between the two quantities: velocity-to-magnetic and magnetic-to-velocity. Here we present the cross sections on kinetic scales in Figs. 5 and 6, respectively, which should be

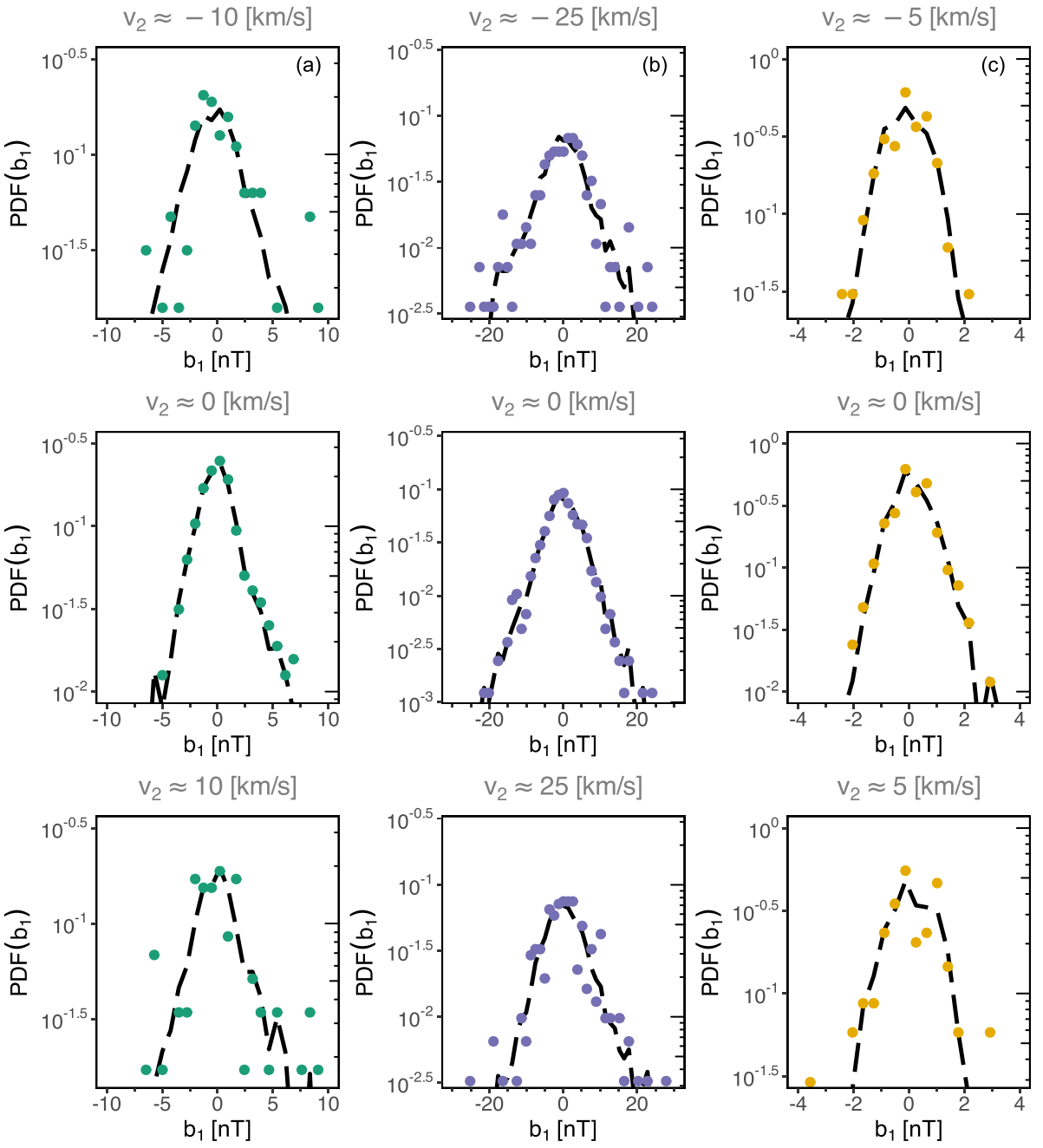

FIG. 5. Comparison of the experimental cross sections through the cPDFs $P_E(b_1, \tau_1|v_2, \tau_2)$ (colored filled circles) and $P_{\mathrm{CK}}(b_1, \tau_1|v_2, \tau_2)$ (black dashed lines), under fixed ion velocity fluctuation v_2 (on top of each graph) for cases (a) behind the bow shock, (b) inside the magnetosheath, and (c) near the magnetopause. The parameter set (τ_1, τ', τ_2) is in agreement with that in Fig. 2.

compared with the corresponding Figs. 7 and 8 of Ref. [11] for MHD scales. Notably, the circles representing empirical cPDFs exhibit a reasonable fit with the slices through the solutions of the generalized CK of Eq. (5). The most accurate fit is seen in case (b), with a slightly less precise fit in case (a), while the most significant deviations are apparent in case (c). The deviations in the tails are present, which can be attributed to some outliers, which are more challenging to understand and potentially remove in this joint method for limited data. In addition, slight shifting and truncation of the PDFs are observed, in particular in case (c).

This analysis suggests that the fulfillment of the appropriate CK condition (5) is at least approximately satisfied for the smallest considered range of scales available for testing. Our results provide supporting evidence that the Markov approach can be applied for the description of the turbulent cascade in solar wind turbulence. Therefore, the assumption of locality of the energy transfer in wave-vector space is valid, and thus

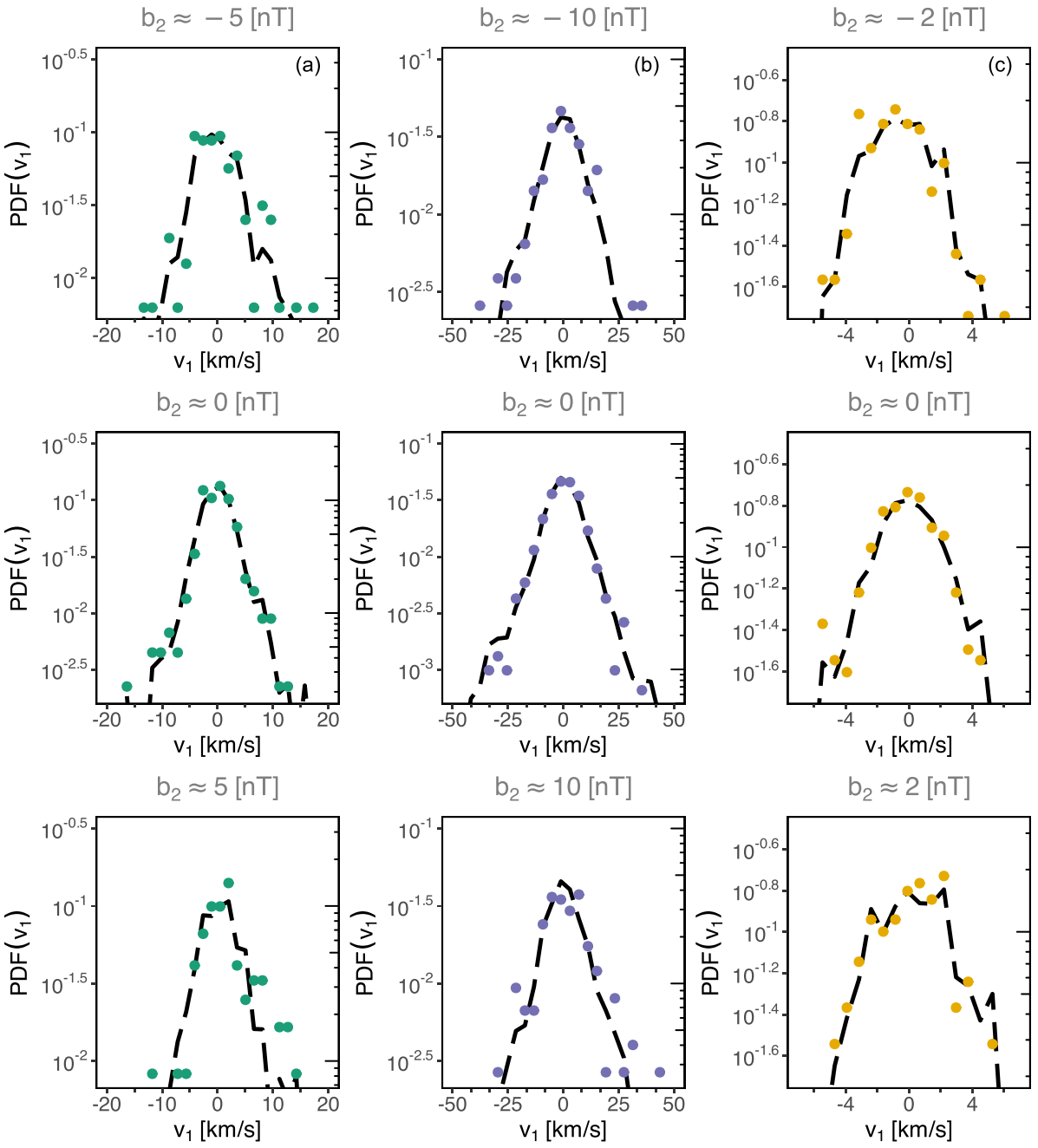

FIG. 6. Comparison of the experimental cross sections through the cPDFs $P_E(v_1, \tau_1|b_2, \tau_2)$ (colored filled circles) and $P_{\mathrm{CK}}(v_1, \tau_1|b_2, \tau_2)$ (black dashed lines), under fixed magnetic field fluctuation b_2 (on top of each graph) for cases (a) behind the bow shock, (b) inside the magnetosheath, and (c) near the magnetopause. The parameter set (τ_1, τ', τ_2) is in agreement with that in Fig. 3.

our analysis extends the findings in the near-Earth space environment to small kinetic scales.

C. Drift and diffusion coefficients

This further allows estimating the KM coefficients and checking the validity of Pawula's theorem as discussed in Sec. III C. Naturally, we have determined the KM coefficients of orders $k = 1, 2$, and 4, defined by Eq. (7). These coefficients bear crucial importance for the validation of Pawula's theorem, described in Sec. III B. The conventional approach employed for the determination of these coefficients involves the application of an extrapolation technique, for instance, the piecewise linear regression (mentioned in Sec. III B), to estimate the corresponding limits as $\tau \to \tau'$. It is important in this regard to recall the Einstein-Markov scale, below which the process is no longer Markovian. In our case, this derived scale is not too high, and the sampling rate is adequately high, thus not significantly affecting the determination of the KM coefficients. However, for $M^{(k)}(x_\tau, \tau, \tau')$ as a function of τ', we have noticed a consistent deviation from a linear fit for small values of τ' in Eq. (8), attributed to the Einstein-Markov scale

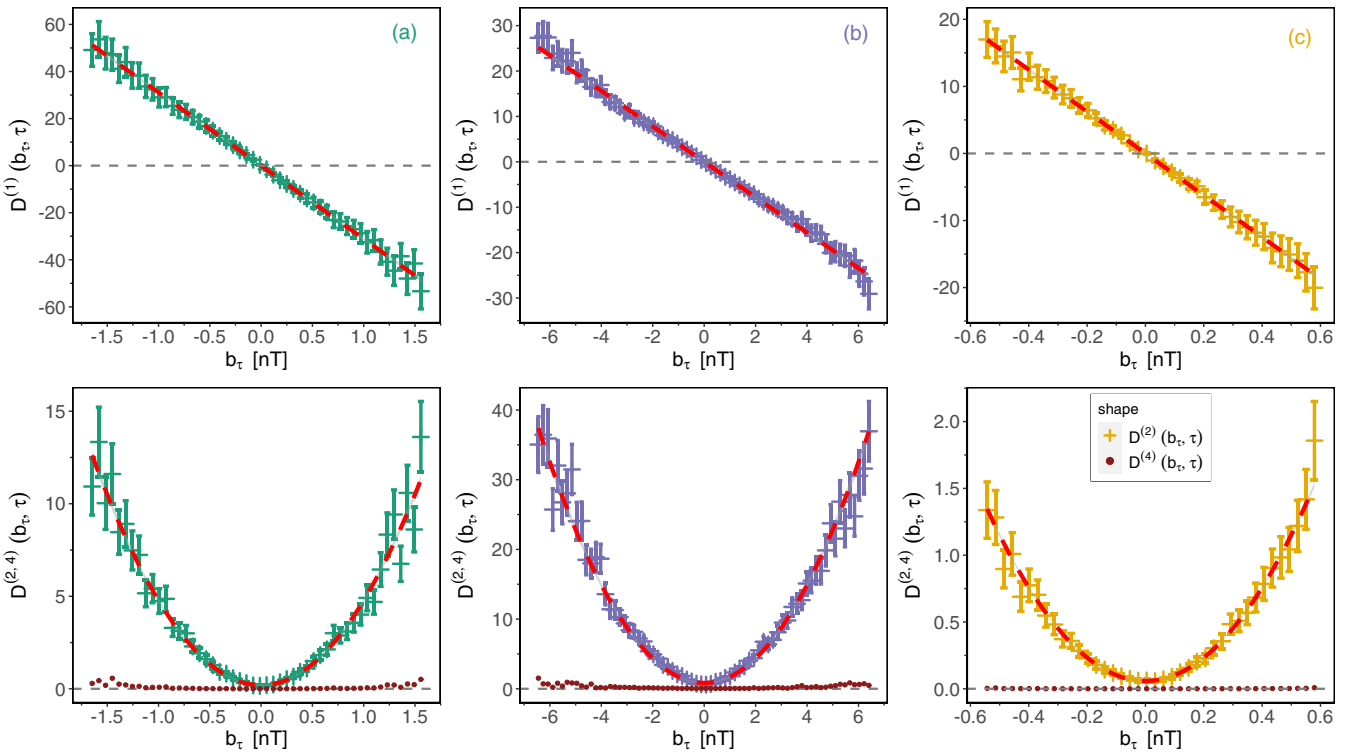

FIG. 7. The first and second Kramers-Moyal coefficients as functions of magnetic field increments b_τ, for the magnetic field strength $B = |\mathbf{B}|$. Dashed red lines represent the optimal fits to the empirical values of $D^{(1)}(b_\tau, \tau)$ and $D^{(2)}(b_\tau, \tau)$, while $D^{(4)}(b_\tau, \tau) \approx 0$ (brown dots), maintaining the condition in agreement with Pawula's theorem, taken from Ref. [20].

(not shown here) that ought to be omitted when calculating the limits; see, e.g., [8], Fig. 14 and [12], Fig. 42. Therefore, we have directly computed these scaled central moments, using the obtained empirical cPDFs $P(x_1, \tau_1|x_2, \tau_2)$, for $0 < \tau_1 < \tau_2$. This systematic approach has yielded the empirical KM coefficients $D^{(k)}(x_\tau, \tau)$ obtained using point-by-point extrapolation of the $M^{(k)}(x_\tau, \tau, \tau')$ coefficients.

In addition, since the errors of the number of occurrences $N(x'_\tau, x_\tau)$ of fluctuations x'_τ and x_τ can be resolved by $\sqrt{N(x'_\tau, x_\tau)}$, we have used an analogous reasoning to determine the errors of the scaled conditional moments $D^{(k)}(x_\tau, \tau)$, [see, e.g., 8]. Consequently, Figs. 7 and 8 provide the first-order coefficient (in the upper segment), and the second- and fourth-order coefficients (in the lower segment) for b_τ and v_τ fluctuations, respectively. These graphs cover all three cases (a), (b), and (c), which are distinguished, as previously shown, by various colors. For each case, we also present the calculated confidence intervals.

The results depicted in Fig. 7 reveal a distinct pattern: the fit for the drift $D^{(1)}(b_\tau, \tau)$ adopts a linear relationship with respect to b_τ, with negative slope, while diffusion $D^{(2)}(b_\tau, \tau)$ stands as a second-degree (parabolic) function of b_τ. This behavior is consistent for $\Delta t_B = 0.0078$ s in cases (a) and (c), and $\Delta t_B = 0.0625$ s in case (b). Remarkably, our comprehensive analysis extends this fitting to significantly larger scales, up to $150\Delta t_B$, corresponding to $\tau_2 = \tau_1 + 150\Delta t_B$ for all three cases. This robust consistency suggests that fitting to lower-order polynomials for different Δt_B is possible on kinetic scales.

We see that for increments of the magnetic field B, while the drift and diffusion coefficients remain nonvanishing, the fourth coefficient (brown dots) is approximately zero for all cases. Thus, the KM expansion of Eq. (6) truncates at $k = 2$ in cases (a)–(c), hence reducing to the FP equation. This results from Pawula's theorem, also ensuring the statistical continuity of the analyzed process. Therefore, the Markov process can effectively be described by this FP equation (9) (or, alternatively, by the Langevin equation (10); see, e.g., [32]).

In the corresponding Fig. 8, we can notice a pattern similar to that in Fig. 7, but with significantly less pronounced alignment. The fit for the drift $D^{(1)}(v_\tau, \tau)$ follows a clearly discernible linear relationship with respect to v_τ, whereas the diffusion coefficient $D^{(2)}(v_\tau, \tau)$ exhibits a somewhat less apparent quadratic dependence on v_τ. Some moderate deviations from observed behavior are seen, especially in cases (a) and (c), with $\Delta t_V = 0.15$ s, and to a lesser extent in case (c), with $\Delta t_V = 4.5$ s. Contrary to the magnetic case, we now see that the KM expansion of Eq. (6) does not stop for $k \geqslant 3$, suggesting that truncation of expansion at any finite lower order would result in some not entirely credible PDFs, which cannot be reconstructed using the FP or Langevin equations [24]. Basically, since the Pawula's theorem is not well satisfied, we can expect that to maintain the Markovian property of the process for velocity fluctuations, considering the higher-order coefficients in the KM equation (6) (possibly for $k \to \infty$) would be necessary. Our results indicate that the observed time series somewhat deviates from the class of continuous

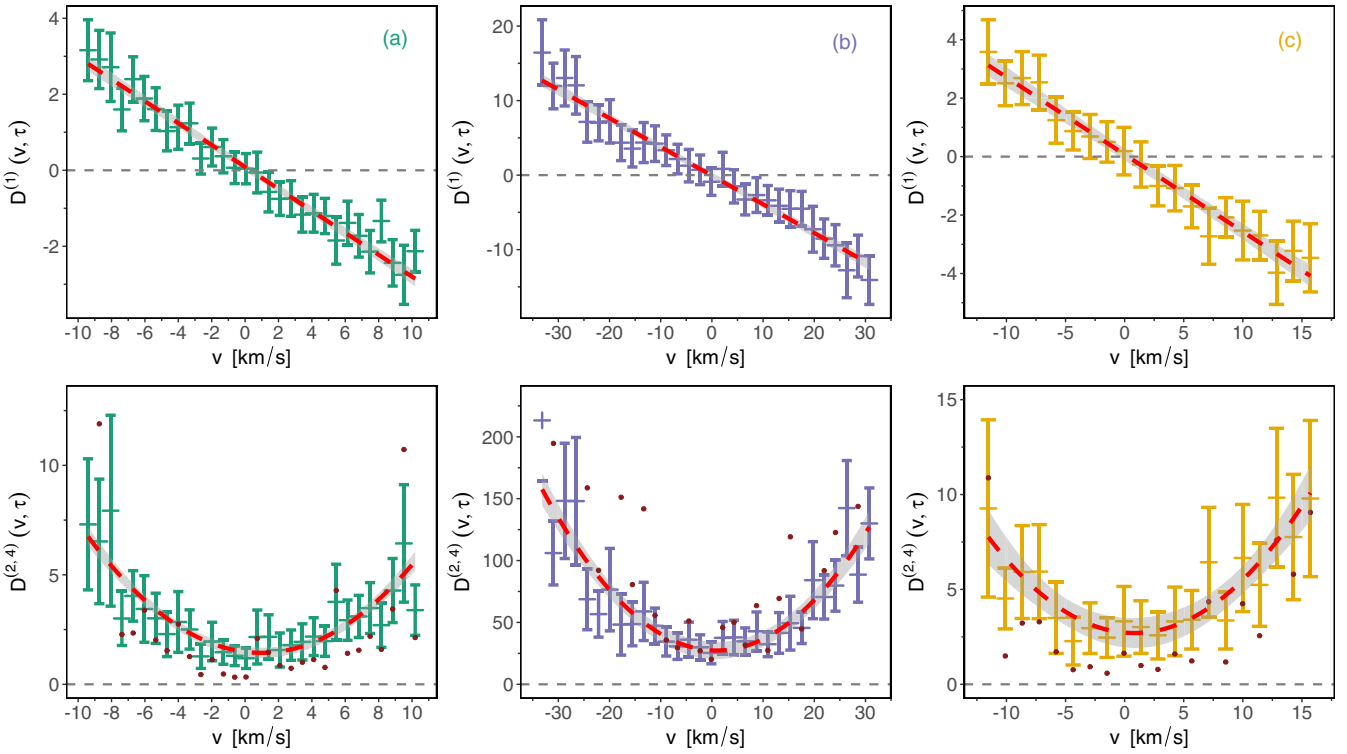

FIG. 8. The first and second Kramers-Moyal coefficients as functions of ion velocity increments v_τ, for the ion velocity $V = |\mathbf{V}|$. Dashed red lines represent the optimal fits to the empirical values of $D^{(1)}(v_\tau, \tau)$ and $D^{(2)}(v_\tau, \tau)$, with $D^{(4)}(v_\tau, \tau) \neq 0$, i.e., not maintaining the Pawula's theorem.

diffusion processes (discussed in Sec. III C), which may point to the influence of some jump events within the underlying stochastic process [27], which would need some more investigation.

D. Distributions and entropies

It is worth noting that for the stationary solutions of the FP given by Eq. (9), the probability current must be constant. Hence, the following formula can be derived (see Sec. 5.2 of Ref. [24]):

$$p_s(x,\tau) = N_0 \exp\left[\int_{-\infty}^{x} \frac{D^{(1)}(x')}{D^{(2)}(x')}\,dx' - \ln D^{(2)}(x)\right]. \quad (15)$$

In this way, with a linear $D^{(1)}(b,\tau) = -a_1(\tau)b$ and a quadratic $D^{(2)}(b,\tau) = a_2(\tau) + b_2(\tau)b^2$, for the magnetic case, the stationary solution of Eq. (15) becomes a PDF of the *Kappa* distribution, given by [19]

$$p_s(b,\tau) = \frac{N_0}{\left[1 + \frac{1}{\kappa}\left(\frac{b}{b_0}\right)^2\right]^\kappa}, \quad (16)$$

where $\kappa = 1 + \frac{a_1(\tau)}{2b_2(\tau)}$ is a shape parameter and $b_0 = \sqrt{\frac{a_2(\tau)}{b_2(\tau)+a_1(\tau)/2}}$ is a scale parameter. The distribution function has to be normalized, $\int_{-\infty}^{\infty} p_s(b,\tau)db = 1$. We obtain

$$N_0 = \frac{1}{\mathcal{B}(\kappa - \frac{1}{2}, \kappa) b_0 \sqrt{\pi\kappa}}, \quad (17)$$

where $\mathcal{B}$ is a mathematical Beta function.

In particular, the Kappa distribution approaches the normal Gaussian distribution for large values of κ. This follows from the properties of the Beta function in the form $\mathcal{B}(\kappa_1,\kappa_2) = \frac{\Gamma(\kappa_1)\Gamma(\kappa_2)}{\Gamma(\kappa_1+\kappa_2)}$, and $\lim_{k\to\infty} \frac{\Gamma(k+\alpha)}{\Gamma(k)k^\alpha} = 1$, for $\alpha \in \mathbb{R}$. Fixing $\alpha = \frac{1}{2}$, and because $\Gamma(\kappa - \frac{1}{2})$ grows asymptotically at the same rate as $\frac{\Gamma(\kappa)}{\sqrt{\kappa}}$, the limit of Eq. (17) is simply given by $\lim_{\kappa\to\infty} N_0 = \frac{1}{b_0\sqrt{\pi}}$. Hence, as $\kappa \to \infty$ in Eq. (16), the well-known formula for the normal density distribution is obtained,

$$\lim_{\kappa\to\infty} p_s(b,\tau) = \frac{1}{b_0\sqrt{\pi}} e^{-\left(\frac{b}{b_0}\right)^2}, \quad (18)$$

with the mean value $\mu = 0$ and the standard deviation $\sigma = \frac{b_0}{\sqrt{2}}$, characterizing this symmetric PDF with extremely small tails. In addition, from the asymptotic expansion using the Stirling's factorial formula, one can show that in this case (with the respective third and fourth central moments μ_3 and μ_4), not only the third κ_3 (skewness) but also the fourth $\kappa_4 = \mu_4/\sigma^4 - 3$ (excess kurtosis) moments both approach zero.

On the other hand, nonzero κ_3 measures the possible asymmetry for left ($\kappa_3 < 0$) or right ($\kappa_3 > 0$) skewed PDF, but the value of κ_4 says how heavily the tails differ from a normal distribution. The Kappa distribution as a special case of the Pearson's type-*IV* family (i.e., a Pearson's type-VII distribution) have been used in numerous studies of solar wind and is important in space plasma physics [e.g., [33]]. This type of PDF is symmetric ($\kappa_3 = 0$) with heavy tail and peaked shape, measured by a positive κ_4 (leptokurtic) or negative κ_4 (platokurtic) kurtosis, which exhibits the deviation from the

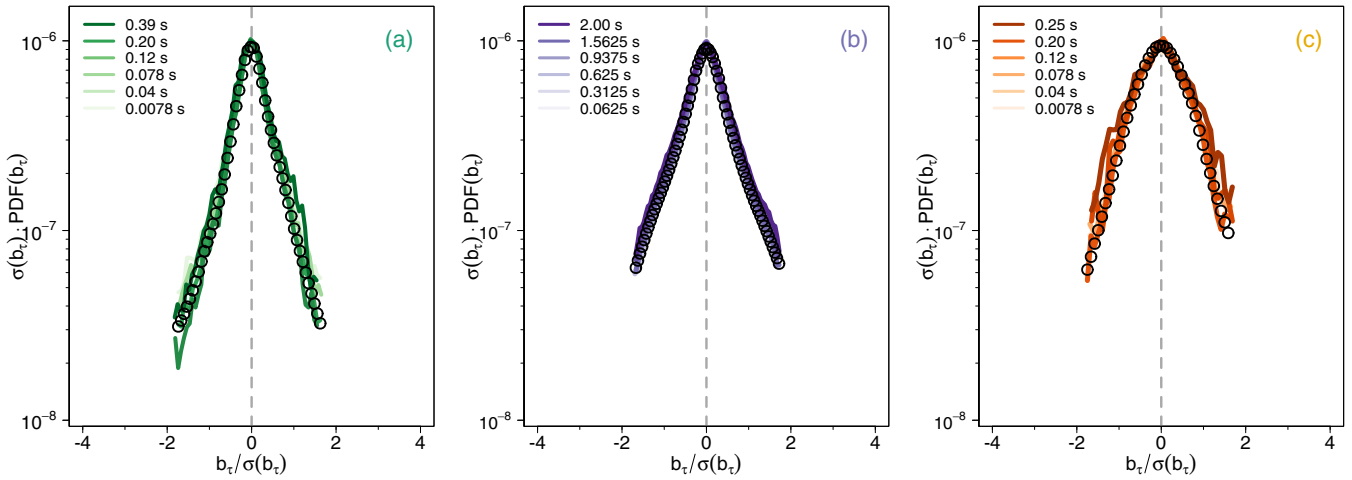

FIG. 9. Comparison between the rescaled empirical cPDFs (various continuous colored lines) and the stationary solutions of the FP equations (black open circles), considering the magnetic field magnitude $B = |\mathbf{B}|$ in all three cases. The global scale invariance can be observed.

standard "bell" shape of the normal (mesokurtic) Gaussian distribution ($\kappa_4 \approx 0$).

Further, as is known, in classical statistical mechanics, Boltzmann additive entropy describes a system in equilibrium. On the other hand, the higher-order nonadditive nonextensive entropy is needed for a nonlinear nonequilibrium system, such as the solar wind at small scales [34]. Tsallis [35] introduced a generalization of the Boltzmann's entropy (with k_B the Boltzmann constant),

$$S_q[p(x)] = \frac{k_B}{q-1}\left\{1 - \int_{-\infty}^{+\infty} [p(x')]^q dx'\right\}, \qquad (19)$$

where $p(x)$ is a given probability distribution, and any real number q is a nonextensive Tsallis parameter, which measures the degree of nonextensivity. For $q \to 1$, the classical Boltzmann-Gibbs information (additive) entropy is recovered, given by $-k_B \int p(x') \ln p(x') dx'$.

To unify power-law behaviors with a proper information measure, we use Tsallis entropy given by Eq. (19). Namely, to relate the derived Kappa distribution, with the Tsallis q-distribution function, a simple transformation can be used, $\kappa = 1/(1-q)$; see, e.g., Ref. [36]. The numerical results of fitting the MMS empirical magnetic data to the given distributions and determining the relevant parameters of Eq. (16) are as follows: $\kappa = 1.5179$, $x_0 = 1.9745$, and $N_0 = 0.68438$ for B in case (a); $\kappa = 1.3758$, $x_0 = 2.6955$, and $N_0 = 0.34375$ in case (b); with $\kappa = 3.5215$, $x_0 = 1.7313$, and $N_0 = 1.1866$ in case (c).

Because the κ parameter depends on $a_1(\tau)$ and $b_2(\tau)$, the KM coefficients can be related to the supposed nonextensive character of the fluctuations. The particular values of this κ parameter can be attributed to the nonextensivity parameter q, which characterizes the generalized Tsallis entropy. In this situation, it is given by $q = \frac{a_1(\tau)}{a_1(\tau)+2b_2(\tau)}$ and is equal to 0.341 in case (a), 0.273 in case (b), and 0.716 in case (c). The extracted values of the κ and q parameters provide robust measures of the departure of the system from equilibrium.

Based on magnetic MMS data, we have already obtained Kappa distributions for various scales, including the leptokurtic shapes for moderate scales (for the smallest scale values 7.8 ms described by a peaked shape close to the Dirac δ function) up to approximately the standard normal Gaussian distribution for the scale two orders of magnitude larger [20], Fig. 6. For relatively higher levels, the distributions still exhibit the peaked shape with high kurtosis, which refers to tails of the PDF. For velocity fluctuations, higher-order Kramers-Moyal coefficients should also be taken into account, with more complicated PDFs with possible slight asymmetry shown in Figs. 4–6.

Figure 9 illustrates the universal global scale invariance of the PDFs up to kinetic scales of (a) $\tau \sim 0.4$ s, (b) $\tau \sim 2$ s, and (c) $\tau \sim 0.25$ s, correspondingly [20]. This monoscaling scale invariance is obtained by rescaling cPDFs by their corresponding standard deviations σ for each case, as explained in Refs. [19,20]. This demonstrates the exceptional agreement between empirical cPDFs and the stationary solutions (denoted by black open circles) of the FP equation (9) provided by the analytic formula of Eq. (16). One can only mention here that these results imply that the mean n-order structure function $S_n(\tau) = \langle b_\tau(t)^n \rangle \sim \tau^{\zeta(n)}$ exhibits a linear (monofractal) scaling, i.e., $\zeta(n) = nH$, with a single Hurst exponent H [37]. It means that in contrast to large magnetohydrodynamic scales (with anomalous scaling), magnetic turbulence on small kinetic scales is not intermittent. Interestingly, several analyses based on Cluster data (we refer to the ESA's Cluster mission) [38,39] report *scale-invariant* behavior, while other analyses support strongly increasing scale-dependent kurtosis and associated departures from self-similarity [40,41] reports that within the kinetic scales, there is a general trend towards large kurtosis at smaller scales.

V. CONCLUSIONS

The Magnetospheric Multiscale mission with unprecedented high millisecond time resolution of magnetometer data allows us to investigate turbulence on very small kinetic scales [19,20]. In these papers, we looked at the MMS observations above 20 Hz, where the magnetic spectrum becomes very

steep, with the slope close to $-16/3$, possibly resulting from interaction between coherent structures [14].

Now, we have also taken into account plasma data with somewhat lower resolution for ion velocity. Following our previous studies in the inertial region [10,11], we have primarily shown that the Chapman-Kolmogorov equation, which is a necessary condition for the Markovian character of fluctuations, is satisfied for the transfer of energy between the magnetic and velocity fields also on much smaller kinetic scales. In fact, we have proved that a local transfer mechanism is present for transfer of ion velocity-to-velocity, velocity-to-magnetic, and magnetic-to-velocity stochastic fluctuations. This physically means that this energy transfer to smaller scales has a *local* character.

Moreover, we have verified that in the case of magnetic fluctuations, Kramers-Moyal expansion stops after the second term, resulting in the Fokker-Planck equation, with *drift* and *diffusion* terms, at least for scales smaller than (a) $\tau \sim 0.8$ s near the bow shock (BS), (b) $\tau \sim 9$ s inside the magnetosheath (SH), and (c) $\tau \sim 0.8$ s near the magnetopause (MP), correspondingly.

Similarly as for Parker Solar Probe (PSP) data [42], the lowest-order coefficients are linear and quadratic functions of magnetic fluctuations, which correspond to the generalized Ornstein-Uhlenbeck processes. As expected for some moderate scales, we have the Kappa distributions with heavy tails. The observed global universal scale invariance corresponds to a simple *linear* (monofractal) scaling. The extracted values of the nonextensity parameter in Tsallis entropy $q < 1$ equal to 0.341 in case (a), 0.273 in case (b), and (c) 0.716, respectively, provide robust measures of the departure of the system from equilibrium.

On the other hand, for velocity fluctuations, higher-order moments should be taken into account with possibly more complex dependence on the increments of velocity. Therefore, in this case, we also see somewhat more complicated probability density functions. Hence, unlike to the magnetic fluctuations, monoscaling does not occur, suggesting rather *nonlinear* (multifractal) scaling.

Nevertheless, we are still hoping that our observation of Markovian features in solar wind turbulence will be important for understanding the relationship between deterministic and stochastic properties of turbulence cascade on kinetic scales in complex physical systems.

ACKNOWLEDGMENTS

We thank Marek Strumik for discussion on the theory of Markov processes. We are grateful for the efforts of the entire MMS mission, with J. L. Burch, Principle Investigator, C. T. Russell and the magnetometer team, including development, science operations, and the Science Data Center at the University of Colorado. The magnetic field data from the magnetometer are available online [22]. We acknowledge B. L. Giles, Project Scientist, for information about the magnetic field instrument, and D. G. Sibeck and M. V. D. Silveira for discussions during previous visits by W.M.M. to the NASA Goddard Space Flight Center. The data have been processed using the statistical programming language R. We would like to thank the referee for useful comments in relation to the problem of scale invariance of magnetic turbulence. This work has been supported by the National Science Centre, Poland (NCN), through Grant No. 2021/41/B/ST10/00823.

APPENDIX A: TIME SERIES CHARACTERISTICS

The analysis of time series is significant in nonlinear dynamics because a thorough investigation can reveal all the essential information on the dynamical properties of the considered system. To estimate the target variable in predicting or forecasting, one uses the time variable (or in our case, also a timescale) as the reference point. The *time series analysis* involves the examination of the characteristics of the selected variables as a function of time, considered as the independent variable. Time series data for our investigation can be directly extracted from the measurements within the MMS mission.

A basic assumption regarding the data type is referred to as stationarity. Precisely, the time series is said to be stationary if it exhibits no trend, no seasonality, has a constant variance over time, and a consistent autocorrelation function over time. To evaluate this feature, one can plot the data and visually look for trend and seasonal components, although the more robust methods include statistical tests, such as the Augmented Dickey-Fuller (ADF) test [29], and the Kwiatkowski-Phillips-Schmidt-Shin (KPSS) test [30]. The ADF test uses the following hypotheses:

(i) H_0: the time series is nonstationary vs

(ii) H_1: the time series is stationary.

Note that it is set up this way to maintain a skeptical and cautious approach towards the findings. The null hypothesis is assumed to be true until the data present sufficient evidence that it is not. Naturally, when the p value is less than a prechosen significance level, say $\alpha = 0.05$ or, more strictly, 0.01, then the null hypothesis can be rejected, which leads to the conclusion that the time series is stationary. The test for nonstationarity of a time series $\{y_t\}$ observed over T time periods is estimated in the ADF regression model,

$$\Delta y_t = \alpha + \beta t + \gamma y_{t-1} + \sum_{j=1}^{p} \rho_j \Delta y_{t-j} + \varepsilon_t, \tag{A1}$$

where α is a constant, β is a coefficient on a time trend, p is a lag order of the *autoregressive* (AR) process, ε_t is an error term (assumed white noise), and differencing terms $\Delta y_{t-j} = y_{t-j} - y_{t-j-1}$, with coefficients ρ_j. Here in the representation of ADF, the differencing term is added, in contrast to the standard Dickey-Fuller test. Once we get a value for the test statistic $\mathrm{DF}_t = \hat{\gamma}/\mathrm{SE}(\hat{\gamma})$, where SE denotes the standard error of the estimator, it can be compared to the relevant critical value for the Dickey-Fuller test.

Alternatively, the statistical Kwiatkowski-Phillips-Schmidt-Shin (KPSS) test is a type of unit root test. A unit root is a stochastic trend in a time series that can cause problems in statistical inference. The KPSS test is used for assessing the stationarity of a series around a deterministic trend. Namely, we have the following hypotheses:

(i) H_0: the time series is trend stationary or has no unit root vs

(ii) H_1: the time series is nonstationary or has a unit root.

Both the ADF and KPSS tests are frequently used to examine the stationarity of times series. A significant distinction between the ADF test and the KPSS test lies in their null hypotheses. In the KPSS test, the null hypothesis assumes stationarity for the series, while for the ADF test, it implies nonstationarity. Consequently, the practical interpretation of the p value differs in a contrasting manner for these two tests. A p value below a given significance level ($\alpha = 0.05$ or 0.01) implies nonstationarity, whereas for the ADF test, such a p value indicates stationarity of the tested series.

Nevertheless, nonstationary time series can be converted into stationary, e.g., using a differencing method, which is a simple transformation of the series. This process effectively mitigates the series dependence on time and stabilizes its mean, resulting in a reduction of trend and seasonality within the series. The simplest difference between successive observations is called a lag-1 difference. However, one should be careful not to over-difference the time series, as it may lose some important information or features.

It is also worth mentioning that the time series have some limitations. For instance, if the missing values are not supported, some specific tools are needed to effectively address this problem. To fill in the empty data spots, a linear interpolation method can be used. It is a process of estimating the value of a function at a specific point, based on the known values at neighboring points. Hence, it requires knowledge of two points and the constant rate of change between them. The primary distinction between an interpolation and regression methods lies in the requirement to precisely match all data points in interpolation, whereas regression does not demand such an exact fit.

APPENDIX B: DATA TRANSFORMATIONS

To compare the cPDF and use the CK condition (4), some preliminary data transformations are necessary. As is known, the *feature engineering* holds a vital role in the development of data analysis. These features can be time, categorical, and continuous variables. Among the various available techniques, we highlight the *feature binning* method. It is used for the transformation of a continuous or numerical variable into a categorical feature. Binning continuous variables may introduce nonlinearity and typically enhances the model performance. We have employed here a specific binning approach known as *equal-width unsupervised binning*. This method falls within the category of binning techniques that converts numerical or continuous variables into categorical bins, without taking the target class label into consideration. This algorithm segments the continuous variable into multiple categories, each characterized by bins or ranges of equal width. To be precise, in our case, we have begun by estimating the empirical joint PDFs, denoted as $P(x_1, \tau_1; x_2, \tau_2)$. This estimation process involved counting the occurrences of distinct pairs (x_1, x_2) on a two-dimensional grid with equally spaced data bins, each of moderate size. Next we have carried out the normalization to ensure that the integral over all bins is equal to one. In a similar way, we have estimated the empirical one-dimensional PDFs $P(x_2, \tau_2)$ using a one-dimensional grid of bins, followed by the normalization. Finally, to obtain the empirical cPDFs, we have precisely applied the conditional probability formula numerically. The advantage of this approach is that it is simple to implement and interpret, and it preserves the distribution of the analyzed data.

In the same way, to distinguish between the local and nonlocal behavior of fluctuations between two quantities x and y (instead one of these), one needs to estimate the empirical cPDFs by using a generalized CK condition (5). Therefore, because of the difference in time resolutions of both analyzed time series, we must address the grid of time dimension. We can employ either the method of mean downsampling (decimation) or upsampling (interpolation) on the chosen variable. Contrary to a simple linear interpolation briefly described in Appendix A, decimation aims to reduce the original sample rate of the input signal to a lower rate by an integer factor. This factor is just a ratio of the input rate to the output rate. To increase the clarity of the presented graphs and ensure better interpretation of the results, we have opted for double-logarithmic (log-log) and semilogarithmic (log-linear) scales in some specific instances, rather than the standard linear scales. This adjustment of a double-logarithmic scale allows power-law representations to come out as straight lines in the spectra. Additionally, the semilogarithmic scale has been employed in Figs. 4–6, and 9.

[1] U. Frisch, *Turbulence. The Legacy of A. N. Kolmogorov* (Cambridge University Press, Cambridge, 1995).

[2] D. Biskamp, *Magnetohydrodynamic Turbulence* (Cambridge University Press, Cambridge, 2003).

[3] R. Bruno and V. Carbone, *Turbulence in the Solar Wind*, Lecture Notes in Physics (Springer International, Berlin, 2016), Vol. 928.

[4] L. F. Burlaga, *Interplanetary Magnetohydrodynamics*, International Series on Astronomy and Astrophysics (Oxford University Press, New York, 1995).

[5] R. A. Treumann, Astron. Astrophys. Rev. **17**, 409 (2009).

[6] A. Kolmogorov, Akademiia Nauk SSSR Doklady **30**, 301 (1941).

[7] R. H. Kraichnan, Phys. Fluids **8**, 1385 (1965).

[8] C. Renner, J. Peinke, and R. Friedrich, J. Fluid Mech. **433**, 383 (2001).

[9] G. Pedrizzetti and E. A. Novikov, J. Fluid Mech. **280**, 69 (1994).

[10] M. Strumik and W. M. Macek, Phys. Rev. E **78**, 026414 (2008).

[11] M. Strumik and W. M. Macek, Nonlinear Process. Geophys. **15**, 607 (2008b).

[12] R. Friedrich, J. Peinke, M. Sahimi, and M. Reza Rahimi Tabar, Phys. Rep. **506**, 87 (2011).

[13] P. Rinn, P. Lind, M. Wächter, and J. Peinke, J. Open Res. Software **4**, 34 (2016).

[14] W. M. Macek, A. Krasińska, M. V. D. Silveira, D. G. Sibeck, A. Wawrzaszek, J. L. Burch, and C. T. Russell, Astrophys. J. Lett. **864**, L29 (2018).

[15] F. Sahraoui, M. L. Goldstein, P. Robert, and Y. V. Khotyaintsev, Phys. Rev. Lett. **102**, 231102 (2009).
[16] O. Stawicki, S. P. Gary, and H. Li, J. Geophys. Res. **106**, 8273 (2001).
[17] Y. Narita, Astrophys. J. **831**, 83 (2016).
[18] A. A. Schekochihin, S. C. Cowley, W. Dorland, G. W. Hammett, G. G. Howes, E. Quataert, and T. Tatsuno, Astrophys. J. Suppl. Ser. **182**, 310 (2009).
[19] W. M. Macek, D. Wójcik, and J. L. Burch, Astrophys. J. **943**, 152 (2023).
[20] W. M. Macek and D. Wójcik, Mon. Not. R. Astronom. Soc. **526**, 5779 (2023).
[21] J. L. Burch, T. E. Moore, R. B. Torbert, and B. L. Giles, Space Sci. Rev. **199**, 5 (2016).
[22] http://cdaweb.gsfc.nasa.gov.
[23] G. I. Taylor, Proc. R. Soc., London Ser. A **164**, 476 (1938).
[24] H. Risken, *The Fokker-Planck Equation: Methods of Solution and Applications*, Springer Series in Synergetics (Springer, Berlin, 1996).
[25] M. Tabar, *Analysis and Data-Based Reconstruction of Complex Nonlinear Dynamical Systems: Using the Methods of Stochastic Processes* (Springer, Cham, 2019), p. 280.
[26] F. B. Hanson, *Applied Stochastic Processes and Control for Jump-Diffusions: Modeling, Analysis and Computation* (Society of Industrial Applied Mathematics, Philadelphia, PA, 2007).
[27] M. Anvari, M. Tabar, Peinke, and K. J. Lehnertz, Sci. Rep. **6**, 35435 (2016).
[28] E. Daly and A. Porporato, Phys. Rev. E **73**, 026108 (2006).
[29] D. A. Dickey and W. A. Fuller, J. Am. Stat. Assoc. **74**, 427 (1979).
[30] D. Kwiatkowski, P. C. Phillips, P. Schmidt, and Y. Shin, J. Econometr. **54**, 159 (1992).
[31] S. Lück, C. Renner, J. Peinke, and R. Friedrich, Phys. Lett. A **359**, 335 (2006).
[32] S. Benella, M. Stumpo, T. Alberti, O. Pezzi, E. Papini, E. Yordanova, F. Valentini, and G. Consolini, Phys. Rev. Res. **5**, L042014 (2023).
[33] W. M. Macek, Physica D **122**, 254 (1998).
[34] W. M. Macek and S. Redaelli, Phys. Rev. E **62**, 6496 (2000).
[35] C. Tsallis, J. Stat. Phys. **52**, 479 (1988).
[36] L. F. Burlaga and A. F. Viñas, Physica A **356**, 375 (2005).
[37] H. E. Hurst, R. P. Black, and Y. M. Simaika, *Long-term Storage: An Experimental Study*, Vol. 129 (Constable, London, 1965), pp. 591–593.
[38] K. H. Kiyani, S. C. Chapman, Y. V. Khotyaintsev, M. W. Dunlop, and F. Sahraoui, Phys. Rev. Lett. **103**, 075006 (2009).
[39] K. H. Kiyani, S. C. Chapman, F. Sahraoui, B. Hnat, O. Fauvarque, and Y. V. Khotyaintsev, Astrophys. J. **763**, 10 (2013).
[40] O. Alexandrova, V. Carbone, P. Veltri, and L. Sorriso-Valvo, Astrophys. J. **674**, 1153 (2008).
[41] P. Wu, S. Perri, K. Osman, M. Wan, W. H. Matthaeus, M. A. Shay, M. L. Goldstein, H. Karimabadi, and S. Chapman, Astrophys. J. Lett. **763**, L30 (2013).
[42] S. Benella, M. Stumpo, G. Consolini, T. Alberti, V. Carbone, and M. Laurenza, Astrophys. J. Lett. **928**, L21 (2022).